University of Alaska Fairbanks

Final Report

Federal Agency and Organization Element to Which Report is Submitted	U.S. Department of Energy Office of Fossil Energy
FOA Name	Advanced Technology Solutions for Unconventional Oil & Gas Development
FOA Number	DE-FOA-0001722
Nature of the Report	Final Research Performance Progress Report (RPPR)
Award Number	DE-FE0031606
Award Type	Cooperative Agreement
Name, Title, Email Address, and Phone Number for the Prime Recipient	**Technical Contact (Principal Investigator):** Abhijit Dandekar, Professor, adandekar@alaska.edu 907-474-6427 **Business Contact:** Kim Cox, Director UAF Office of Grants and Contracts Administration kwcox@alaska.edu, 907-474-7301
Name of Submitting Official, Title, Email Address, and Phone Number	Same as PI
Prime Recipient Name and Address	University of Alaska Fairbanks Grants and Contracts Administration PO Box 757880, Fairbanks AK 99775
Prime Recipient Type	Not for profit organization
Project Title	**FIRST EVER FIELD PILOT ON ALASKA'S NORTH SLOPE TO VALIDATE THE USE OF POLYMER FLOODS FOR HEAVY OIL EOR a.k.a ALASKA NORTH SLOPE FIELD LABORATORY (ANSFL)**

University of Alaska Fairbanks

Principal Investigator(s)	**PI:** Abhijit Dandekar, *University of Alaska Fairbanks* **Co-PIs:** Yin Zhang, *University of Alaska Fairbanks* Samson Ning, Hilcorp Alaska LLC Randy Seright, *New Mexico Institute of Mining & Technology* Baojun Bai, *Missouri University of Science and Technology* Dongmei Wang, *University of North Dakota*
Prime Recipient's DUNS number	615245164
Date of the Report	January 25, 2023
Period Covered by the Report	June 1 2018-October 31 2022
Reporting Frequency	Final
Signature of Principal Investigator:	 Abhijit Dandekar

Disclaimer

This project was funded by the US Department of Energy, National Energy Technology Laboratory an agency of the United States Government, through a support contract with University of Alaska Fairbanks. Neither the United States Government nor any agency thereof, nor any of their employees, nor University of Alaska Fairbanks, nor any of their employees, makes any warranty, express or implied, or assumes any legal liability or responsibility for the accuracy, completeness, or usefulness of any information, apparatus, product, or process disclosed, or represents that its use would not infringe privately owned rights. Reference herein to any specific commercial product, process, or service by trade name, trademark, manufacturer, or otherwise does not necessarily constitute or imply its endorsement, recommendation, or favoring by the United States Government or any agency thereof. The views and opinions of authors expressed herein do not necessarily state or reflect those of the United States Government or any agency thereof.

TABLE OF CONTENTS

LIST OF FIGURES

LIST OF TABLES

NOMENCLATURE

ABS	Absorbance
ANS	Alaska North Slope
ATBS	Acrylamide Tertiary Butyl Sulfonate
bpd	Barrel Per Day
BHP	Bottomhole Pressure
BP	Budget Period
BS	Backscattering
BS&W	Basic Sediment and Water
BT	Breakthrough
CAPEX	Capital Expenses
CMG	Computer Modeling Group
cp or cP	Centipoise
CPF	Central Processing Facility
CPV	Channel Pore Volume
DMP	Data Management Plan
DPR	Disproportionate Permeability Reduction
DSD	Drop Size Distribution

DSL	Dynamic Scale Loop
EB	Emulsion Breaker
EOR	Enhanced Oil Recovery
EOS	Equations of State
ESEM	Environmental Scanning Electron Microscopy
ESP	Electrical Submersible Pump
FPV	Fracture Pore Volume
FR	Filter Ratio
Fr	Resistance Factor
Frr	Residual Resistance Factor
f_w	Fractional Flow of Water
G’	Elastic Modulus
G”	Viscous Modulus
HPAM	Hydrolyzed Polyacrylamide
HM	History Matching
HSPF	High Salinity Polymerflood
HSWF	High Salinity Waterflood
IAPV	Inaccessible Pore Volume
ICD	Inflow Control Device
ID	Inside Diameter
IFT	Interfacial Tension
IMEX	Implicit Pressure Explicit Saturation Simulator
IOR	Incremental Oil Recovery
IPROF	Injection Profile Log
KI	Potassium Iodide
k or K	Permeability (generally absolute)
k_d	Thermal Conductivity of (Polymer) Deposit
k_t	Thermal Conductivity of Tube Material
Kc	Channel Permeability
Kh	Horizontal Permeability (intrinsic)
Km	Matrix Permeability
Kro	Relative Permeability to Oil
Krw	Relative Permeability to Water
Kv	Vertical Permeability (intrinsic)
LSWF	Low Salinity Waterflood
LSPF	Low salinity Polymerflood
md or mD	MilliDarcy
mg	Milligram
MSR	Matching Size Ratio
nm	Nanometer
No	Corey Exponent for Oil
NPV	Net Present Value
Nvf	Viscous Fingering Number
Nw	Corey Exponent for Water
OD	Outside Diameter

OHTC	Overall Heat Transfer Coefficient
OIW	Oil in Water
OOIP	Original Oil in Place
OPEX	Operating Expenses
OSTI	Office of Scientific and Technical Information
PAS	Polymer Alternating Solvent
PF	Polymerflood
PFO	Pressure Falloff
PFPU	Point Forward Polymer Utilization
PIU	Polymer Injection Unit
PMP	Project Management Plan
PPB	Parts Per Billion
PPG	Preformed Particle Gel
ppm or PPM	Parts Per Million
PRV	Pressure Release Valve
PSU	Polymer Skid Unit
PV	Pore Volume
QC	Quality Control
RF	Recovery Factor or Resistance Factor
R_f	Fouling Factor
RPM	Rotation Per Minute
RRF	Residual Resistance Factor
SC	Standard Conditions
SCTR	Abbreviation of Sector as used in CMG
SE	Spontaneous Emulsion
SEM	Scanning Electron Microscopy
SFB	Simulated Formation Brine
SIB	Simulated Injection Brine
SHR	Keyword in CMG for shear rate dependent polymer viscosity
SHV	Keyword in CMG for Darcy velocity dependent polymer viscosity
SOPO	Statement of Project Objectives
S_{or}	Residual Oil Saturation
S_{orw}	Residual Oil Saturation due to Water
S_{orp}	Residual Oil Saturation due to Polymer
STB	Stock Tank Barrel
STOOIP	Stock Tank Original Oil in Place
S_{wc} or S_{wi}	Connate/Irreducible Water Saturation
TDS	Total Dissolved Solids
T_o	Oil Content in the Water Sample
TPV	Total Pore Volume
TSI	Turbiscan Stability Index
μ	Viscosity
μg	Microgram
U_c	Overall Heat Transfer Coefficient of Clean Tube
U_f	Overall Heat Transfer Coefficient of Fouled Tube

URTeC	Unconventional Resources Technology
USBM	United State Bureau of Mines
UV	Ultraviolet
VE	Viscoelasticity
VRR	Voidage Replacement Ratio
WC	Water Cut
WF	Waterflood
WOR	Water Oil Ratio
WT	Wall Thickness
XRD	X-ray Diffraction
XRF	X-ray Fluorescence

1. Executive Summary

Alaska's high viscosity oil resources that range between 20–30+ billion barrels represent about a third of known North Slope original oil in place (OOIP). These resources are primarily concentrated in the Schrader Bluff formation (also called West Sak on the Western North Slope) and Ugnu reservoirs and are categorized as "viscous oils" and "heavy oils" owing to their in-situ viscosities between 5–10,000 cP and up to a million+ cP respectively. The viscous oil deposits are relatively deeper (2,000 – 5,000 ft), whereas the heavy oils are somewhat shallower (2,000 – 4,000 ft). The typically shallow depths and the proximity to the continuous permafrost results in relatively lower formation temperatures and pressures, and consequently higher viscosities. The vertical depth vs. viscosity delineated in Paskvan et al. (2016) differentiates the viscous and heavy oils. As depicted in Paskvan et al. (2016), currently the main focus (referred to as "developing") is on the viscous oils in the Schrader Bluff formation in the Milne Point Unit (MPU). Notwithstanding this Alaska North Slope (ANS) specific categorization, we use the industry adopted, all-inclusive term "heavy oil" for all high viscosity oils. Resource characterization and additional details can be found in topical publications of Paskvan et al. (2016) and Targac et al. (2005).

Despite the vast resource base, the development pace, vis-à-vis the production of heavy oils has been very slow and limited due to multiple factors such as cost, logistics, challenging arctic environment, poor waterflood sweep efficiency due to mobility contrasts, and significantly high minimum miscibility pressures (MMP). Most importantly, typical or standard thermal methods that are commonplace elsewhere (Canada, California) are inapplicable due to the continuous permafrost. As a consequence, cumulative production of heavy and viscous oils is a little over 1% of OOIP slope wide and currently, there is hardly any production from Ugnu. However, on a broader level, these unfavorable factors are outweighed by the fact that (1) these resources, within the established infrastructure, are too large to ignore because of their strategic importance to the Nation and the State of Alaska and (2) Prudhoe Bay type diluent crude oil is still available for heavy oil transport through the Trans Alaska Pipeline System (TAPS). Similarly, from a reservoir standpoint, the following factors also are important offsets: (1) favorable rock characteristics of Schrader Bluff; (2) the promise demonstrated by the initial scoping studies (Seright 2010, 2011) suggesting significant increase of heavy oil recovery using polymer flooding; (3) successful field implementation in Canada, China and elsewhere in the world, and (4) availability of the existing pairs of horizontal injector-producer in Schrader Bluff.

The foregoing was recognized as the best readily available opportunity for significant investment by the US Department of Energy and the field operator Hilcorp Alaska LLC to conduct the first ever field scale experiment to test the polymer flooding technology to unlock the vast heavy oil resources on ANS. With this primary goal in mind, the research team embarked on a ~4.5 years long project that focused on the field polymer pilot complemented by supporting laboratory and simulation studies. As documented in this final report, over the course of the project, many lessons have been learned and valuable field and supporting laboratory data has been collected, which also is complemented by numerical reservoir simulations. We have been able to establish the injectivity of polymer solution, evidence of significant reduction in the water cut of previously waterflooded pattern, effective propagation of a hydrolyzed polyacrylamide (HPAM), benefits of low salinity water, provide practical guidance on handling of produced fluids containing breakthrough polymer, fit-for-purpose forecast-worthy history matched

simulation model, polymer EOR benefit of 700-1000 bopd over waterflood, and most importantly a low polymer utilization factor of ~1.7 lb/stb. In summary this project is deemed as a scientific, technical and economic success, having met all objectives, fulfilled deliverables and within budget, providing impetus to apply polymer EOR throughout the Milne Point Field paving the way for even heavier viscosity oils in the Ugnu area, eventually extending the economic life of TAPS.

2. Project Goal

The primary goal of this project is to perform a research field experiment to validate the use of polymer floods for heavy oil Enhanced Oil Recovery (EOR) on the Alaska North Slope (ANS). In particular: (1) Systematically evaluate an advanced polymer technology that will integrate polymer flooding, low salinity water flooding, horizontal wells, and injection conformance control treatments into one process to significantly enhance oil recovery for heavy oil reservoirs; (2) Gain field polymer flood performance data to optimize polymer flood design in the Schrader Bluff heavy oil reservoir on ANS' Milne Point Field, Hilcorp J-Pad; (3) Minimize disruption to current/existing field operations, and minimize risk of lost production or damage to the wells, reservoir, facilities and the environment; and (4) Resolve important outstanding technical issues regarding polymer flooding of heavy oils – including the desired polymer viscosity/concentration, salinity, retention, early polymer breakthrough, and treatment of produced fluids that contain polymer. Following are the main scientific/technical objectives:

1. Determine the synergy effect of the integrated EOR technology of polymer, low salinity water, horizontal wells, and conformance treatments (e.g., gels), and its potential to economically enhance heavy oil recovery.
2. Assess polymer injectivity into the Schrader Bluff formations for various polymers at various concentrations.
3. Assess and improve injection conformance along horizontal wellbore and reservoir sweep between horizontal injectors and producers.
4. Evaluate the water salinity effect on the performance of polymer flooding and gel treatments.
5. Optimize pump schedule of low-salinity water and polymer.
6. Establish timing of polymer breakthrough in Schrader Bluff N-sands.
7. Screen an optimized method to control the conformance of polymer flooding at the various stages of the polymer flooding project.
8. Estimate polymer retention from field data and compare with laboratory and simulation results.
9. Assess incremental oil recovery vs. polymer injected.
10. Assess effect of polymer production on surface facilities and remediation methods.

3. Deliverables

The fulfilment of deliverables is summarized in the below table and the technical deliverables are described in specific details in the subsequent **Section 5**.

Table 3.1: Summary of deliverables.

Deliverable	Fulfilment	Verification Method	Comments
Updated Project Management Plan (PMP)	On file with DOE NETL Federal Project Manager, submitted on April 30th 2019	As reported in RPPRs	None
Updated Data Management Plan (DMP)	• Compilation of field data since project start up sent each month to DOE NETL Federal Project Manager. • Articles and other research products such as thesis have been submitted to NETL-EDX.	Injection and production data graphically reported in RPPRs Receipts from E-link submissions	None See **Section 6** and Products in RPPRs
Tabulations of polymer and formation parameters and their resultant performance values	Tabular and graphical results of almost all aspects of polymer retention and propagation.	RPPRs and publications	None
Impact of water salinity on polymer performance, screened polymer gels based on performance criteria of conformance control	Effect of (low) salinity experimentally established. Various gel products and crosslinkers tested.	RPPRs and publications	None
History matched reservoir simulation model for polymer flood, optimized polymer injection strategy, and data files	Following extensive iterations, a robust fit-for-purpose forecast-worthy history matched model has been established. This model has been used to run several sensitivity cases as well as in the economic analysis.	RPPRs and publications	None
Polymer flood performance data	Injection-production data graphically reported and in addition the quantities of polymer	RPPRs and publications	None

	injected, resulting EOR benefit and polymer utilization factor also are documented.		
Screened method/technique for treating/handling produced polymer water	Composite emulsion breaker screened/identified after extensive lab testing. Similarly, fouling tests have established threshold heater-treater operating temperature.	RPPRs and publications	None
Long term suitability of advanced polymer flooding in ANS heavy oil reservoirs	A custom-built economic modeling tool has been used to analyze the performance of polymer flooding incremental to waterflooding. This tool has demonstrated that the first ever polymer flood field pilot for heavy oil EOR is economically beneficial under all the tested scenarios. As an extension of economic analysis, polymer recycling concept testing also has been conducted.	RPPRs and publications	None

4. Broad Accomplishments

Over the 4 years and 4 months period of performance the project has many accomplishments to report; some of the notable ones are listed below.

- Publications have been one of the most important hallmarks of the project with 12 peer reviewed journal articles and 18 conference papers on diverse technical aspects of the polymer pilot.

- A paper presented at the 2021 URTeC was selected as "the best of URTeC" for re-presentation at the 2022 virtual IOR meeting.

- Despite the adverse conditions manifested by Covid-19 (lab access limitation), the project progress remained on track, by careful planning and management of various tasks.

- UAF-PETE graduate student, Cody Keith (reservoir simulation), competed in the 2022 SPE Western Region student paper contest in the MS division and won the first place and also at the international level in October 2022 at the SPE ATCE, https://www.spe.org/en/students/contest/winners/.

- The DOE NETL Federal Project Manager nominated the Alaska North Slope polymer flood project for Special Meritorious Awards for Engineering Innovation (MEA).

- Finally, we believe that the overall success of the project and its outreach (e.g., PI discussed the project and its potential future implications for Ugnu, with the State of Alaska Governor's office staff in May 2021), may have been conducive to attracting $5 million in State of Alaska funding

for heavy oil recovery in Ugnu using a concept known as polymer alternating solvent.

5. Research Findings

Key research findings from the project technical tasks are summarized below. Extensive details are covered in the RPPRs and pertinent topical publications.

5.1 Optimization of Injected Polymer Viscosity/Concentration and Quantification of Polymer Retention

Summary. This section explores the unusual shape of HPAM breakout/propagation during dynamic polymer retention measurements in Milne Point core material. In contrast to conventional expectations, polymer retention does not delay the initial polymer arrival at the end of a Milne Point core. However, after effluent polymer concentrations rapidly rise to at least 50% of the injected value, the concentration gradually "tails" up over many pore volumes before it finally achieves the injected value. To understand the origin and significance of this behavior, a wide range of core experiments were performed, including substantial variations in polymer concentration and molecular weight, core length, preservation state, sand grain size and mineral composition. Illite was identified as primarily responsible for the tailing phenomenon. This phenomenon has important consequences that must be considered when projecting performance of the field project. This work suggests that mineralogy analysis (especially for illite and kaolinite) may reveal whether tailing should be accounted for during simulations of polymer propagation/retention in a given field application. Retention is also strongly influenced by the divalent ion content of the water and the ATBS content of the polymer.

Introduction. In any polymer flood or chemical flood where polymer is used for mobility control, the polymer must propagate deep into the porous rock of the reservoir in order to be effective. Polymer retention (e.g., adsorption, mechanical entrapment) can retard the movement of polymer solutions through the reservoir and thus have an important impact on the efficiency of oil displacement and the economics of a project (Manichand and Seright 2014, Wang et al. 2020). Projections of the impact of polymer retention on a given field project are commonly incorporated into numerical simulations and/or fractional flow calculations (Green and Willhite 2018). Chemical flooding simulators traditionally assume that polymer retention follows the Langmuir isotherm, while fractional-flow calculations usually assume concentration-independent retention. Both models predict a delay in propagation of the polymer front (in proportion to the given retention value), followed by a rapid rise in produced polymer concentration to the injected level. For illustration, the blue curve in **Figure 5.1.1** shows polymer propagation predictions using the Langmuir isotherm (in a simulator), while the black-dashed curve shows predictions from an assumption of concentration-independent retention using fractional flow calculations (all assuming 240 μg/g total polymer retention). In contrast, our laboratory retention studies (Wang et al. 2020) for the Milne Point polymer flood consistently showed virtually no delay in polymer propagation, a rapid rise in produced polymer to 70-90% of the injected concentration, followed by produced concentration gradually approaching the injected value over many pore volumes. This tailing behavior yields overall retention up to 600 μg/g, even though most polymer is not delayed. From a practical viewpoint, this behavior means that retention causes no

significant delay in propagation of the polymer bank (and therefore the oil bank), but the effective viscosity and displacement efficiency are less than originally planned. This work explores why this polymer "tailing" phenomenon occurs.

Detailed aspects of polymer retention were covered during previous reviews (Manichand and Seright 2014; Zhang and Seright 2014; Seright 2017; Wever et al. 2018; Green and Willhite 2018; Guetni et al. 2019; Ferreira and Moreno 2020; Wang et al. 2020; Sugar et al. 2021). However, only Wang et al. 2020 mentioned the tailing phenomenon. Perhaps this phenomenon was not reported previously for fear that the effect might have been an experimental artifact associated with the polymer retention method used. However, in Wang et al. (2020) (and again in this work), three different polymer retention methods were used simultaneously to demonstrate that the tailing phenomenon was a real effect. In addition to the tailing phenomenon, Wang et al. (2020) noted that inaccessible pore volume was negligible in Milne Point cores. They also found no evidence of chromatographic separation of HPAM molecular weights during dynamic retention experiments—the intrinsic viscosity of the first polymer produced from a core was (within experimental error) the same as that produced many pore volumes (PV) later.

Throughout this work, multiple types of laboratory measurements were used to assess HPAM polymer retention. Core floods were used to dynamically determine polymer retention in different Milne Point Schrader Bluff sands, with extensive permeability, grain size distribution, XRD, and XRF characterizations. During all experiments, the effluent was analyzed for brine-tracer concentration, viscosity, total organic carbon, and total nitrogen. The latter three items allowed three independent measures of polymer concentration and polymer retention. In Seright and Wang (2022), experiments were performed with Milne Point core material, oil, brine, and field conditions. We investigated the effects of core preservation state (extending those studies described in Wang et al. 2020). Additional studies were performed to quantify how the tailing phenomenon varied with injection rate, polymer concentration and Mw, and sand grain particle size in Milne Point sands. Mechanistic experiments were also performed (Seright and Wang 2022) using packs of glass beads with controlled levels of various minerals, including illite, kaolinite, montmorillonite, chlorite, calcium carbonate, dolomite, siderite, pyrite, and calcium sulfate. Also, extensive experiments were analyzed that focus on bead packs containing illite—the most prevalent clay in Milne Point core material. These experiments examine a wide range of polymer concentrations and Mw values, flow rates, core lengths, and particle sizes. A model was proposed to account for the tailing phenomenon. This report amplifies and extends this project's work that was formalized in Wang et al. (2020) and Seright and Wang (2022).

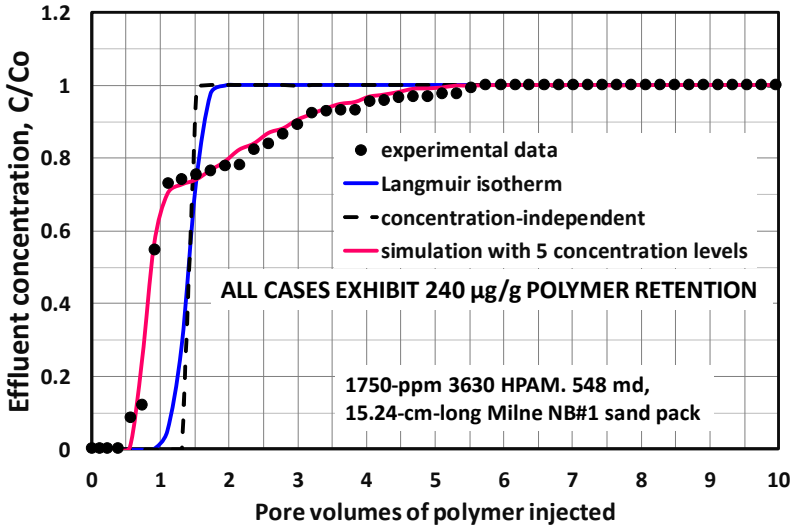

Figure 5.1.1: Tailing phenomenon during a polymer retention study versus model predictions.

Design of experiments

The Brine, Polymers and Polymer Solutions. The synthetic brine in this work was called Milne Point injection water, which contained 2435 ppm total dissolved solids (not including water of hydration)—consisting of 2173 ppm NaCl, 8 ppm KCl, 357 ppm $CaCl_2.2H_2O$, and 73 ppm $MgCl_2.6H_2O$. The calcium and magnesium salts were added as hydrates. This brine was passed through 0.45 µm Millipore filters before further use.

For most of this work, several powder-form partially hydrolyzed polyacrylamides (HPAM) were used: SNF Flopaam 3630S™ (Lot GJ1201, received from the Milne Point field application September 26, 2018), SNF Flopaam 3430S™, SNF Flopaam 3130S™, and Flodrill TS705™. The degree of hydrolysis was 30% for these polymers. In one experiment, Ciba Alcoflood 254S™ was used, which had a 10% degree of hydrolysis. The third column of **Table 5.1.1** lists manufacture-stated molecular-weight (Mw) ranges (based on intrinsic viscosity). We made our own measurements of intrinsic viscosity and Mw in the Milne Point injection water, using the methods of Jouenne and Levache (2020). These Mw values are listed in the fourth column, while the fifth column lists C^* values—the critical polymer overlap concentration. Below this concentration, polymer molecules generally float free and un-entangled in solution. Above this concentration, the polymer molecules are entangled with others.

Polymer solutions were prepared by sprinkling polymer powder (over the course of four minutes) onto the brine vortex created by an overhead stirrer (IKA RW-200) at 300 rpm with a four-blade propeller. After initial mixing for several hours at high rate, the stir rate was reduced to ~100 rpm for at least one day. Polymer solutions were confirmed to be homogeneous by the absence of any lumps within a thin layer as the fluid flowed over a beaker lip when poured from one beaker to another. As in the field application, our target polymer solution viscosity was 45 cp (at 7.3 s^{-1} 25°C). For consistency in many studies, we fixed concentrations at 1750 ppm Flopaam 3630S and 2000 ppm

Flopaam 3430S.

Table 5.1.1: Mw and C* parameters for HPAM polymers.

Polymer	Anionicity, %	Manufacturer-stated Mw million g/mol	Measured Mw, million g/mol	*C**, ppm
Flopaam 3630S	30	17 – 19	18**	200
Flopaam 3430S	30	10 – 12	11	300
Flopaam 3130S	30	3 – 5	2.7	850
Flodrill TS705	30	--	0.3	4500
Alcoflood 254S	10	0.25 - 0.5	0.1	10000

** This case was used as a starting basis for the calculations and comparison.

The Sands. The Schrader Bluff sands of the Milne Point polymer flood were the NB and OA sands. The current polymer pilot is flooding NB sands, but OA sands are of high interest for expansion of the polymer flood. Our experiments used NB sands (provided by Hilcorp) from two different wells (located 3000 ft apart and at slightly different depths). We labeled NB sands from 3908 ft of the Pesado well as "NB#1"; and NB sands from 3757 ft of the Liviano well as "NB#3". The OA sand used in this work was from 4067 ft of the Pesado well. The sands are fairly similar in elemental composition, except the OA sand contains 5-7 times as much calcium, 30% more iron, and 30-100% more magnesium, and 70-90% less sulfur than the NB sands. The NB#3 sand had 4-5 times as much sulfur as the NB#1 sand. The clay contents of the various sands were similar, with the NB#3 sand containing slightly less than the others. The OA sand contained noticeably more dolomite and feldspar (albite and orthoclase) than the NB sands. Grain-size distributions were obtained for the sands and materials used to make synthetic sand packs. These distributions were obtained using a laser-diffraction method (Malvern Mastersizer 3000™ with Hydro EV™ dispersing unit), which provides volume-based measurements (Seright and Wang 2022).

Sand Pack Preparation. Our packing procedures are described in Wang et al. (2020). Typically for the current work, we used biaxial Temco Hassler core holders. These were 2.54-cm diameter, and usually either 15.24-cm or 30.48-cm in length. To fine-tune the desired pack permeability, the confining pressure (i.e., overburden pressure) was varied (between 100 and 1750 psi). However, 500 psi confining pressure was most commonly used, unless stated otherwise. GE Druck DPI 104™ pressure transducers were used—either 1000-psi transducers with 0.1 psi readout or 300-psi transducers with 0.01 psi readout. Four ISCO (Model 500D or 1000D™) pumps were used during a typical experiment—one each for brine, polymer solution, oil, and confining pressure.

The condition of the sand varied. In some cases, the sand was used as received ("native state"), where some unquantified level of residual water and oil was present. Other times, the sand was washed/extracted with toluene and methanol and dried before use. In some cases, the sands were saturated only with brine before use. In other cases, the sand packs were "restored"—i.e., flooded with fresh Milne Point oil (viscosity ~ 111 cp at 25°C) to connate water saturation, followed by flooding with at least 150 PV of brine to drive the sand pack to residual oil saturation. Preserved cores were also used. (Preserved cores were carefully collected by the field operator during drilling/coring

so that the wettability of the cores was maintained at or close to that within the reservoir. Further, the cores were sealed and stored in a controlled environment to maintain their condition until use.)

For comparison, some experiments referenced in Wang et al. (2020) (using the same Milne Point core material) contained no oil. The mechanistic bead-pack studies in the last part of this work (where illite and other materials were added) contained no oil.

Flood Sequence and Polymer and Tracer Detection. After pack saturation, characterization, and stabilization of brine injection at a low rate (typically, 1.86 or 3.7 ft/d darcy velocity), 5-13 PV of polymer solution were injected at a fixed rate, while monitoring pressure drops across the pack or pack sections.

Effluent from packs was analyzed by several methods. Routinely, we monitored a water tracer (20 ppm potassium iodide) using a Genesys 2™ spectrophotometer at a wavelength of 230 nm. Effluent polymer concentration was monitored by three methods: total organic carbon, total nitrogen, and viscosity. For total organic carbon, a Shimadzu TOC-L™ was used. We recognize that this measurement might be influenced by the presence of any oil. Total nitrogen was measured using chemiluminescence with a Shimadzu TNM-L™ unit. Viscosity was measured at 7.3 s^{-1} (25°C) using proRheo LS-300™ and/or Vilastic VE™ rheometers. The previous measurements were made at 3-4 cm^3 increments for each effluent sample.

Figure 5.1.2 illustrates the results during 10 PV of polymer injection (2000 ppm Flopaam 3430S) for a 15.24-cm-long pack with 232-md native-state OA sand with 500-psi confining pressure. In **Figure 5.1.2**, all values are reported relative to the injected values. The dashed blue curve shows the tracer (KI) breakout. The black and green curves show breakout of the polymer, as judged by carbon content and nitrogen content, respectively. The solid red curve plots effluent produced polymer concentrations that were based on viscosities (using a relation between viscosity and concentration that was reported in Wang et al. 2020).

The difference in area between the tracer (dashed blue) curve and a given polymer curve in **Figure 5.1.3** can be used to calculate polymer retention (if one assumes that inaccessible pore volume is zero). Specifically, **Equation 5.1.1** (from Manichand and Seright, 2014) provides a means for the calculations:

$$R_{pret} = \{[\Sigma\,[(C_p/C_{po} * \Delta PV) - (C_t/C_{to} * \Delta PV)]] + IAPV\} * C_{po} * PV / M_{rock} \qquad (5.1.1)$$

where R_{pret} is polymer retention, C_p is effluent polymer concentration, C_{po} is injected polymer concentration, C_t is effluent tracer concentration, C_{to} is injected tracer concentration, PV is the volume in one pore volume, ΔPV is pore-volume increment, and M_{rock} is the rock mass in the sand pack.

In **Figure 5.1.2**, polymer retention values were 236 μg/g based on effluent nitrogen, 156 μg/g based on effluent carbon, and 204 μg/g using viscosity-based concentration. The nitrogen-based calculation provides the most reliable answer because the carbon-based method could be influenced by any carbon

contamination (e.g., residual oil) and polymer degradation could affect the viscosity-based method. To elaborate, if the produced carbon concentrations are higher than the nitrogen concentrations (because of the presence of oil), that makes the area between the tracer and carbon effluent curves smaller than that between the tracer and the nitrogen effluent curves—which in turn, makes polymer retention appear smaller for carbon detection than for nitrogen detection. Consequently, all subsequent retention values reported in this work are based on nitrogen detection.

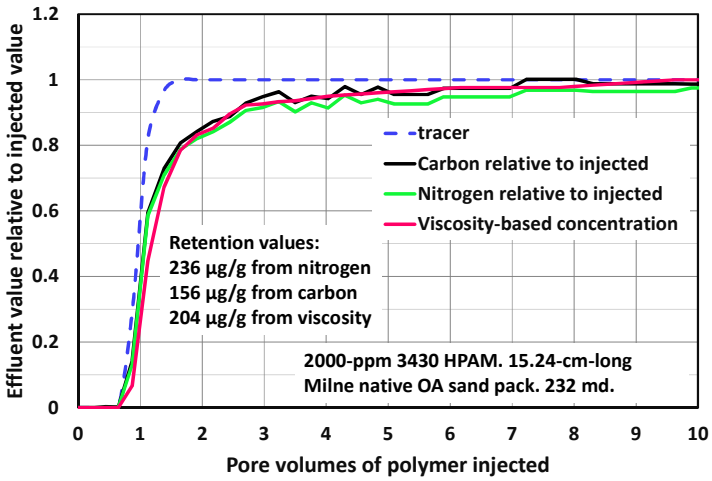

Figure 5.1.2: Effluent composition during polymer injection (232-md native OA sand).

Summary of key results

Inaccessible Pore Volume. Manichand and Seright (2014) reviewed previous petroleum literature for the phenomenon of inaccessible pore volume (*IAPV*). They noted that a limited number of inaccessible pore volume values were reported in the literature, and that the range of values reported is inconsistent, considering the conditions of the experiments. One might expect *IAPV* to increase with decreasing permeability and increasing HPAM molecular weight. However, **Table 5.1.2** (which compares several HPAM *IAPV* values from the literature) indicates no clear relation between *IAPV*, permeability, and *Mw*.

Manichand and Seright (2014) point out that the available theories for the *IAPV* phenomenon cannot explain the magnitude and odd variations of *IAPV* with changes in permeability. It was noted the average diameter of an HPAM molecule in solution (~0.5 µm) is small enough that the polymer should be able to easily fit into over 99% of the pores present in typical polymer floods (Manichand and Seright, 2014).

We found a possible explanation for the inconsistent reports of inaccessible pore volume in the literature. In particular, we suggest that previous studies used varying volumes of brine to flush polymer from the cores between the first and second cycles of polymer injection. (Determination of *IAPV* requires injection of a polymer bank, followed by a brine bank to flush out un-adsorbed polymer, followed by a second polymer bank that presumably will not experience further retention, Lotsch *et al*. 1985.) When brine displaces viscous polymer solution, viscous fingering will occur, and many (100 or more) *PV* of brine may be required to displace all free (un-adsorbed) polymer (Chen *et*

al. 2016, Seright 2017). If insufficient brine is injected during this period, some of the pore space will still be occupied by free polymer that could eventually be displaced. In other words, that un-displaced polymer could be misinterpreted as *IAPV*. To investigate and demonstrate this possibility, consider **Figure 5.1.3**, which plots residual resistance factor versus *PV* during brine injection after polymer for two different sand packs. (In each case, the packs were 30.5-cm long, with an internal pressure tap at 15.24 cm. The reported residual resistance factors apply to the second section of the packs.) Residual resistance factor is defined as mobility during original brine injection (before polymer injection) divided by brine mobility after polymer is displaced. It is often considered the permeability reduction provided by adsorbed polymer. In **Figure 5.1.3**, the blue curve plots residual resistance factors during brine injection for the case of a 4100-mD NB#3 sand pack. Note that the residual resistance factor was 4 after 5 *PV* of brine and 1.6 after 100 *PV*.

Table 5.1.2: Literature *IAPV* values for HPAM.

Porous medium	*k*, mD	HPAM*	*Mw*, 10^6 g/mol	*IAPV*, %	Reference
Berea	49-61	Pusher 500	3	17-37	Dabbous 1977
Berea	761	Pusher 500	3	19	Dabbous 1977
Berea	90-120	Pusher 700	5	0-4	Knight *et al* 1974
Berea	277	Pusher 700	5	18.7-24	Shah *et al.* 1978
Berea	470	Pusher 700	5	22	Dawson & Lantz 1972
Bartlesville	2090	Pusher 700	5	24	Dawson & Lantz 1972
Reservoir sand	30-453	Pusher 700	5	32-37	Vela *et al*. 1976
Teflon	86	Pusher 700	5	19	Dominguez & Willhite 1977
Sand pack	12600	Flopaam 3630S	18	35	Pancharoen *et al*. 2010

* All three HPAMs had 30% degree of hydrolysis.

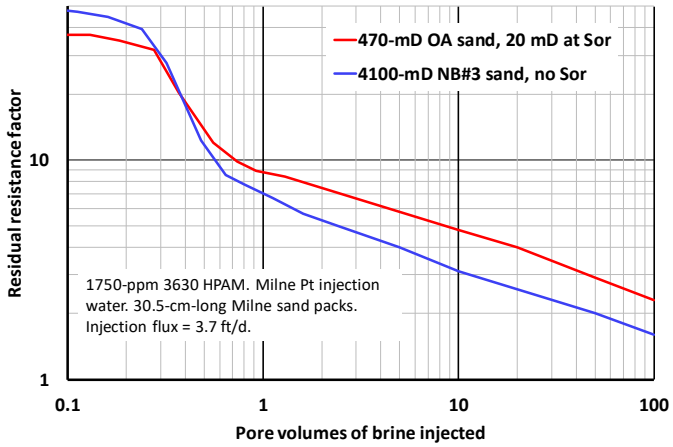

Figure 5.1.3: Residual resistance factors during 100 *PV* of brine injection.

A flood was performed involving a 470-mD OA-sand pack with a confining pressure of 1000 psi. After initial brine saturation, this pack was flooded to high oil saturation and then aged for 6 days at

60°C. The pack was then flooded with 150 *PV* of brine to reach residual oil saturation. Subsequently, the pack was flooded with 9.3 *PV* of 1750 ppm Flopaam 3630S HPAM. In **Figure 5.1.4**, the black curve shows the polymer breakout, while the green curve shows the tracer breakout during the first polymer injection into this sand pack. After polymer injection, 7 *PV* of brine were injected, ending with a residual resistance factor of 5.3. After this brine, a second bank of polymer solution was injected. In the dashed blue curve of **Figure 5.1.4**, the 50% effluent polymer concentration level (as judged by nitrogen chemiluminescence) was reached at 0.7 *PV* polymer injection—suggesting that the *IAPV* was 30%. Following this second polymer bank, 100 *PV* of brine were injected to drive the pack to a residual resistance factor (in the second pack section) of 2.3. At this point, a third bank of polymer solution was injected. For this case, the red curve in **Figure 5.1.4** indicates that the *IAPV* was close to zero (because the 50% polymer concentration was reached at 1 *PV*). Thus, even in a porous medium with 20-mD permeability to water (i.e., 470-mD OA-sand) at S_{or}, the polymer appears to access all the aqueous pore space. This example illustrates how incomplete flushing of mobile polymer solutions (during a brine post-flush) can be misinterpreted as *IAPV*. For the remainder of this work, we assume that inaccessible pore volume is zero. For field applications of polymer flooding, we support the suggestion of Manichand and Seright (2014): "A conservative approach to design of a polymer flood would assume that *IAPV* is zero, especially in multi-darcy sands."

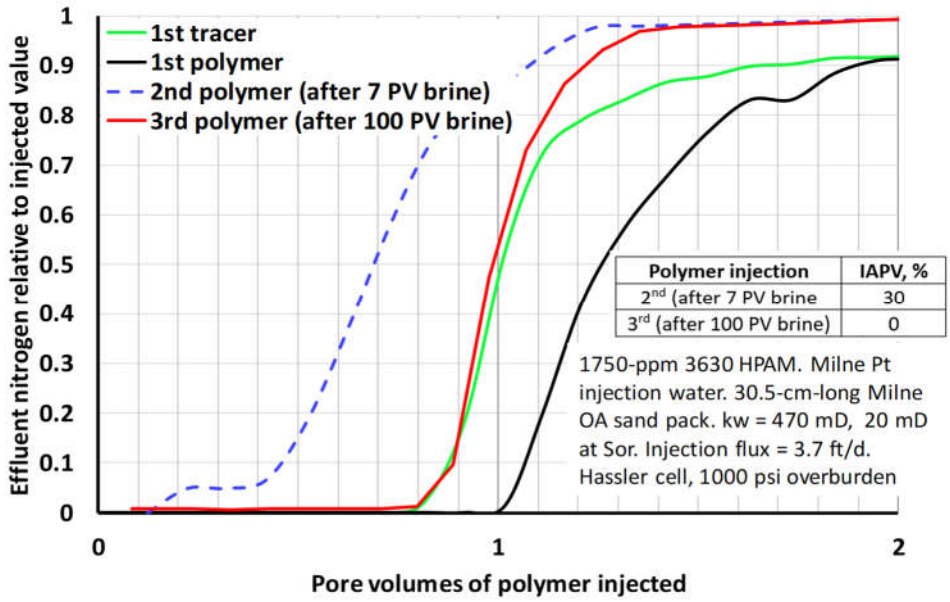

Figure 5.1.4: Nitrogen breakout during three polymer injections into 20-mD OA sand.

Effect of Polymer Molecular Weight, and Concentration. Our work indicated that the tailing was not sensitive to HPAM concentration (between 600 and 1750 ppm) or Mw (between 11 and 18 million g/mol) in Milne Point core material (Seright and Wang 2022). However, we were concerned that greater ranges of concentration and Mw were needed to properly investigate these effects. Consequently, additional retention studies were performed using SNF Flopaam 3130S (Mw~2.7 million g/mol) and SNF Flodrill TS705 (Mw~0.3 million g/mol). All SNF polymer had 30%

anionicity (degree of hydrolysis). We also tested Ciba Alcoflood 254S (Mw~0.1 million g/mol, 10% anionicity). The experiments were performed in bead packs with 9% illite (that was sieved through 100 mesh) using 1750 ppm and 200 ppm HPAM.

Comparison of the solid and dashed red and black curves in **Figure 5.1.5** reveals qualitatively similar behavior for the 2.7- and 18-million-g/mol polymers—except that the 2.7-million-g/mol HPAM exhibited less than half the retention—especially between 1 and 2.5 PV. Retention values for these cases are listed in **Table 5.1.3**.

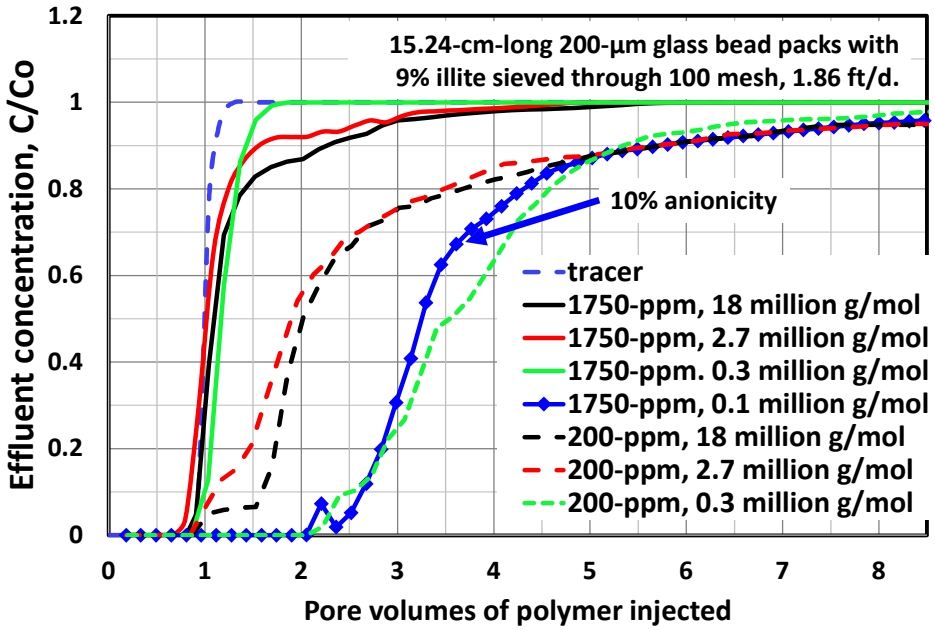

Figure 5.1.5: Tailing phenomenon in 9% illite versus HPAM molecular weight and concentration (30% anionicity).

Table 5.1.3: Effect of various parameters for HPAM retention on illite (with 200 μm beads).

Mw, 10^6 g/mol	Anionicity, %	HPAM, ppm	Illite, %	Illite sieving	Rate, ft/d	Length, cm	Retention, μg/g	Retention, μg/g of illite
18	30	1750	9	<100 mesh	0.31	15.24	152	1672
18	30	1750	9	<100 mesh,	1.86	15.24	123	1353
18	30	1750	9	<100 mesh,	12.4	15.24	99	1089
18	30	200	9	<100 mesh	1.86	15.24	162	1782
2.7	30	1750	9	<100 mesh	1.86	15.24	53	583
2.7	30	200	9	<100 mesh	1.86	15.24	80	880
0.3	30	1750	9	<100 mesh	1.86	15.24	71	781
0.3	30	200	9	<100 mesh	1.86	15.24	102	1122
0.1	10	1750	9	<100 mesh	1.86	15.24	972	10692
18	30	1750	9	no sieving	1.86	15.24	125	1375
18	30	1750	9	20-100 mesh	1.86	15.24	117	1287
18	30	1750	9	20-100 mesh	1.86	30.48	69	759
18	30	1750	9	20-100 mesh	1.86	61.00	100	1100
18	30	1750	4.5	20-100 mesh	1.86	15.24	3	66
18	30	1750	18	20-100 mesh	1.86	15.24	133	732
18	30	1750	36	20-100 mesh	1.86	15.24	209	575

Interestingly, the 0.3-million-g/mol HPAM at 1750 ppm (solid green curve) exhibited no tailing, but a slight delay in initial polymer breakthrough (consistent with the Langmuir isotherm), yielding 71 μg/g retention. In contrast, the blue-diamond curve in **Figure 5.1.5** shows that the 0.1-million-g/mol polymer (10% anionicity) exhibited a substantial delay in polymer propagation. In this case, no polymer was produced until 2-2.5 PV. The solid red and black curves in **Figure 5.1.5** showed that the higher-Mw (2.7 and 18 million g/mol) polymers (at 1750 ppm) exhibited no delay in polymer breakthrough. This difference suggests that either the lowest-Mw HPAM (0.1 million g/mol) can penetrate deeper into the illite—leading to very high adsorption/retention (972 μg/g)—or that 10% anionicity causes substantially greater adsorption/retention than 30% anionicity. In contrast, the higher-Mw HPAMs appear largely unable to penetrate into the illite upon initial contact—resulting in significantly lower retention (53 to 123 μg/g). (Of course, a study to decouple the effects of Mw from the degree of hydrolysis should be interesting. Also, a study of the behavior using different salinity values could be interesting, since the surface charge of clay may depend on these parameters. These points will be addressed shortly.)

Note that all (except the case of 0.3-million-g/mol HPAM at 1750 ppm) polymers exhibit substantial

tailing after polymer breakthrough (when 9% illite was present). This result suggests that even the lowest-Mw polymer (0.1 g/mol) experiences difficulty in penetrating into the tightest illite pores. For 200 ppm of the 2.7- and 18-million g/mol HPAMs (dashed red and black curves), the retention curves were notably below the solid red and black curves (1750 ppm). The polymer concentration was at or below C^* for the dashed red and black curves and for the blue-diamond and green curves (see **Table 5.1.1**)—suggesting that the polymer more easily penetrates into the illite when the polymer concentration is at or below C^*. However, one could argue that the solid green curve (0.3-million g/mol at 1750 ppm) might be an exception to this rule. **Figure 5.1.5** and **Table 5.1.3** suggest a complicated relation between polymer retention on illite and polymer Mw, concentration, and anionicity.

Effect of Illite Content. To test how the tailing phenomenon depends on illite composition in the pack, additional experiments were performed (using the illite that passed through 20 mesh but was retained by 100 mesh). The illite content ranged from 4.5% to 36%, corresponding to pack permeabilities that ranged from 1730 to 6527 md. **Figure 5.1.6** shows the results. Very little retention (3 μg/g) was seen with 4.5% illite. The dashed black curve in **Figure 5.1.6** was quite similar to that for the KI tracer curve (not shown) for the 4.5%-illite case, and tailing was not particularly evident. In contrast, retention increased from 117 μg/g to 209 μg/g as illite content rose from 9% to 36%. The level of tailing became more pronounced also. In **Figure 5.1.6**, the produced polymer concentrations departed from the KI-tracer curves at ~80% (of injected concentration) for 9% illite (green curve), ~70% for 18% illite (red curve), and ~50% for 36% illite (solid black curve). The produced polymer concentrations reached the injected values at ~4 PV for 9% illite, ~5 PV for 18% illite, and ~10 PV for 36% illite. These results suggest that the level of contact of polymer with illite was important. All cores visually appeared to have the illite uniformly distributed throughout the core—as judged by the color, texture and core integrity. Of course, the illite could have experienced segregation on a sub-visual level. However, if the illite was macroscopically segregated, the KI tracer breakout curves should have reflected this—via a noticeable tail in the KI breakout curves. In contrast, all KI tracer breakout curves for these cases were quite sharp—indicating homogeneous cores. Further, as shown in **Figure 5.1.7**, a plot of log of permeability versus porosity (red data points and line) follows a consistent relation with changing illite content. If substantial segregation occurred for the beads and illite, one would have expected a substantial deviation for the plot in **Figure 5.1.7**, as suggested by the dashed blue curve (which was calculated assuming Darcy's law for flow in parallel for totally segregated material).

We also performed an experiment that contained only 20-100-mesh illite (i.e., no glass beads). When subjected to 500 psi confining pressure, permeability to brine was only 0.4 md. Due to the low permeability, polymer injection was not attempted. Instead, we dried the pack and re-determined the particle size distribution to see if the process of compression (to 500 psi) affected particle size. The compression process did indeed alter the illite size distribution—by significantly increasing the fraction of smaller illite particles. The compression process produced small particles so that the low end of the size distribution (below 100 μm) matched that associated with the original un-sieved illite.

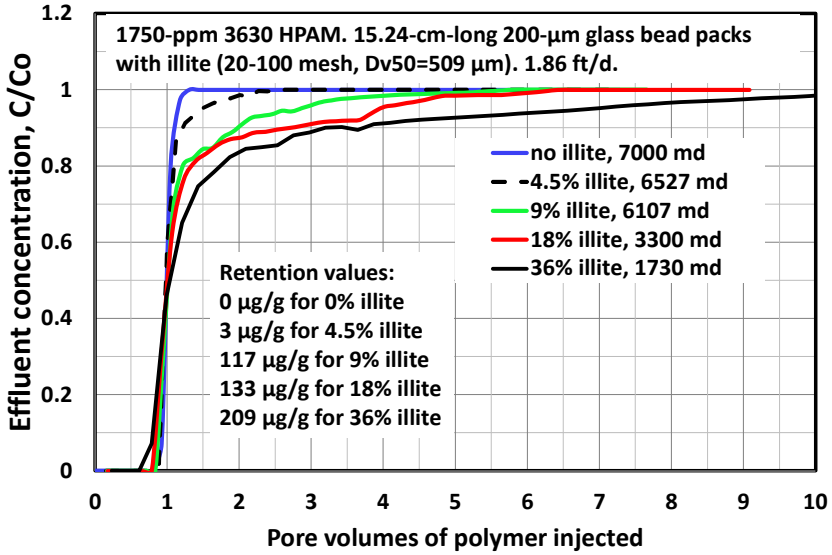

Figure 5.1.6: Tailing phenomenon in 20-100-mesh illite versus illite content in bead pack.

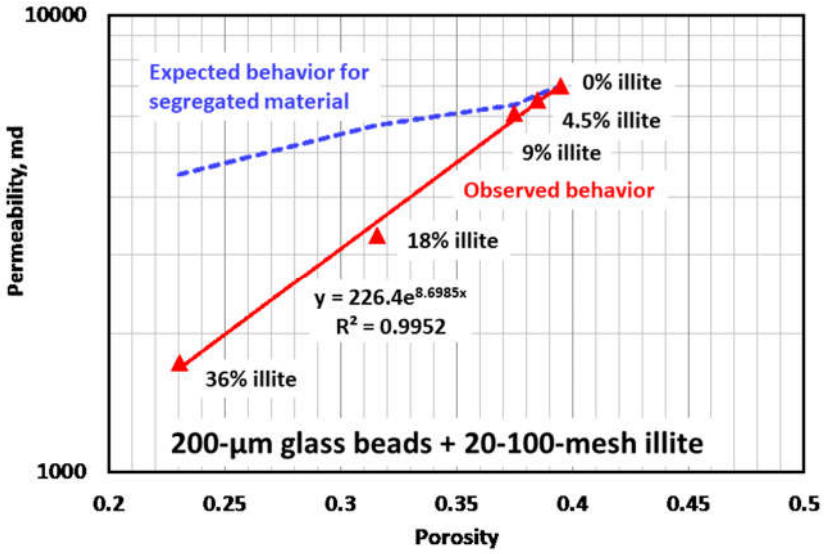

Figure 5.1.7: Permeability-porosity relation versus illite content.

Effect of Pack Length. Using packs that contained 9% illite (20-100 mesh), **Figure 5.1.8** shows that the tailing phenomenon persisted for pack lengths from 15.24 to 61 cm. Although some variation was observed, the nature of the tailing was similar over this range of lengths—with total retention values from 69 to 117 µg/g. If the tailing was caused by channeling of polymer through a pack (because of heterogeneity or uneven illite distribution along the pack), one would have expected the tailing to be mitigated as pack length increased. So, the behavior in **Figure 5.1.8** is consistent with our other observations indicating that the packs were all reasonably homogeneous—and the tailing was not due to uneven contact with illite within the packs.

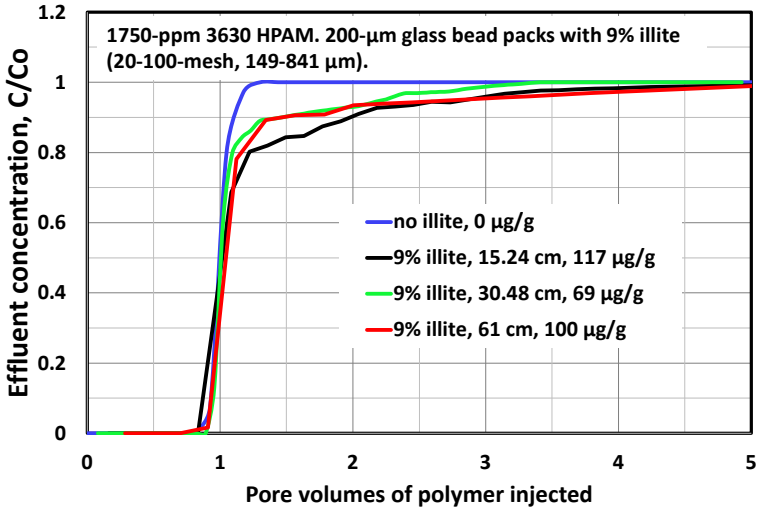

Figure 5.1.8: Tailing phenomenon in 20-100-mesh illite versus pack length.

Surface Area/Particle Size. Electron micrographs of illite (Keller et al. 1986) show the surfaces to be quite rough. Polymer adsorption is expected to depend on the surface area of the adsorbing mineral. For a fixed weight of mineral, small particles will have a larger surface area than large particles. Consequently, one would expect polymer retention should be noticeably higher for packs with small particles than with large particles. In contrast, this concept does not receive much support from our work. Whatever is causing the tailing phenomenon seems to be fairly insensitive to particle size (Wang et al. 2020; Seright and Wang 2022). However, as suggested earlier, compression of the clay (e.g., to 500 psi) may have renormalized the illite size distribution to more closely match the original, un-sieved clay. In that case, perhaps all our illite cases that were compressed actually had similar distributions of small illite particles. Also, the particle-size measurements were made under conditions where the particles were well-dispersed so that all grains had minimum contact with other particles. The extensive grain contact in compacted cores would substantially reduce the surface area that could contact the polymer.

Retention per g of Illite. For much of the above data for bead packs with illite, **Table 5.1.3** summarizes the results and (in the last column) expresses HPAM retention as µg per gram of illite. Previous calculations (summarized in the eighth column) included all solids (i.e., glass beads plus mineral) in the denominator of the retention calculation. If the results are excluded for the 4.5%-illite case and the polymer with 10% anionicity, HPAM retention averaged 1100 µg of polymer per gram of illite—with variations extending from 575 to 1782 µg/g. Thus, it appears that for 9% illite and above, HPAM (with anionicity=30%) retention (after many PV of polymer injection) is roughly 1100 µg/g of illite, regardless of other conditions. However, from the last column of **Table 5.1.3**, we note that the average retention on illite that was sieved through 100 mesh (<149 µm) was generally higher than that for 20-100-mesh (149-841 µm) illite. This observation is consistent with the idea that smaller particles have a greater surface area and therefore should exhibit higher HPAM retention.

Proposed model. In formulating a model for the retention tailing phenomenon, the model must

account for the experimental observations mentioned previously. One can conceive of multiple mechanisms. Some mechanisms that could not adequately explain our experimental observations (e.g., polymer imbibition, flocculation, and inaccessible pore volume). This section will focus on the most applicable mechanism that we have examined to date. However, as will be seen, unanswered questions remain.

Much of the data (for HPAM with Mw=18-million g/mol, 30% anionicity in packs with 9% illite) could be fitted using an "exposure parameter", *Lp*, that is defined in **Equation 5.1.2**:

$$Lp = (t - t_{bt})\ u\ C^{0.5} \tag{5.1.2}$$

where, t is time since the start of polymer injection (seconds), t_{bt} is the time of first polymer arrival at the end of the core (seconds), u is darcy velocity (cm/s), and C is injected polymer concentration (weight fraction). The units for Lp are cm-(wt. fraction)$^{0.5}$. The effluent polymer concentration, relative to the injected value, C/Co, was predicted quite well using **Equation 5.1.3**.

$$C/Co = 1 - 0.7\ e^{-Lp/0.03} - 0.3\ e^{-Lp/0.25} \tag{5.1.3}$$

The solid red curve in **Figure 5.1.9** reveals that this model described the observed behavior quite well for HPAM concentrations from 200 to 1750 ppm, darcy velocities from 0.31 to 12.4 ft/d, pack lengths from 15.24 to 61 cm, and independent of illite particle size.

To rationalize this model, we note that polymer retention depends on the total time ($t - t_{bt}$) of polymer exposure to illite. This time difference is multiplied by the injection rate, u, to reflect that low rates cause longer exposure times for a given fluid element. This product is then multiplied by the square root of polymer concentration. One would expect that lower HPAM concentrations would show reduced reaction rates. However, the cause of the dependence on the square root of concentration is less obvious.

In **Equation 5.1.3**, the two exponential terms suggest that two exposure-dependent processes occurred at the same time. The middle term reveals that ~70% of the concentration change was due to a relatively short process (with an exposure constant of 0.03), while the third term indicates that ~30% of the concentration change was ascribed to the longer process (with an exposure constant of 0.25). We understand the temptation to note the 0.3 multiplier and its similarity to the 20-30% inaccessible pore volume (*IAPV*) values that were sometimes reported in the literature (Manichand and Seright 2014). However, Seright and Wang (2022) presents argument why the tailing phenomenon should be differentiated from *IAPV*. (In particular, *IAPV* accelerates polymer propagation through porous media, whereas the tailing phenomenon does not.) Also, we understand that **Equation 5.1.3** may require adjustment of the parameters for other polymer Mw values or illite concentrations. Consequently, additional work is needed.

Conceivably, the short process could be HPAM adsorption onto the outer (most accessible) surface of the illite, while the longer process could be associated with HPAM penetrating more deeply into the

rough illite. To elaborate, illite is known to be a layered structure where an alumina layer is tightly bound between two silica layers, which in turn are loosely bound to other layers. One might speculate that HPAM intercalates between the loosely bound layers to explain the tailing process. A problem with this logic is that intercalation of HPAM between illite layers should expand the clay, leading to clay swelling and subsequent permeability reduction of the porous medium. This plugging/permeability reduction was never observed with any of our experiments with illite.

Another possibility is that HPAM adsorption occurs only on the outer surface of the illite, but that two separate types of adsorption sites exist with different adsorption characteristics—causing the double exponential in **Equation 5.1.3**. Additional work is needed to understand the tailing phenomenon.

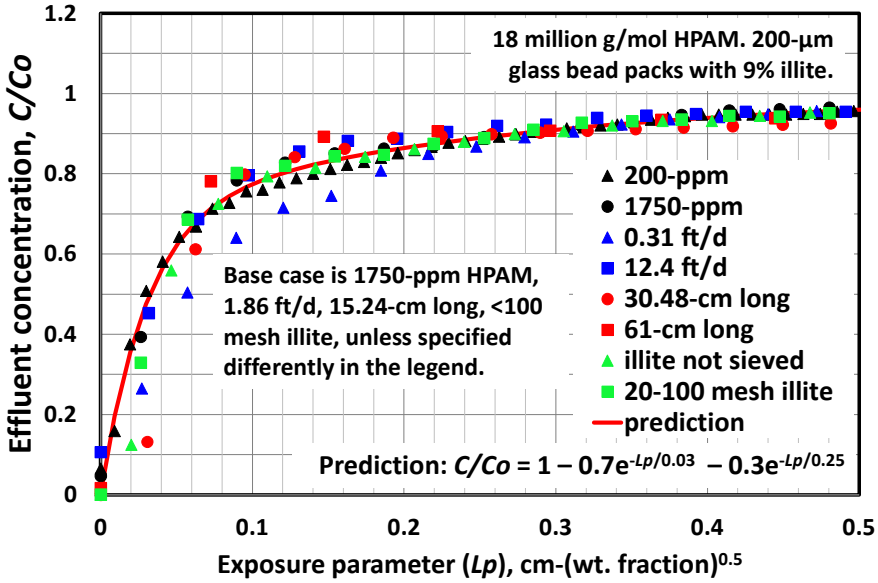

Figure 5.1.9: Match of experimental data with the double-exponential model.

Effect of salinity and hardness on polymer retention. We examined the effect of salinity and hardness (divalent cation content) on polymer retention. These experiments used 1750 ppm Flopaam 3630S in packs with 9% illite. (Polymer retention results are shown in **Figure 5.1.10**, while **Figure 5.1.11** shows viscosity versus shear rate for the solutions examined.) The solid black curve in **Figure 5.1.10** illustrates the typical retention tailing phenomenon that we have observed previously in bead packs with 9% illite when the brine was our "Milne Point Injection brine" (composition indicated in the figure legend). The total polymer retention was 125 µg/g when the brine contained 0.22% NaCl, 0.027% $CaCl_2$ and 0.0034% $MgCl_2$. The dashed black curve shows that similar tailing and retention were noted (114 µg/g) for a similar salinity but with no magnesium (0.18% NaCl, 0.06% $CaCl_2$). When synthetic Milne Point formation brine was used (solid green curve: 2.56% NaCl, 0.065% $CaCl_2$, 0.11% $MgCl_2$), polymer retention was modestly greater (145 µg/g)—even though salinity was about ten times greater and hardness was about six times greater than for the Milne Point injection brine case (solid black curve). The solid green curve exhibited about the same retention tail as the solid black curve, but a significant delay in polymer arrival was noted for the green curve, whereas the delay was not seen for the solid black curve.

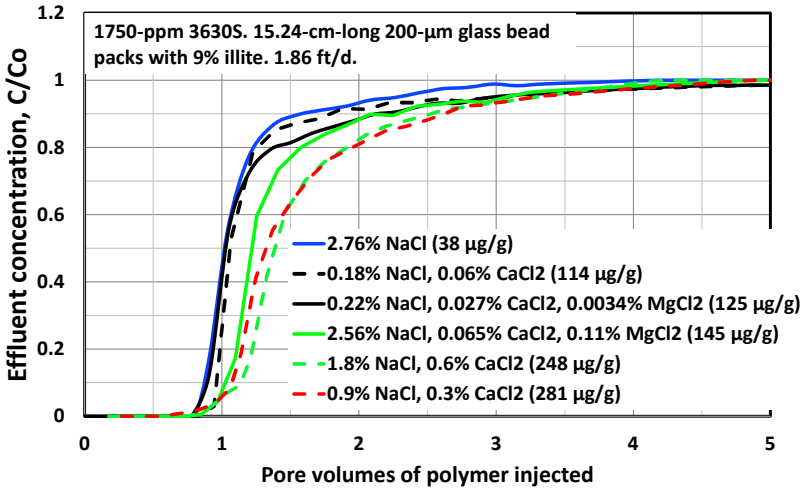

Figure 5.1.10: Divalent cations accentuate HPAM retention.

When using 2.76% NaCl with no divalent cations (the solid blue curve in **Figure 5.1.10**), polymer retention was much lower (38 µg/g). Thus, it appears that much of the polymer retention on illite is tied to the presence of divalent cations. To further test this idea, experiments were performed using a brine with 1.8% NaCl and 0.6% $CaCl_2$ (dashed green curve in **Figure 5.1.10**). This case had roughly the same total salinity as the Milne Point formation brine (solid green curve) and the 2.76%-NaCl brine (solid blue curve), but the calcium content was much higher and a substantially greater polymer retention was seen (248 µg/g). We tried to prepare polymer solutions with even higher calcium concentrations, but the HPAM would not dissolve fully in those brines. Another case was tested with 0.9% NaCl and 0.3% $CaCl_2$—leading to a polymer retention of 281 µg/g (dashed red curve in **Figure 5.1.10**). For these last two cases, note that retention is higher primarily because of delay in arrival of the HPAM. The retention "tail" is not greatly different from most of the other cases in **Figure 5.1.10**. The overall conclusion here is that HPAM retention on illite is dominantly dictated by divalent ion content—much more so than salinity, injection rate, polymer concentration, polymer Mw, degree of hydrolysis, polymer solution viscosity, presence/absence of residual oil, or wettability state (Wang et al. 2020, Seright and Wang 2022).

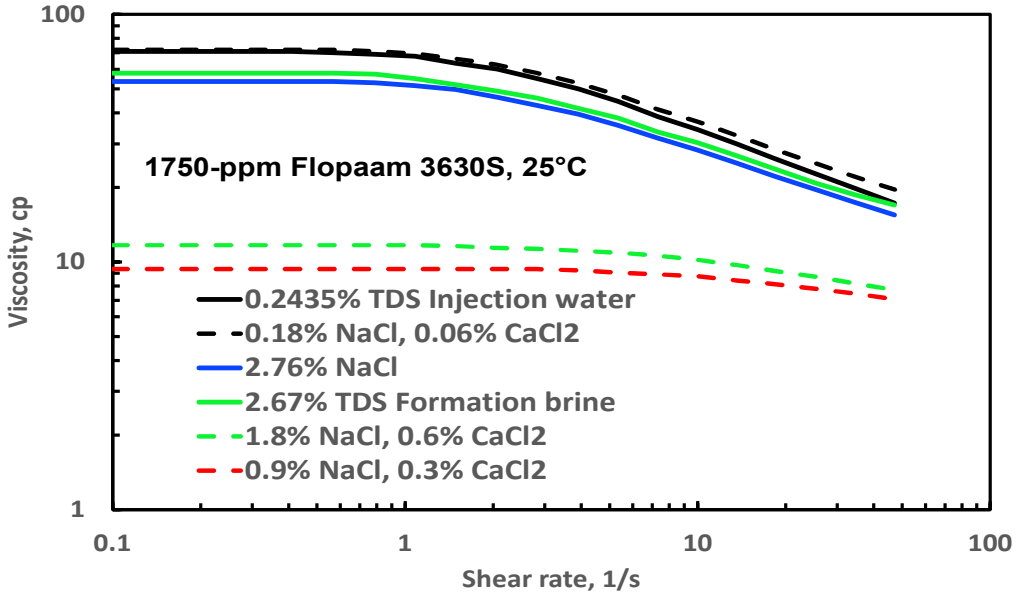

Figure 5.1.11: Viscosity versus shear rate for HPAM in various brines.

Effect of polymer ATBS content on polymer retention. We also examined the effect of ATBS content on polymer retention on illite. ATBS is a monomer that is much more resistant to hydrolysis and precipitation than acrylamide and can impart substantial long-term stability to HPAM-type polymers (see SPE 200324). A comparison of the solid blue and black curves in **Figure 5.1.12** reveals that inclusion of only 3-7% ATBS into HPAM dramatically reduced polymer retention on illite with Milne Point injection water (0.22% NaCl, 0.027% $CaCl_2$ and 0.0034% $MgCl_2$)—from 125 µg/g for Flopaam 3630S to only 14 µg/g for Flopaam 5205XV. SNF said that these two polymers provide similar viscosities in Milne Point injection water.

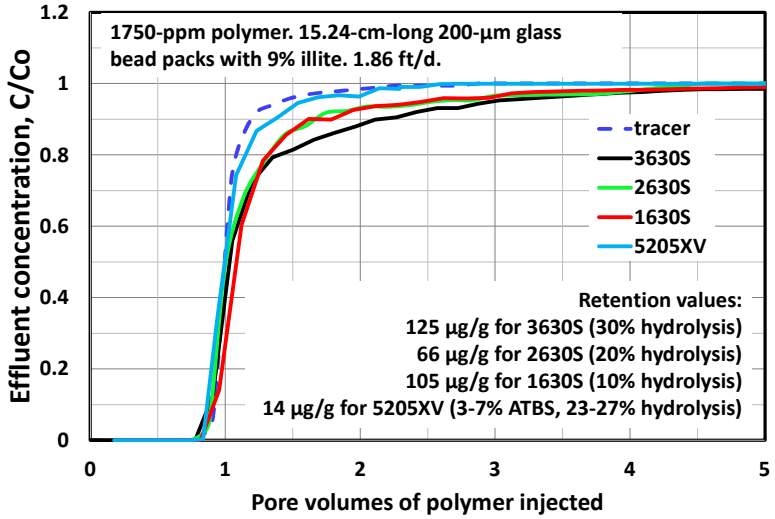

Figure 5.1.12: Polymer retention on illite using Milne injection water.

Based on our results in **Figure 5.1.12**, were performed additional studies to examine the effect of ATBS content on polymer retention on illite in brine with 1.8% NaCl and 0.6% $CaCl_2$. We guessed that any retention differences would be accentuated using this high-hardness brine. **Figure 5.1.13** confirms that polymer retention decreased substantially with increased ATBS content—from 248 µg/g with Flopaam 3630S (0% ATBS) to 70 µg/g with Flopaam 5205XV (3-7% ATBS) to only 3 µg/g for AN125 (25% ATBS). These results suggest that polymer retention (at least on illite) could be dramatically reduced in hard brines by using a polymer with some ATBS in it.

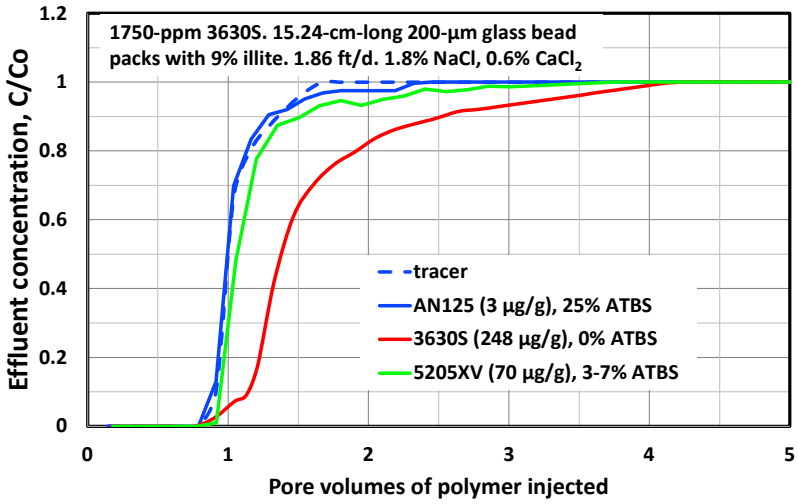

Figure 5.1.13: Effect of ATBS content on polymer retention with a hard brine.

Further confirmation is provided in **Figure 5.1.14**, which compares retention in Milne Point (Schrader Bluff) NB#1 sand for 1750 ppm SNF Flopaam 5205XV (3-7% ATBS) with the same concentration of Flopaam 3630S (0% ATBS). (Both solutions and experiments used Milne Point injection brine.) Polymer retention was effectively zero for Flopaam 5205XV but was 336 µg/g for Flopaam 3630S.

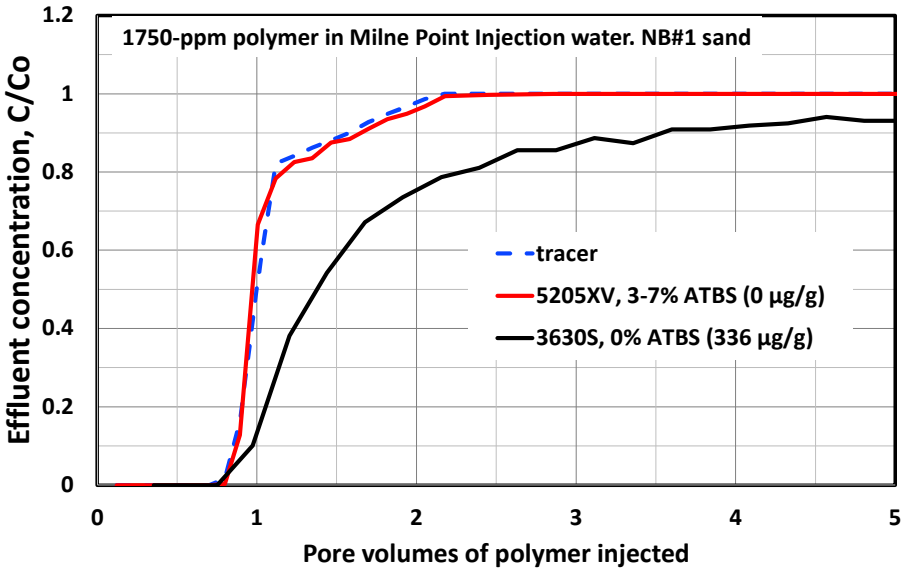

Figure 5.1.14: A small amount of ATBS reduces polymer retention in NB#1 sand.

Effect of mineralogy on polymer retention in a high-hardness brine. Additional experiments were performed to examine the impact of other mineralogies (besides illite) on polymer retention. Again, 1750 ppm Flopaam 3630S was used. These studies focused on the high-hardness brine (1.8% NaCl, 0.6% $CaCl_2$) to accentuate differences in retention. All studies used 9% of the chosen mineral in 200-µm glass bead packs. **Figure 5.1.15** provides the results. A comparison of the dashed and solid green curves reveals that kaolin exhibits the same behavior as illite (215 µg/g vs 248 µg/g total retention). Retention on 9% dolomite or 9% $CaCO_3$ exhibited similar behavior in that (1) total retention values (45 and 59 µg/g, respectively) were much less than on either 9% kaolin or illite (215 and 248 µg/g, respectively) and (2) retention tailing was far less evident than on kaolin or illite. Although the retention curves for dolomite (solid red curve) and $CaCO_3$ appear notably different in **Figure 5.1.15**, this occurred primarily because the water-tracer breakout curves were substantially different. The tracer (and polymer) curves for 9% $CaCO_3$ were more spread out than normal because the pack was more heterogeneous than normal for our bead-pack experiments. In summary, **Figure 5.1.15** reveals that HPAM retention is significantly greater on kaolin and illite than on dolomite or limestone ($CaCO_3$). Also, consistent with our earlier studies (Seright and Wang 2022), the retention tailing effect occurs dominantly with kaolin and illite, rather than with other minerals.

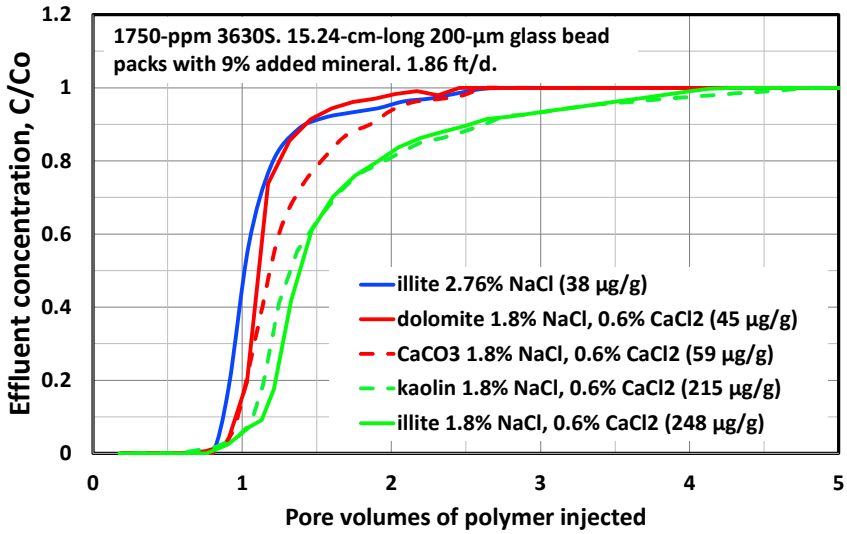

Figure 5.1.15: Impact of mineralogy on HPAM retention with a hard brine.

Main findings of practical significance

Polymer production from Wells J-27 and J-28. Using chemiluminescent nitrogen (Shimadzu TOC-L/TNN-L) to detect HPAM, polymer was first detected October 10, 2020, in Production Well J-27 and December 13, 2020, in Well J-28. Since then, the produced HPAM concentration rose to a maximum of 817 ppm in Well J-27 and 1031 ppm in Well J-28—both on June 21, 2021. Subsequently, produced polymer concentration declined to 528 ppm in Well J-27 as of June 7, 2022, followed by a jump to 665 ppm as of July 22, 2022. In Well J-28, the polymer concentrations appear somewhat stable, with a value of 798 ppm as of September 20, 2022. **Figure 5.1.16** shows all produced polymer concentrations to date.

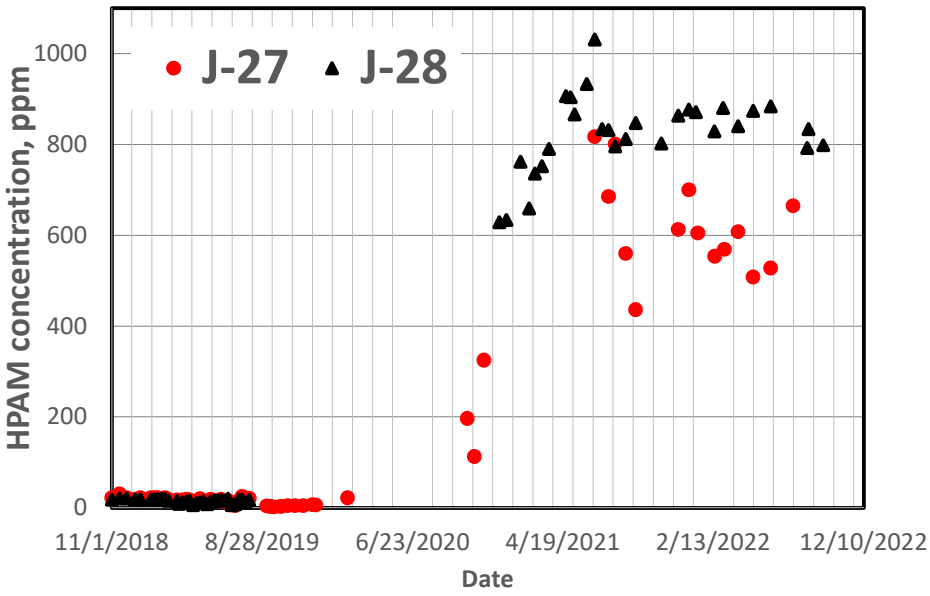

Figure 5.1.16: Produced HPAM concentrations from Wells J-27 and J-28.

Credible prediction of the performance of a polymer flood requires an accurate characterization of oil mobilization, which in turn requires an appropriate representation of polymer retention and propagation through the reservoir. As mentioned earlier, the standard Langmuir isotherm in simulators and the standard assumption of concentration-independent retention in fractional flow calculations cannot correctly describe polymer retention at the Milne Point polymer flood. Our findings suggest a similar concern for any polymer flood where significant levels of illite or kaolinite are present in the reservoir. Mineralogy analysis (especially for kaolinite and illite) is strongly encouraged to reveal whether the tailing phenomenon should be accounted for during simulations of polymer propagation/retention in a given field application.

At the Milne Point polymer flood, HPAM was first detected in both horizontal production wells (J-27 and J-28) after injecting only 10% PV (Dandekar et al. 2021). On the one hand, the fast polymer breakthrough is consistent with our experimental results in the sense that no delay in polymer propagation is evident due to retention. Also consistent with the experimental results, the maximum produced polymer concentration to date is 48% (in J-27) and 59% (in J-28) of the injected concentration. On the other hand, the fast polymer breakthrough is probably due to channeling through a fracture-like feature, rather than via propagation through typical Schrader Bluff reservoir sand. Given the near-unit-mobility displacement provided by the injected polymer solutions, breakthrough would not be expected before injection of 50% PV polymer solution. Thus, definitive field confirmation of the tailing effect will require significant additional time, PV injected, and analysis of produced polymer. As mentioned earlier, we anticipate that the tailing behavior should result in no significant delay in propagation of the polymer bank (and therefore the oil bank), but the effective viscosity and displacement efficiency may be less than originally planned. To reiterate a very positive note, produced water cuts dropped from ~70% during waterflooding before the project

to less than 10% during polymer injection. To our knowledge, no other field polymer flood has resulted in this magnitude of reduction in water cut. At this time, only 18% PV of polymer has been injected, so there certainly is no delayed response to polymer injection.

Because this polymer flood is still in its relatively early stages and because a number of factors influence the current produced polymer concentrations, we cannot yet make definitive conclusions about the actual polymer retention that has occurred within the Milne Point field. Properly assessing retention on a field scale will require significantly more time, polymer throughput, and a methodology like that in Manichand and Seright (2014). Nevertheless, laboratory experiments suggest value in switching to a polymer that contains a small amount of ATBS, to minimize polymer retention in the field application.

Conclusions

1. Laboratory retention studies for the Milne Point polymer flood (North Slope of Alaska) consistently show virtually no delay in polymer propagation, a rapid rise in produced polymer to 70-90% of the injected concentration, followed by produced concentration gradually approaching the injected value over many pore volumes.
2. In contrast, conventional use of the Langmuir isotherm (used in most chemical flooding simulators) or concentration-independent polymer retention (used during fractional-flow calculations) predict a delay in propagation of the polymer front (in proportion to the given retention value), followed by a rapid rise in produced polymer concentration to the injected level.
3. From a practical viewpoint, this tailing behavior means that retention causes no significant delay in propagation of the polymer bank (and therefore the oil bank), but the effective viscosity and displacement efficiency is less than originally planned.
4. In Milne Point cores, over practical ranges of conditions encountered in the field, the presence of the tailing phenomenon was not sensitive to flow rate, polymer concentration, core heterogeneity, or whether the core was preserved, cleaned of oil, or cleaned and re-saturated with oil, or cleaned, re-saturated and aged with oil.
5. Inaccessible pore volume can be overestimated if insufficient brine is flushed through the porous medium between polymer banks. Around 100 *PV* of brine may be needed to displace mobile polymer to approach a true residual resistance factor and properly measure *IAPV*. Even for a sand pack with k_{wsor} = 20 mD, *IAPV* was zero for HPAM with *Mw* of 18 million g/mol.
6. The tailing phenomenon was also observed during mechanistic floods using glass bead packs when sufficient levels of kaolinite or illite were present. This observation was consistent with high levels of illite noted in Milne Point cores.
7. The tailing phenomenon was not noted during mechanistic floods that contained glass beads with montmorillonite, chlorite, calcium carbonate, dolomite, siderite, pyrite, or calcium sulfate.
8. The work suggests that mineralogy analysis (especially for kaolinite and illite) may reveal whether the tailing phenomenon should be accounted for during simulations of polymer propagation/retention in a given field application.
9. A model was proposed to account for the retention tailing phenomenon. Much of the retention data could be fitted to a double-exponential equation, where a relative short reaction accounted for ~70% of the HPAM retention and a longer reaction accounted for the remaining ~30%.

Additional work is needed to elucidate the mechanism associated with the tailing mechanism.

10. Retention is also strongly influenced by the divalent ion content of the water and the ATBS content of the polymer.

Topical publications

1) Seright, R.S. Wang, D. 2022. Polymer Retention "Tailing" Phenomenon Associated with the Milne Point Polymer Flood. SPE Journal 27.

2) *Wang, D., Li, C. and Seright, R.S.: Laboratory Evaluation of Polymer Retention in a Heavy Oil Sand for a Polymer Flooding Application on Alaska's North Slope, SPE Journal, February 2020.*

3) R.S. Seright, New Mexico Inst-Mining & Tech; D. Wang, University of North Dakota, "Impact of Salinity, Hardness, Lithology, And ATBS Content On HPAM Polymer Retention for The Milne Point Polymer Flood", SPE Western Regional Meeting, Anchorage, May 22-25, 2023.

5.2 Optimization of Injection Water Salinity and Identification of Contingencies in Premature Polymer Breakthrough in the Field

Summary. In this section, low salinity polymer flooding, micro-sized preformed particle gel conformance control, in-situ polymer gel conformance control, and optimized polymer injection design though simulation model are explored and discussed. In contrast to high salinity water or polymer flooding individually, the combination of low salinity water and polymer flooding could reach a higher oil recovery. Low salinity prepared polymer can save one third of polymer prepared by formation water. For the particle gel conformance treatment, the oil recovery before and after gel treatment was compared. It was found after gel treatment the water cut was reduced and oil recovery was improved. We also studied the transport behavior of particles, finding a relationship between critical pressure gradient and particle/pore size ratio, in return helping us estimate the maximum possible propagation distance of particles and select the particle size for a desired transport distance. About the in-situ polymer gel treatment, we developed the gelant composition for target low temperature reservoir and studied their injectivity. We noticed that after the gelant was injected, its injection pressure would keep increasing which was opposite with the bottle tests result. This indicated that the micro gel aggregation might have been formed immediately after the polymer and Cr was mixed. In the end, a simulation model of gel propagation in open fractures has been used to design the polymer gel injection volume for the specific well in the pilot.

Introduction. Viscosities for HPAM polymer solutions decrease dramatically with increased salinity and divalent ion content. Polymer retention (adsorption) can also depend on salinity and hardness. For these reasons, low-salinity water is often preferred for polymer flooding. Conventional wisdom argues that polymers are mainly for improved sweep efficiency but have little or no effect on displacement efficiency improvement (i.e., reducing residual oil saturation). In contrast, it has been widely reported that the low salinity water flooding can reduce residual oil saturation significantly in conventional reservoirs by altering formation wettability, but its performance in heavy oil reservoirs is limited due to poor sweep efficiency. Therefore, hybrid injection of low salinity water and polymer may significantly enhance oil recovery in favorable conditions. An important part of this project was to examine the oil displacement mechanisms during low-salinity polymer flooding for the conditions

associated with the Milne Point Unit with the goal of identifying the optimum salinity for use in the field project. The laboratory work elucidated effects due to low-salinity, due to polymer alone, and due to a synergy between low-salinity and polymer.

Early polymer breakthrough is a major concern for the success of a polymer flooding project because it will significantly reduce the efficiency of polymer flooding. This problem could be much worse for heavy oil reservoirs. Polymer gel treatments have often been applied in polymer flooding projects at the beginning, middle, or end of polymer injection to improve polymer injection conformance. Pre-formed particle gels have been widely applied to improve the conformance for water flooding and polymer flooding because they can preferentially enter super-K zones/streaks to reduce their permeability while minimizing the damage of gels in unswept oil-rich zones. It is of significant importance to screen a proper polymer gel that can be used to control the polymer flooding conformance and improve the utilization efficiency of the polymer flooding project while minimizing the penetration of gel on unswept oil-rich zones/areas. To reach the goal, Missouri S&T screened a series of polymer gels for the pilot reservoir based on a series of evaluations.

Design of experiments

The designed and conducted experiments were planned in such a way that enabled qualitative as well as quantitative testing of a multitude of variables such as salinity, water cut, oil types, particles/pore size ratio, flow rate, polymer types, and permeability. The simulated brine was prepared according to the composition of injection brine (SIB) and formation brine (SFB). All the polymer and polymer gel were even and transparent before use, the particles were also swelled to a designed size. **Table 5.2.1** provides a concise summary of all the experiments.

Table 5.2.1: Test matrix for polymer flooding tests to optimize salinity and gel injection behavior studies (and additive).

Parameters /Variables	**Mechanisms**	**Test Fluids and Materials**	**Test Conditions**	**Screening Criteria/ Evaluation of Results**
• Water/Polymer salinity • Sandpack/Core permeability • Oil property • Pore volume • Particle size • Flow rate	• Oil composition (polar component) • Particle/pore size ratio • Permeability contrast • Pressure buildup and release due to	• SIB/SFB • Crude/Mineral oil • Particle gels • Flopaam 3630 of 18-20 million Dalton and 25-30% hydrolysis	• Polymer mother solution diluted to desired concentrations • Room temperature 71°F • Injection flow rate varied	• Oil recovery • Water cut • Pressure gradient • Injection pressure • Gelation time

• Polymer type (Molecular weight, Hydrolysis degree, ATBS content)	particles accumulation and pass • Formation of micro gel aggregation • Electrostatic repulsion	• Flopaam 2330 of 8-10 million Dalton and 20-25% hydrolysis • AN 105 of 6 million Dalton and 5% ATBS • AN 125 of 8 million Dalton and 25% ATBS	from 0.1-50 mL/min • Particle/pore ratio ranged from 0.67 to 1.77	

Summary of key results

Effect of Salinity on Oil Recovery Efficiency. Firstly, the effect of salinity on oil recovery by water and polymer flooding was studied. Low salinity water/polymer flooding after high salinity correlated water/polymer flooding can reduce residual oil saturation by 3-9%. In this process, it was found low-salinity benefit is related to the oil property, the polar composition in oil will make an important effect on the effectiveness of LSP flooding.

(a) Oil Recovery Performance. Table 5.2.2 and **Figure 5.2.1** summarizes the incremental oil recovery performance core-flooding experiments performed. In these experiments, 3-9% additional oil was recovered from tertiary low-salinity water flooding performed after high-salinity water flooding using native NB sand (from the depth of 3755 ft from Well Liviano-01A). Also, extra oil was recovered from low-salinity polymer flooding (3630S, 45 cp) after high-salinity polymer flooding with the same viscosity. By contrast, no additional oil was recovered from low-salinity polymer flooding when mineral oil was used as the oil phase, as shown in **Figure 5.2.2**. The results suggest the low-salinity benefit is related to the oil properties.

Table 5.2.2: Summary of oil recovery performance.

Sand	Conditions	No.	Incremental recovery, % OIIP			
			LSW after HSW	HSP after HSW/LSW	LSP after HSW/LSW	LSP after HSP
Silica sand	Salinity=4945 ppm 50-1400 mD	7	1-6	4-5	8-12	No tests in this way
NB sandpack	From well Liviano-01A Depth: 3755’	10	3-9	5-8	10.6 (one test)	3-9

	200-16,000 md					
NB sandpack (cleaned)	From well Liviano-01A Depth: 3755' Cleaned with solvent Mineral oil (173 cp)	1	No tests in this way	13 (one test)	No tests in this way	0.7 (one test)
NB core plug (cleaned)	From well Liviano-01A Depth: 3760' Received in cleaned condition	4	No tests in this way	No tests in this way	9.1 (one test)	No tests in this way

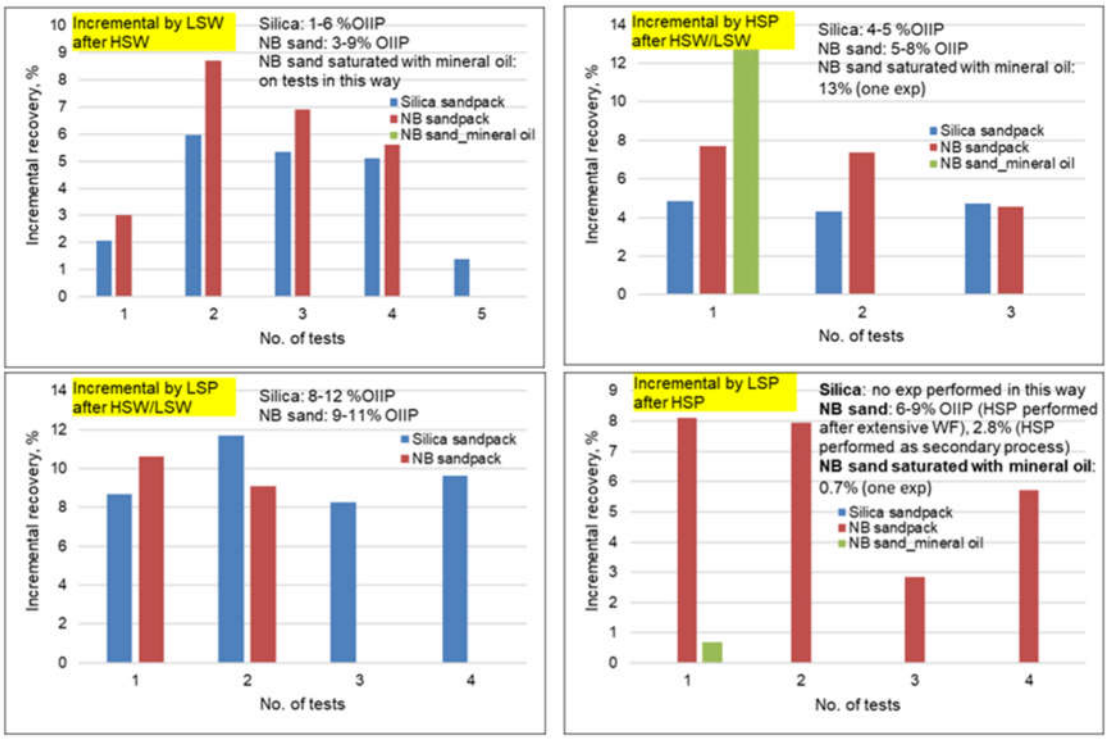

Figure 5.2.1: Summary of oil recovery performance at various conditions.

(b) Influencing Factors on the Effectiveness of LSP Flooding. To demonstrate the influence of the oil properties, we performed experiments with heavy mineral oil instead of the crude oil. The viscosity of the mineral oil (173 cp) was comparable with the crude oil (202 cp). Note that LSW flooding was not performed before the LSP flooding. In this circumstance, the low salinity effect during the LSP flooding was expected to be more prominent. However, the results show that no appreciable incremental oil was achieved by the LSP flooding (only 0.73% OOIP) after extensive HSP flooding. The mineral oil was composed of paraffin and contained no polar components. The coreflooding

results indicate that the composition of the oil is an important influencing factor on the effectiveness of LSP flooding.

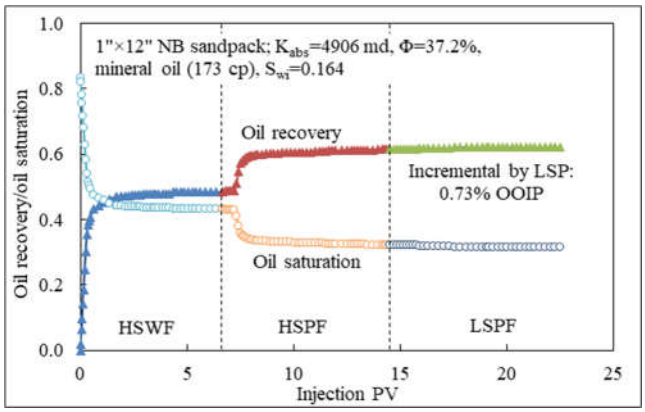

Figure 5.2.2: No beneficial effect when saturated with mineral oil.

In a real reservoir, the flooding pore volume is very limited for the major portion of pore space. Also, there may be local and global heterogeneities present in the reservoir. It can be reasonably concluded that except for the near wellbore region and the water-preferential channeling zones, the large portion of the reservoir cannot really reach the true residual oil saturation (Sor). Therefore, instead of focusing on the theoretical true Sor, it would be more practically meaningful to compare the water cut level and cumulative oil recovery factor after given pore volumes. The results shown in **Figure 5.2.3** indicate that LSW generally has a lower water cut and higher oil recovery at a given finite pore volumes of flooding.

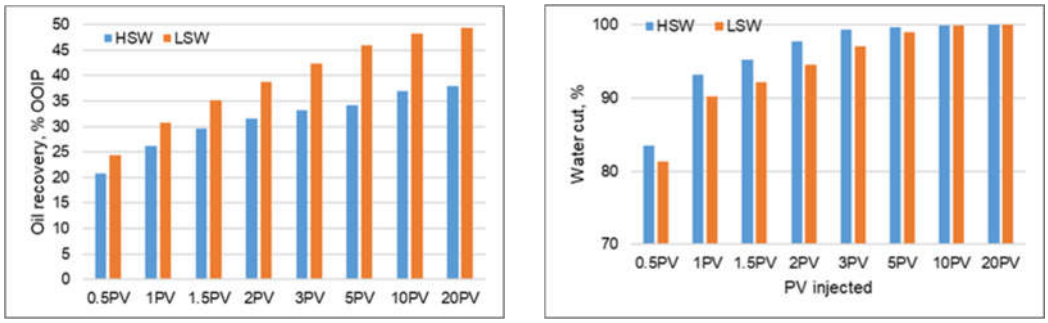

(a) Oil recovery (b) Water cut

Figure 5.2.3: Oil recovery water cut after given pore volumes of LSW flood or HSW flood.

Micro-sized Particle Gel Conformance Control Treatment. Due to the existence of fractures, conduits, and high permeability channels, the heterogeneity is normal in formation which can result in an unsatisfactory recovery performance and a low oil recovery rate. To solve this problem micro-sized particle gel was injected to plug the high permeability zone and divert the polymer flow into the matrix. Therefore, the oil recovery before and after gel injection was compared to verify its effect. We also studied the transport behavior of particles, finding a relationship between critical pressure gradient and particle/pore size ratio, in return helping us estimate the maximum possible propagation distance of particles and confirm the wanted particle size for a desired transport distance.

(a) Oil Recovery Performance before Gel Treatment. Table 5.2.3 summarizes the basic conditions and key results of the experiments. As a base case, the results obtained from the model with the channel filled with 20/30 mesh (0.60-0.84 mm) sand are discussed in detail (Exp #4). In this experiment, the permeability of the channel and the matrix was 57 and 0.50 D, respectively. Another experiment was carried out using homogeneous core with a comparable permeability (Exp #1). In this study, we use the permeability contrast (Kc/Km) between the channel and the matrix to quantify the heterogeneity severity of the model. Another parameter, R_{FC}, is also introduced to estimate the heterogeneity severity of the model. The R_{FC} is defined as the flow capacity ratio of the channel to that of the matrix. A higher R_{FC} indicates more flooding fluid would just flow through the channel, rather than through the matrix to effectively displace the majority remaining oil there. For the channel model, the permeability contrast (Kc/Km) was 114 and the flow capacity ratio, R_{FC}, was 7.4, while Kc/Km=1 and R_{FC}=0 for the homogeneous model.

Table 5.2.3: Summary of the experiment results.

Exp #	Sand	Heterogeneity	Km, D	Kc, D	Kc/Km	R_{FC}	Water breakthrough, PV_t	Oil recovery (% OOIP)		
								WF at f_w=80%	PF	Overall
1	Homo	Low ↓ ↓ High	0.86	0.86	1	0	0.24	49.0	22.7	72.9
2	60-80		0.52	19.6	38	2.6	0.20	29.3	36.7	67.7
3	30-60		0.64	31.0	48	3.2	0.11	19.0	32.1	58.4
4	20-30		0.50	57.0	114	7.4	0.10	16.7	32.1	48.9
5	10-20		0.49	237	484	30.0	0.09	10.8	22.7	34.7

Figure 5.2.4 shows the oil recovery performance of water flooding and extensive polymer flooding. Compared with the homogeneous model, the water breakthrough in the channel model occurred much earlier (0.10 PV versus 0.24 PV), and the secondary recovery from waterflooding was much lower (16.7% versus 49.0%). Note that the pore volume of the channel (CPV) was about 13% of the total pore volume. Most of the injected water transported through the super-k channel and most of the recovered oil was from the channel. The majority oil in the matrix was bypassed. In the polymer flooding process, the pressure buildup was much lower in the channel model. Although significant incremental oil was recovered from both models (32.1% and 22.7%), substantial difference was observed after a closer examination. As shown in **Figure 5.2.4**, the incremental oil was recovered gradually over quite a long period of polymer flooding (more than 4 PV) in the channel model. Note that after switching to polymer flooding, although the water cut declined, it would quickly increase back to a high level, making the production process uneconomical. The channel model would reach a water cut of 90% after 0.64 PV of polymer flood, and the oil recovery factor was only 34.0%. In contrast, the homogeneous model would achieve an overall oil recovery factor of 70.5% when the water cut rose to 90%. Clearly, the unsatisfactory recovery performance in the channel model indicates that the oil bank generated by the polymer flood was much less concentrated, and the oil production rate was much slower. Therefore, the impact of heterogeneity was significant and polymer flood alone was insufficient to attack the excessive water production and achieve a satisfactory oil

recovery performance. Additional conformance treatment effort was required to shut off the super-k channel and force the displacing fluid into the matrices.

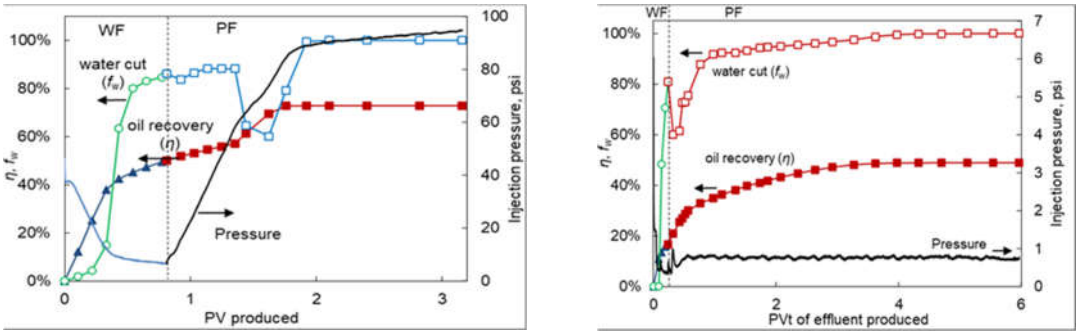

(a) Channel model before gel treatment (Exp #4) (b) Homogeneous model (Exp #1)

Figure 5.2.4: Comparison of oil recovery in channel model and homogeneous model.

(b) Oil Recovery Performance after Gel Treatment. Oil recovery performance after gel treatment is shown in **Figure 5.2.5**. For the base case (Exp #4, Figure c), the water cut was significantly reduced (from 100% to 70%). Also, the water cut could be maintained at a relatively low level for an appreciably long period of flooding (~1 PV with fw<98%), and the sweep efficiency and overall oil recovery were improved (by 18.0% OOIP). The noticeable improvement indicates the subsequent flooding fluid was diverted into the matrices to displace the previously bypassed oil. For the worst case (Exp #5, Figure d), after the gel treatment, the water cut was reduced to 63%, and the oil recovery factor was increased from 34.7% to 56.1%. The results demonstrate the effectiveness of the tested microgels under the conditions of these two experiments. For the 30/60-mesh-sand-filled model (Exp #3, Figure b), the improvement was limited, only 2.7% OOIP. The injected gel volume was insufficient, and no gel was produced. The gel was not successfully injected into the channel and a gel bank was not formed. Consequently, the water cut first reduced and then rapidly increased after a short period during the post polymer flooding. In the first 0.1 PV, the polymer was forced into the matrix at the front section of the model. After transporting for a distance, the polymer solution would crossflow back into the channel as the gel was not tightly packed in that section. For the 60/80-mesh-sand-filled model (Exp #2, Figure a), the channel had a lower permeability of 19.6 D. The heterogeneity was not as serious as the other models. The overall oil recovery performance before the gel treatment was comparable with the homogeneous model. However, in the latter case, the oil bank established during the tertiary polymer flooding was more concentrated and exhibited a better timing effect. During the gel treatment, the microgel particles were harder to penetrate the channel, and higher injection pressures were required. A total of 11.4 CPV of gel dispersion was injected with no gel particles produced out at the outlet. The gel injection was stopped as the injection pressure reached the equipment limit. Still, we observed appreciable incremental recovery, 15.9% OOIP, after the gel treatment, resulting in an overall recovery factor even higher than in the homogeneous model. This is not surprising as the injection pressure was much higher in this experiment. The high injection pressure gradient indicates the difficulty of the microgel particles in transporting in the channels with lower permeabilities.

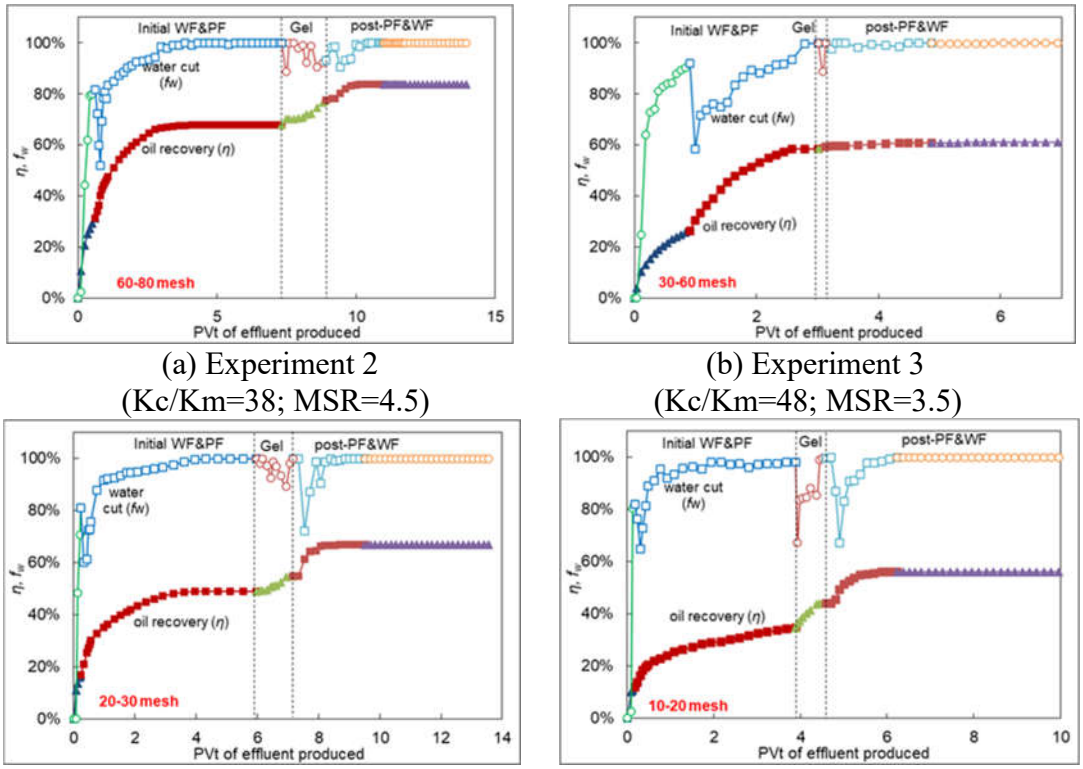

(a) Experiment 2 (Kc/Km=38; MSR=4.5)

(b) Experiment 3 (Kc/Km=48; MSR=3.5)

(c) Experiment 4 (Kc/Km=114; MSR=2.6)

(d) Experiment 5 (Kc/Km=484; MSR=1.2)

Figure 5.2.5: Water cut and oil recovery after gel treatment with matching-size ratio.

(c) Critical Pressure Gradients during Microgel Propagation. In these experiments, sandpacks were used as the super-K porous media, which mimicked the super-K channels present in reservoirs. Six experiments were conducted, in which the permeabilities ranged from 55.4 to 221 D. The basic information of the sandpacks is summarized in **Table 5.2.4**.

Table 5.2.4: Summary of basic information of the experiments.

Exp #	k, D	Gel size, μm	Gel strength	Particle/pore ratio	Carrying fluid
1	55.4	260	Soft	2.35	Injection brine
2	60.0	150	Soft	1.31	Injection brine
3	221	150	Strong	0.69	Formation brine
4	62.0	130	Strong	1.11	Formation brine
5	62.4	150	Strong	1.28	Formation brine
6	59.8	206	Strong	1.77	Formation brine

Taking Exp #2 as an example, the permeability was 60 D, and the particle/pore ratio was 1.31. At the beginning, gel dispersion was injected at 2 ml/min (19.2 ft/d) for about 6 pore volumes (PV). As shown in **Figure 5.2.6**, the pressure gradients in different sections were sequentially increased and stabilized (with fluctuations). Afterwards, the flow rate was increased to 50 ml/min (481 ft/d),

sequentially decreased to 0.2 ml/min (1.9 ft/d), and then successively increased back to 50 ml/min. The pressure gradients in the second section (between the first and second internal pressure taps) of the sandpack are shown in **Figure 5.2.7**. The pressure gradient was much less sensitive to the superficial velocity of the gel dispersion compared with a Newtonian fluid. The gel dispersion behaved like a pseudoplastic fluid when transporting through the porous channels. The slip effect and the breakage of the gel particles into smaller pieces were possible reasons responsible for the apparent shear thinning behavior. The pressure gradient data was fitted with the equation in the form of **Equation 5.2.1** to determine the critical pressure gradient (∇Pcr). The physical meaning of ∇Pcr was the pressure gradient at the superficial velocity of zero. It was the minimum pressure gradient to initiate the propagation of the gel particles in the porous media. The critical pressure gradient was 32.63 psi/ft in Exp #2.

$$\left|\nabla P\right| = \nabla P_{cr} + a \cdot u^{b} \tag{5.2.1}$$

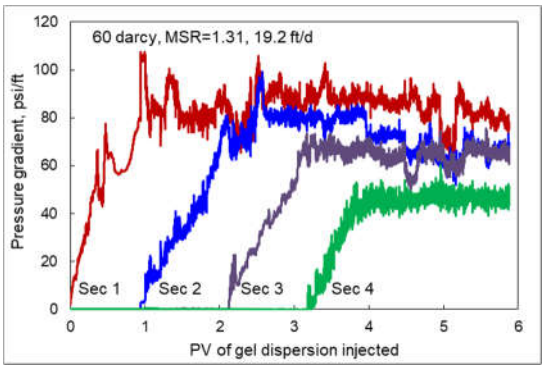

Figure 5.2.6: Pressure gradients during gel injection (Exp #2).

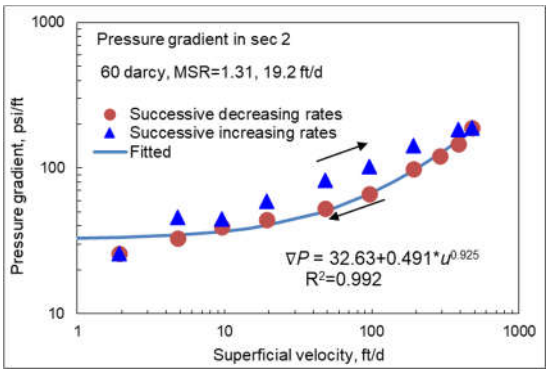

Figure 5.2.7: Pressure gradients at different superficial velocities (Exp #2).

During the experiments we also observed that the particle/pore ratio had a significant impact on the critical pressure gradient. As the matching size of the gel particles was a crucial design parameter for gel treatment in field applications, it was practically meaningful to study the impact of the particle size on the critical pressure gradient. In **Figure 5.2.8**, the critical pressure gradients during gel injection were plotted against the particle/pore ratio. The experimental data covers the particle/pore ratio in the range from 0.67 to 1.77.

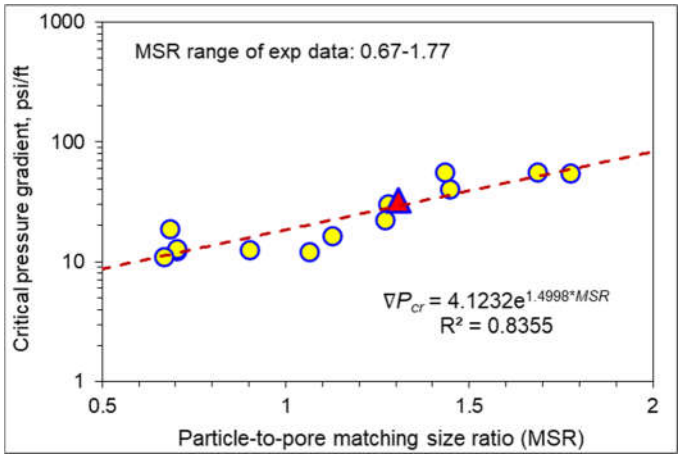

Figure 5.2.8: Correlating the critical pressure gradient with the particle/pore ratio.

As shown in this figure, the critical pressure gradient followed an exponential relationship with the particle/pore ratio. The critical pressure gradients were generally below 60 psi/ft at the particle/pore ratios below 2. When the particle/pore ratios were lower than 1 (i.e., the particles smaller than the pore throats), the critical pressure gradients were roughly below 20 psi/ft. The low particle/pore ratios represented the desired situations in the channels to be treated. Low pressure gradients were necessary to allow easy propagation and placement of the gels in the channels. The critical pressure data could be described quite well with an exponential equation (**Equation 5.2.2**).

$$\nabla P_{cr} = 4.1232 \exp\left(1.4998 R_r\right), R_r < 2. \tag{5.2.2}$$

In the equation, R_r was the particle/pore ratio. This correlation could predict the critical pressure gradients of the microgels at other matching size conditions in the validated range. This could be used to estimate the maximum possible propagation distance of gels in the channels. The basic principle was that the gel particles would stop propagating when the driving pressure gradient at the frontal section was insufficient to overcome the required critical pressure gradient. The procedure was illustrated with a simple schematic horizontal injector-producer pair, which is shown in **Figure 5.2.9**. A super permeable channel connected the horizontal injector and the producer. As a base case, we assume the maximum allowable bottomhole pressure in the injector was 2500 psi, and the average reservoir pressure was 1750 psi. Thus, the maximum allowable driving differential pressure was 750 psi. As the channel had superhigh permeabilities compared with the matrices, in the conceptual simulation, we assumed linear flow in the super-k channel, and the near-wellbore radial flow was neglected. Based on the relationship between the critical pressure gradient and the particle/pore ratio, the transport distances of the microgel particles at different particle/pore ratios were obtained, as shown in **Figure 5.2.10**. It was straightforward that the propagation distance decreased with the particle/pore ratio at a given differential driving pressure.

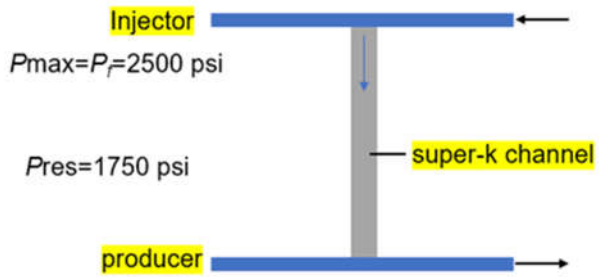

Figure 5.2.9: Schematic diagram of the horizontal pair and super-k channel.

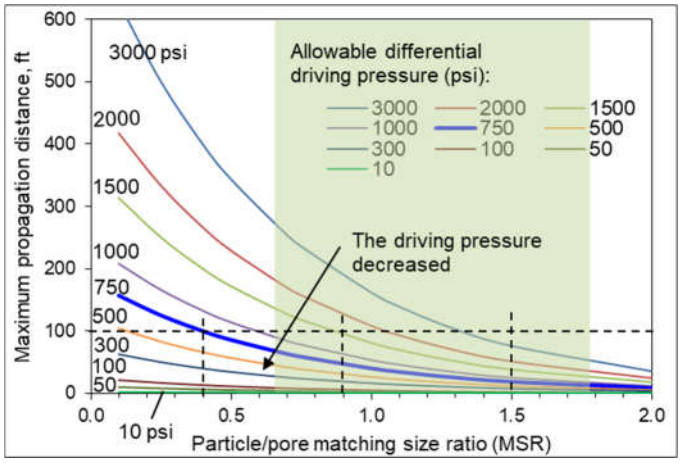

Figure 5.2.10: Diagram of the maximum transport distances in superpermeable channels.

(d) Study of Transport Behavior of Microgel Particles. The injection pressure during the gel treatment process is shown in **Figure 5.2.11**. According to the pressure behavior, the gel injection process exhibited three different stages. In the first stage, the injection pressure steadily increased with no fluctuation. In the second stage, wild pressure fluctuation was observed with an upward trend. Afterwards, gel would break out at the outlet, and the pressure would jump around a relatively constant value, 240 psi. At the beginning, leak-off took place at the face of the channel model. The carrying fluid would leak off into the matrix and the channel, while the gel particles would be left behind at the surface. As more gel particles accumulate at the surface, a cake would be formed, and the injection pressure would climb up. The cake would continue to grow stronger as the injection pressure increased. A check of the channel model showed that a sticky filter cake was formed at the inlet face. **Figure 5.2.12** (a) shows the photo of the cake formed at the inlet face, which confirms the occurrence of leak-off during gel injection. The leak-off and formation of the filter cake is further illustrated in **Figure 5.2.11** (b). The cake would prevent the gel particle from penetrating the matrices (oil zones). The gel cake can be easily removed by soaking with breaker after the gel treatment to resume the production. Otherwise, the oil zones would be catastrophically damaged if gel particles penetrate a significant distance into the oil zones.

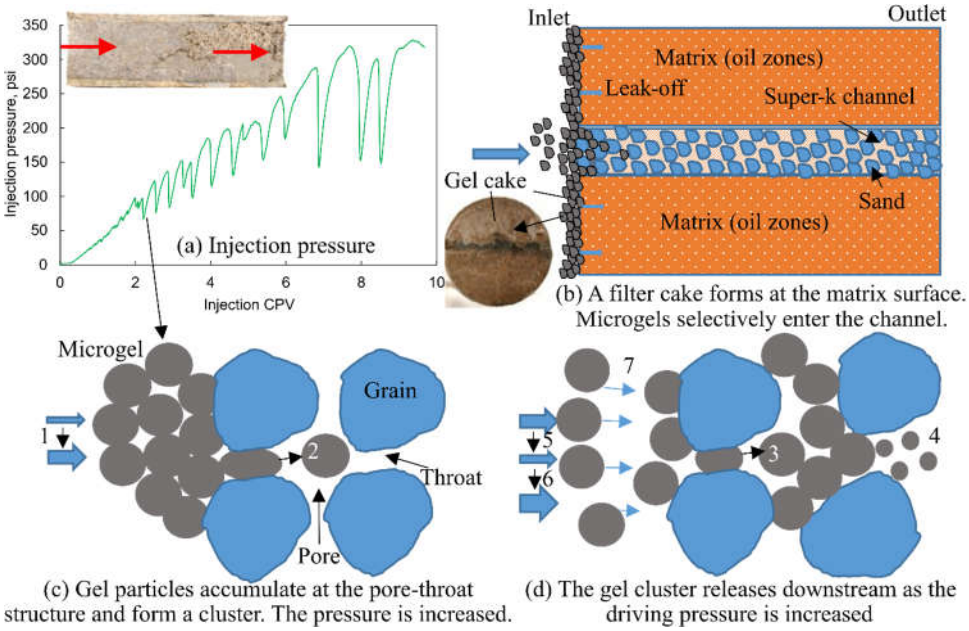

Note: 1. Pressure buildup as microgel particles accumulate. 2. Deform and pass. 3. Shrink/deform and pass. 4. Break and pass. 5. Pressure released as the gel cluster breaks out downstream. 6. Pressure buildup as released particles re-accumulate and upstream particles arrive and accumulate. 7. Upstream gel particles occupy the vacancy left by released particles. The repeated particle accumulation and release are in accordance with the pressure fluctuations.

Figure 5.2.11: Injection pressure and schematic diagram of gel transport behavior.

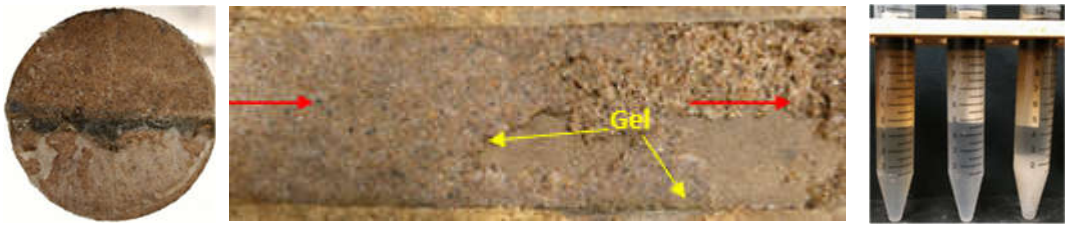

(a) Filter cake (b) Gel placement in the super-k channel (c) Gel produced

Figure 5.2.12: Filter cake at inlet surface and gel placement in the super-k channel (Exp #4).

<u>Polymer Gel Conformance Control Treatment</u>. To solve early polymer breakthrough problem in-situ polymer gel treatment will be another choice to improve polymer injection conformance. It is important to screen a proper polymer gel that can be used without causing serious formation damage. For this purpose, we tested a series of polymer gels based on bottle tests and injectivity studies. Provided from SNF Floerger, 5 different polymers were evaluated according to their molecular weight, hydrolysis degree, and ATBS content, the detailed information is listed in **Table 5.2.5**. The crosslinker we used to crosslink polymer chains was chromium acetate containing 24% active Cr^{3+}. From bottle tests gelation time can be obtained and gelant injection pressure could be analyzed through injectivity studies. Before the test, the gelant injection pressure was expected to be same as polymer and will not increase until the gelation process started which was expressed as gelation time. But our results indicate that the injection pressure of gelant prepared by some polymers (3630, 2330, and AN 105) will increase immediately after it was injected which will require a higher injection

pressure and may cause formation damage problem. In other words, it is critical to choose a proper polymer to prepare the gel.

(a) Bottle test results. In experiments, all the dry polymers were dissolved in simulated injection brine (salinity was 2500mg/L) firstly to prepare a 5000mg/L polymer solution. Then totally 125 mg/L Cr^{3+} was added into the polymer solution. After shaking and stirring, a transparent and homogeneous gelant solution was obtained. Keep observing the gelant appearance and recording the gel strength code according to Sydansk Gel Strength Codes. When the strength code turned from A to C (viscous solution to flowing gel) regard it as gelation time. The gelation time result for each polymer gel is listed in **Table 5.2.5**. It was found that polymer 3630 have the shortest gelation time due to the highest molecular weight and hydrolysis degree; the gelation rate of AN 125 is the slowest resulting from a low molecular weight and more importantly, the high ATBS content.

Table 5.2.5: Gelation time for different polymer gels.

Exp #	Polymer	Mw (Million Dalton)	Hydrolysis (%)	ATBS (%)	Gelation time (d)
1	3630	18-20	25-30	0	2.5
2	2330	8-10	20-25	0	5.0
3	AN 105	6-8	0	5	7.0
4	AN 125	8	0	25	20.0

(b) Effect of polymer types on gel injectivity. To evaluate the polymer gel that can be used to control the conformance of polymer flooding for the heavy oil reservoirs, the polymer and gel were injected while the pressure was recorded and compared. The gelant and polymer injection pressure were assumed to be same as each other based on their similar viscosity before the gelant viscosity started to increase. However, through the previous study we found the gelant injection pressure will keep increasing once it was injected. But, we also noticed that if ATBS was contained in polymer and only if the ratio of it was high enough, the injection pressure will not change. To study the effect of polymer types on injectivity, gelant prepared by 4 different polymers were injected, and the pressure results were compared. During the flooding test polymer concentrations were 5000mg/L, Cr concentrations were 125mg/L, brine salinity was 2500mg/L, and the core permeability was around 1D. The detailed information is summarized in **Table 5.2.6**.

Table 5.2.6: Information of the injectivity experiments.

Exp #	Polymer	Cp (mg/L)	C_{Cr} (mg/L)	Salinity (mg/L)	K (mD)
1	3630	5000	125	2500	857
2	2330	5000	125	2500	9208
3	AN 105	5000	125	2500	821
4	AN 125	5000	125	2500	710

The injectivity results are shown in **Figure 5.2.13**. On the one hand, the injection pressure of gelant was always higher compared with polymer when 3630 or 2330 were used. After the gelant was

injected, the injection pressure kept increasing which indicated that the micro gel aggregation might be formed after polymer and crosslinker was mixed. On the other hand, this increase would become slower and smaller if there are some ATBS contained in polymer molecules, and even vanished when ATBS content was high enough due to the protecting effect of SO_3^- group. The whole -$C(CH_3)_2CH_2SO_3^-$ group needs to be hydrolyzed to -COO^- group firstly and then can be crosslinked by Cr^{3+} ion. The results inform us if gelant made with 3630 or 2330 were used to control the conformance, the required gelant injection pressure must be high enough to overcome the injectivity problem. Consequently, the gelant cannot go in depth and may cause formation damage problem. Meanwhile, the injection pressure of gelant prepared with polymer 2330 was lower than that of 3630. This is because polymer 2330 has a shorter polymer chain and a lower hydrolysis degree resulting in a smaller aggregation size and a slower gelation rate.

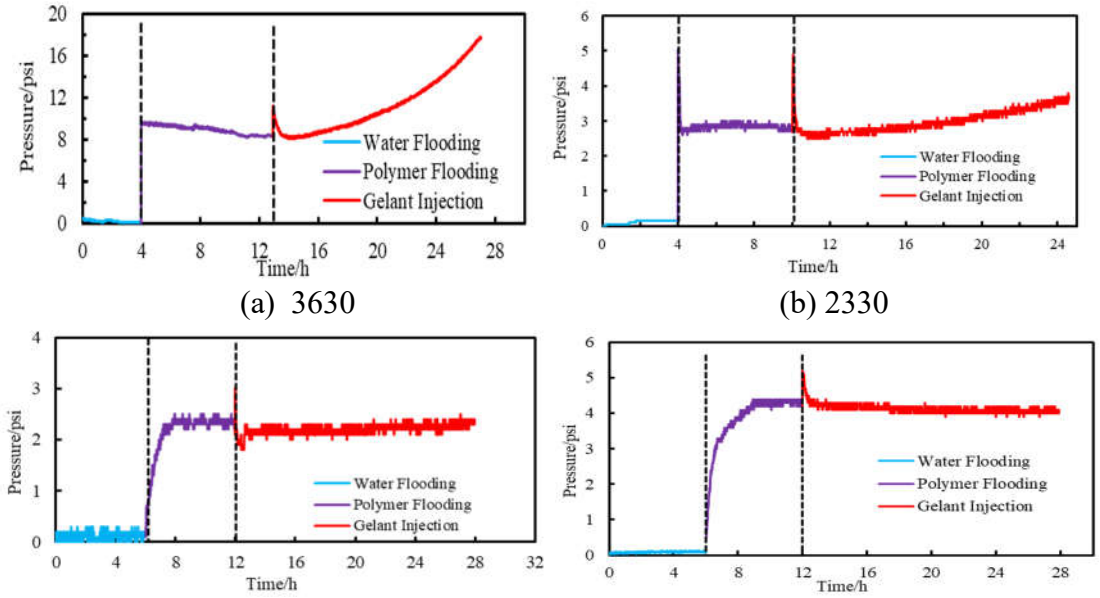

Figure 5.2.13: Injection pressure of gelant prepared by different polymers.

(c) Effect of matrix permeability on gel injectivity

After knowing the fact that the injection pressure of gelant prepared by polymer 3630 will keep increasing after it was injected, whether matrix permeability will make an effect was studied. For this purpose, gelants made by a same recipe were injected in cores with different permeabilities (180 mD to 21 D). The basic parameters are listed in **Table 5.2.7**.

Table 5.2.7: Basic parameters for permeability effect study.

Exp #	Polymer	Cp (mg/L)	CCr (mg/L)	Salinity (mg/L)	K (mD)
1	3630	5000	125	2500	180
2					857
3					1778
4					21,000

As shown in **Figure 5.2.14**, although the permeability was as high as 21 D the gelant injection pressure still kept increasing immediately after it was injected. Even the pressure curve shapes were also very similar; after 16 hours the injection pressure increased by 2-3 times than polymer flooding pressure. Unfortunately, this is undesired result for the application of this gel. Because if this gel was used to adjust the water conformance between two layers the permeability of the gel cannot go in deep and when the injection pressure increased to a certain value, the gelant started to flow into low permeability zone and cause the formation damage.

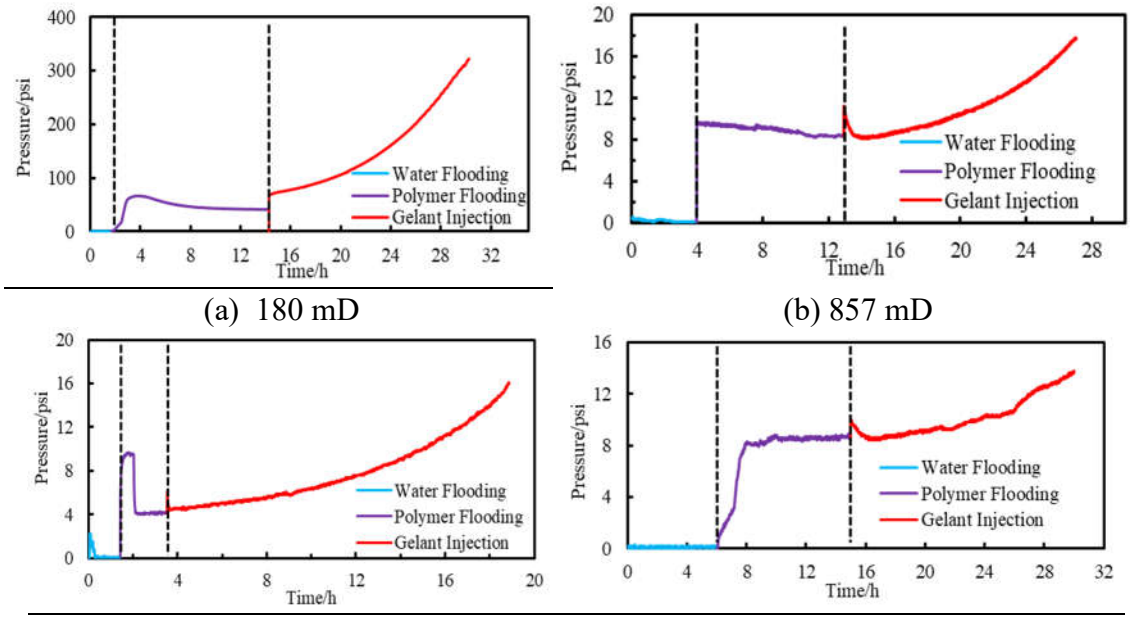

(a) 180 mD (b) 857 mD

(c) 1778 mD (d) 21 D

Figure 5.2.14: Effect of permeability on gelant injection pressure.

(d) Effect of brine salinity on gel injectivity

Through comparing the injection pressure of gelant prepared by different salinity brine, one was SIB whose salinity was 2500mg/L and another one was SFB with a salinity of 27,500mg/L, as **Figure 5.2.15** shows, it was found that the gelant injection pressure would increase much faster at high salinity condition. After injecting the gelant for 16 hours, the pressure of gelant made by SFB was around 300 psi while the pressure at low salinity condition was only 18 psi. We also found a thin gel accumulation layer formed on the inlet surface (shown in **Figure 5.2.15** b) at high salinity condition. However, nothing was found when SIB was used to prepare the gelant. Both the injection pressure result and gel accumulation phenomenon indicate that the gelation rate at high salinity condition will be faster than low salinity which is also consistent with the bottle test results. Resulting from the high salinity which also represents a higher counter ion concentration, the electrostatic repulsion between inter-molecules decreases and the distance between chains decreases, the electrostatic repulsion in intra-molecule also decreases which is favorable for the uptake process. Consequently, the gelation process was accelerated, and the injection pressure increased faster.

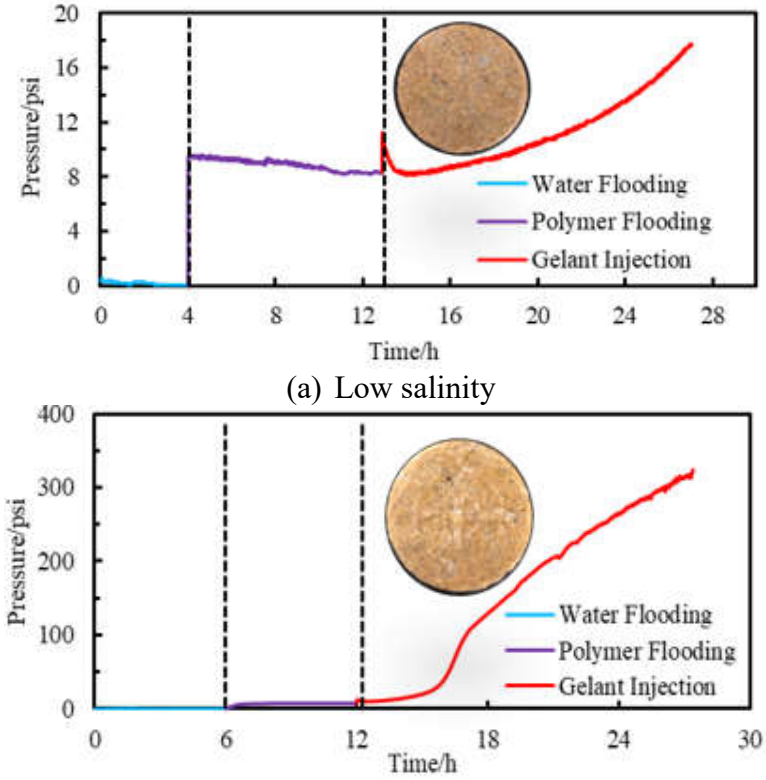

(a) Low salinity

(b) High salinity

Figure 5.2.15: Effect of salinity on gelant injection pressure.

Optimized Design of Polymer Gel Injection for the Pilot using a Conceptual Simulation Model.

We conducted numerical simulation using a conceptual model to provide an optimized design for the pilot test based on the lab results, water/polymer flooding performance, and reservoir characterizations. The conceptual model contains two horizontal wells as partitions of J-23A (Injector) and J-28 (Producer). The model size is 1500 ft * 100 ft * 20 ft as a partition of sector A. An open fracture with width 0.37 mm in that section was reported by UND based on calculations of tracer results. Therefore, the base case of the conceptual model contains a 0.37 mm (14 d-ft) fracture from well to well. The matrix has permeability of 1050 md and porosity of 0.236. The model illustration is shown in **Figure 5.2.16** (a).

Due to existence of fractures and premature breakthrough of water/polymer flooding, we identified that a gel treatment was a necessary option to control driving phase conformance. However, design of gel injection for the pilot is complicated due to many factors influencing gel volume for placement. The key factors include gel rheology, retention, dehydration, injection rate, penetration depth and fracture width. To consider these factors correctly in pilot design, we first conducted simulation on core scale to history match the results that measured in lab experiments and then upscaled the model to field scale.

As mentioned in previous sections, gel cannot enter matrix but forms a filter cake on fracture surface and water in gel system can leak-off to the matrix. Thus, the concentration of retained gel in the filter cake and pressure gradient can increase with more and more gel injected. Besides, with more gel retained in the fracture, the breakthrough is delayed (in fracture pore volume FPV). As a result, we first fitted a gel rheology model to quantify the gel viscosity variation during propagation in fractures based on the pressure gradient. Second, we fitted a gel retention model with higher retention capacity on fracture surface to quantify the dehydration behavior, based on the breakthrough time. After gel cake is formed and packed in fractures, the later injected gel will be fingering through the packed gel and the transport pathway is more like turbulent instead of laminar flow. Thus, in third step, a conversion model of effective shear rate in turbulent flow was considered to better simulate gel propagation in fractures. Fourth, a scale up model was developed to consider uncertainties in pilot such as the fracture width. Fifth, based on the simulation model, we predicted the gel volume required to place gel into varied penetration depth in open fractures with varied fracture widths. The procedures have been summarized in **Figure 5.2.16** (b).

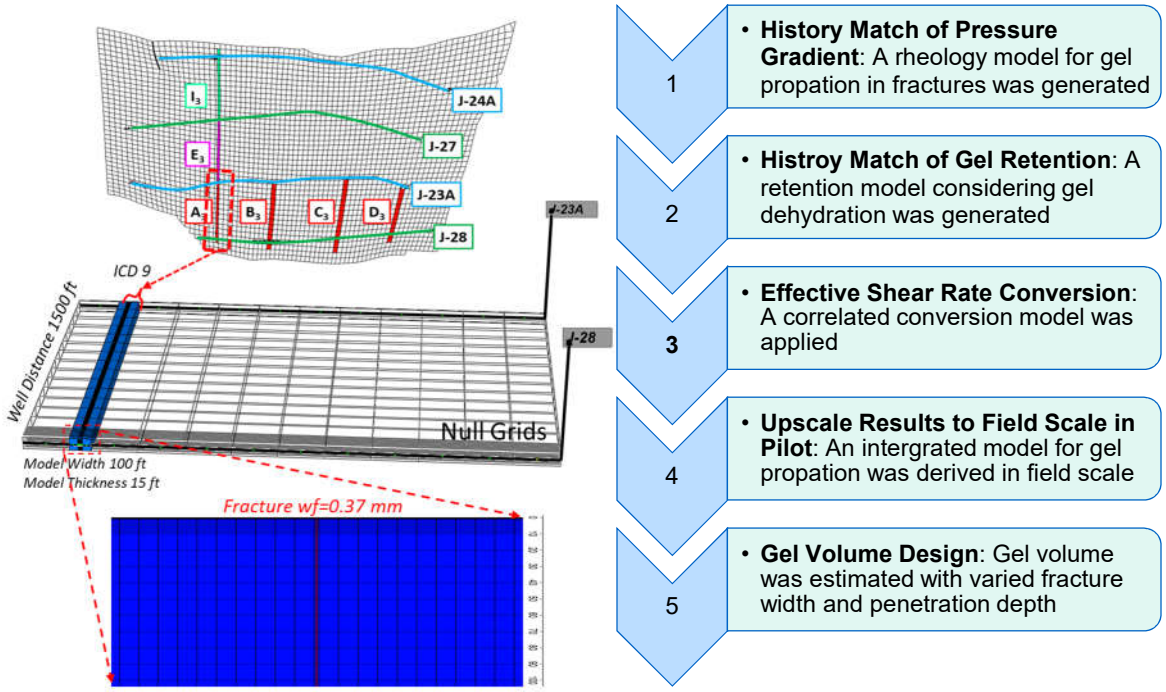

(a) Simulation model setup in field scale (b) Procedures of gel treatment design

Figure 5.2.16: Optimized gel treatment design.

In this study, we have proposed the upscaled simulation model for gel propagation in fractures including a rheology model, a retention model, and a shear rate conversion model. The parameters in each model are fitted in history matching of lab experiments provided by Seright (1998). Rheology model is shown in **Equation 5.2.3**, where μ_0 is reference viscosity, μ_{ref} is reference effective velocity, μ_g is gel apparent viscosity, and n_{thin} is shear coefficient, u is velocity. In this study, we have μ_0=2550 cp, μ_{ref} =40.68 ft/d, n_{thin} =0.32.

$$\mu_g = \mu_0 * \left(\frac{u}{u_{ref}}\right)^{n_{thin}-1} \tag{5.2.3}$$

Retention model is shown in **Equation 5.2.4**, where R_c is retention capacity in lbmole/ft^3 due to dehydration, W_f is fracture width in inch, Q is flow rate in ft^3/d, and α, R_{c1}, R_{c2} are tuning factors based on lab results. In this study, α =0.0017, R_{c1}=-1.359, R_{c2}=-0.454.

$$R_c = \alpha * W_f^{Rc1} * Q^{Rc2} \tag{5.2.4}$$

A conversion model for effective shear rate is proposed based on the theory in (Seright, 1988) that assumed the residual fracture volume after gel retention was like porous media. Thus, the correlated relationship between velocity and effective shear rate is shown in **Equation 5.2.5**, where porosity Φ is obtained empirically and in this study, we used 4% to 14% as indicated in lab experiments (Seright, 1999), K is effective permeability of gel cake calculated by empirical equation K=0.0011+(C/C_0)$^{-3}$.

$$u = shear\ rate * \sqrt{\emptyset K} \tag{5.2.5}$$

With the proposed gel propagation model in fractures, the design of gel treatment in pilot can be achieved.

The design of gel volume in this study assumes that: (1) the gel cannot penetrate into matrix and can only form a filter cake on fracture surface; (2) gel retention is an instantaneous process without kinetics considered; (3) gel rheology only applies to flowing gel and after retained, gel is immobile. The gel volume design results are shown in **Figure 5.2.17**. The consumed gel volume is scaled using Y-axis in FPV. The results show that the gel volume can increase logarithmically with penetration depth in fractures. Besides, the results also show that gel can be dehydrated more in narrower fractures because more gel is consumed in narrow fractures such as W_f = 0.37 mm than that in wide fractures such as W_f=5 mm. Based on our results, we can predict the design of gel injected in pilot to reach certain depth in fractures.

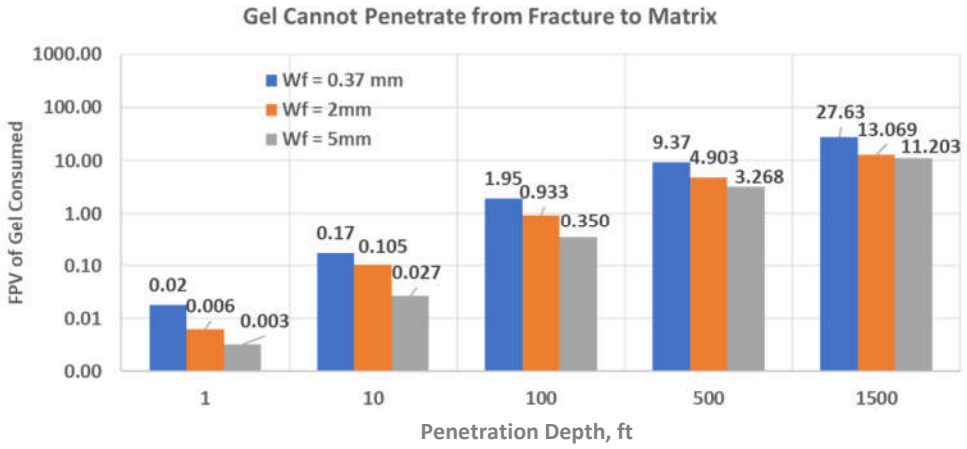

Figure 5.2.17: Optimized gel volume design considering varied penetration and fracture width.

University of Alaska Fairbanks

Main findings of practical significance

- One obvious economic benefit of LSP was reduced polymer consumption to achieve the same target viscosity. The HSP required nearly one third more polymer than the LSP to achieve the same target viscosity in this study. Compared with displacing fluids with relatively high salinity, low-salinity fluids can reduce the effective permeability of aqueous phase (reduced Krw), lower its mobility, and suppress the viscous fingering effect.
- Additional oil was recovered from LSW flooding after extensive HSW flooding (3-9% OOIP). LSW flooding performed in secondary mode could achieve a higher recovery than that in tertiary mode. Also, the occurrence of water breakthrough was delayed in the LSW flooding compared with the HSW flooding. After extensive LSW flooding and HSP flooding, incremental oil recovery (~8% OOIP) was still achieved by LSP flooding with the same viscosity as the HSP. No appreciable incremental oil was recovered by HSP flooding performed after LSP flooding. LSP flooding performed directly after waterflooding can achieve more incremental oil recovery (~10% OOIP).
- Polymer flooding alone was insufficient to achieve a satisfactory oil recovery as the heterogeneity of the reservoirs becomes more pronounced (e.g., Kc/Km>50). Additional conformance treatments are required. The results demonstrate the effectiveness of microgels in improving the conformance under appropriate conditions.
- A critical (minimum) pressure gradient (∇Pcr) was required to drive the microgel particles to propagate the super permeable porous channels. A procedure was developed to estimate the maximum transport (treatment) distance of the gel particles in reservoirs based on the critical pressure gradient. Transport-distance diagrams were developed, which can help engineers select proper gel products to address water channeling problems in reservoirs.
- 260-μm microgel particles tested in this study are effective to address the excessive water production problem and improve the oil recovery when the channel has a much higher permeability (>50 D). The gels are unlikely effective for channels below 30 D due to the penetration/transport difficulties.
- If there were not enough ATBS content in polymer molecules, the injection pressure of gelant will keep increasing immediately after it was prepared and injected which indicated that the micro gel aggregation might be formed after polymer and crosslinker were mixed. This will cause an injection problem as well as formation damage.
- Molecule structure like functional group, molecular weight, and hydrolysis degree will make an effect on gelant injectivity behavior. With more $-COOH^-$ group, longer chain length, and higher hydrolysis degree, the gelant injection pressure will increase faster. The salinity of brine used to prepare the gelant also will have an effect. When SFB (27,500mg/L) was used to prepare the gelant, the injection pressure increased much faster than the gelant using SIB (2,500mg/L) as solvent.
- A simulation model of gel propagation in open fractures has been proposed for gel design in pilot. The model is generated considering the reported mechanisms of gel transport in literatures and the parameters in the model are fitted using lab experimental results. Based on the simulation results in conceptual model, we designed the optimized gel injection for pilot test in field scale. The results show that the consumption of gel volume is sensitive to fracture width and can increase logarithmically with increased penetration depth in fractures.

University of Alaska Fairbanks

Topical publications

1) *Zhao, Y., Wei, M., Leng, L., Bai, B. Propagation of swellable microgels through superpermeable channels: impact of particle–pore matching size relationship, Energy & Fuels 2021, 35, 22, 18533–18542.*
2) *Zhao, Y., Bai, B., Selective penetration behavior of microgels in superpermeable channels and reservoir matrices, JPSE 210 (2022), 109897.*
3) *Zhao, Y, and Bai, B. "Experimental Study of Transport Behavior of Swellable Microgel Particles in Superpermeable Channels for Conformance Control." SPE J. 27 (2022): 790–805.*
4) *Zhao, Y., Leng, J., Lin, B., Wei, M., Bai, B. 2021. Experimental study of microgel conformance control treatment for a polymer flooding reservoir containing super-permeable channels. SPE Journal, 2021, 26 (04): 2305–2317.*
5) *Zhao, Y., Yin, S., Seright, R. S., Ning, S., Zhang, Y., Bai, B. 2021. Enhancing heavy oil recovery efficiency by combining low salinity water and polymer flooding. SPE Journal. 26 (03): 1535–1551.*
6) *Leng, J., Wei, M., & Bai, B. (2022). Impact of Polymer Rheology on Gel Treatment Performance of Horizontal Wells with Severe Channeling. SPE Journal, 27(02), 1017-1035.*
7) *Leng J, Sun X, Wei M, et al. A Novel Numerical Model of Gelant Inaccessible Pore Volume for In Situ Gel Treatment[J]. Gels, 2022, 8(6): 375.*
8) *Leng, J., Wei, M., Bai, B., Seright, R. S., Zhang, Y., Cercone, D., & Ning, S. (2021, August). Impact of Rheology Models on Horizontal Well Polymer Flooding in a Heavy Oil Reservoir on Alaska North Slope: A Simulation Study. OTC-31087-MS.*
9) *Leng J, Wei M, Bai B. Review of transport mechanisms and numerical simulation studies of preformed particle gel for conformance control[J]. Journal of Petroleum Science and Engineering, 2021, 206: 109051.*

5.3 Reservoir Simulation Studies for Coreflooding Experiments and Optimization of Field Pilot Test Injection Strategy

Design of simulation cases

Three different scenarios were designed for simulation studies:

I. Lab-scale simulation case design for core flooding experiment history match based on the core sample conditions, boundary condition, and polymer well geometries. **II**. Full field-scale models case design for actual production history match using multiple relative permeability curves, as well as geomechanical behaviors impacted by polymer flooding, and **III.** Full field-scale 3D models case design for history match using permeability strips classification is used for polymer formula injection strategy optimization and economic evaluation.

I. Major designed cases for lab-scale core flooding behavior simulation include:

- Capillary pressure effect on polymer effectiveness.
- Factors affecting polymer retention.
- Ion exchange effect on the depth of cations advancing to scaling laboratory studies.
- Core flooding history match on injection pressure behavior in two-section sand packs.

- Core flooding phase behavior simulation to investigate the relationship of pore volume injection of brine and residual resistance factor.
- Shear rate versus polymer viscosity behavior.
- Factors affecting polymer retention tail.
- Particle size effect on polymer retention tail using analytical model.
- Wettability effect on polymer retention.
- Examination of pressure barrier issues during polymer flooding.

II. Major designed cases for full field-scale models for actual production history match using multiple relative permeability curves, as well as geomechanical behavior impacted by polymer flooding include:

- Multiple relative permeability curves application.
- Equation of State (EOS) characterization.
- Viscous fingering number consideration.
- Geomechanical behavior during polymer injection.

III. Full field-scale 3D models case design for history match using permeability strips classification used for polymer formula injection strategy optimization and economic evaluation include:

- Introduction of transmissibility strips and transmissibility multipliers for history matching.
- Modification of relative permeability curves and skin factor for history matching.
- Incorporation of the polymer tailing effect.
- Application of a machine assisted history matching.
- Stage-wise history matching for more reasonable predictions.

Summary of key results

Wettability effect on polymer retention investigation

Wettability effects on polymer retention were investigated from three scenarios: (1) 1D lab-scale homogeneous Cartesian simulation model, (2) 2D semi-field corner point model with heterogeneity from aerial view, and (3) 3D full field-scale simulation model with heterogeneity in both areal and vertical directions in orthogonal corner point system. In this report, a lab-scale homogenous model that focuses on NB sand with grid cells of 61 × 1× 1 in *x*, *y*, and *z* directions will be discussed in this section. In order to observe the wettability alteration as the fluid saturation change or production change, the Amott-Harvey method was adopted for all three scenarios. As laboratory studies for wettability survey do, several steps must be performed with spontaneous imbibition or forced imbibition process, and drainage process, respectively. In the Amott-Harvey method, wettability status is defined as oil-wet to strong oil-wet from the wettability index range from "- 0.3 ~ -1", and water-wet to strong water-wet from the range from "0.3 ~ 1". In between the value from "-0.3 ~ 0.3", it is defined as intermediate wetting state or neutral state.

Based on Morrow's model and a scaling group proposed by Mattax and Kyte (1962), as well as Ma *et al*. (1997), we developed an analytical method for drainage time scaling for this study. Wettability

changes were then estimated using the methods proposed by Dake (1977) and Amott (1959). **Figure 5.3.1** and **5.3.2** show the wettability change effect on polymer retention on 2D and 3D maps, as well as the wettability effects on oil recovery. Theoretically, oil recovery is less when wettability status is strongly water-wet or oil-wet. From **Figure 5.3.2**, for the 2D, 1-Layer heterogeneity (in the areal direction) model, oil recovery basically stabilized over a long time because of the strong oil-wet wettability status. However, for the 3D heterogeneity model, oil recovery exhibited an increasing trend as wettability index changed from strong oil-wet to intermediate-wet.

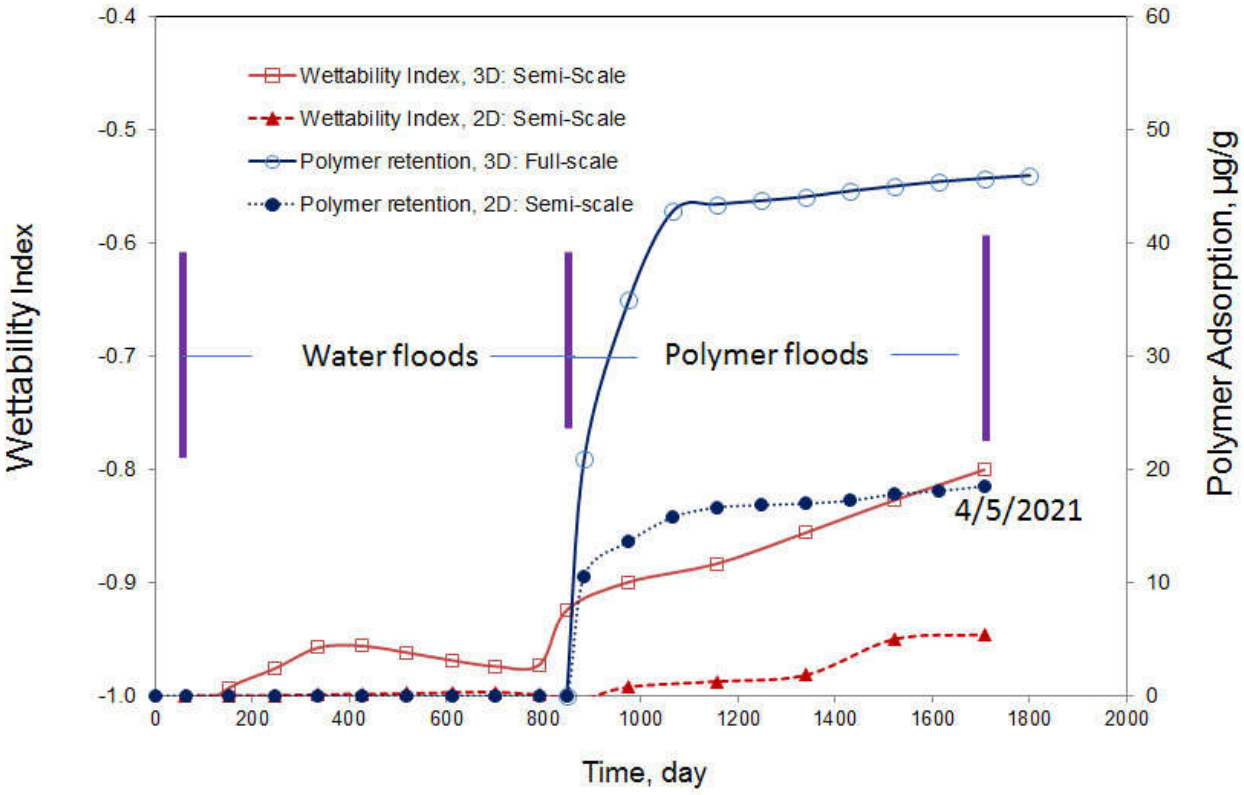

Figure 5.3.1: Wettability vs polymer retention comparison between heterogeneity in areal plane and in vertical geometry.

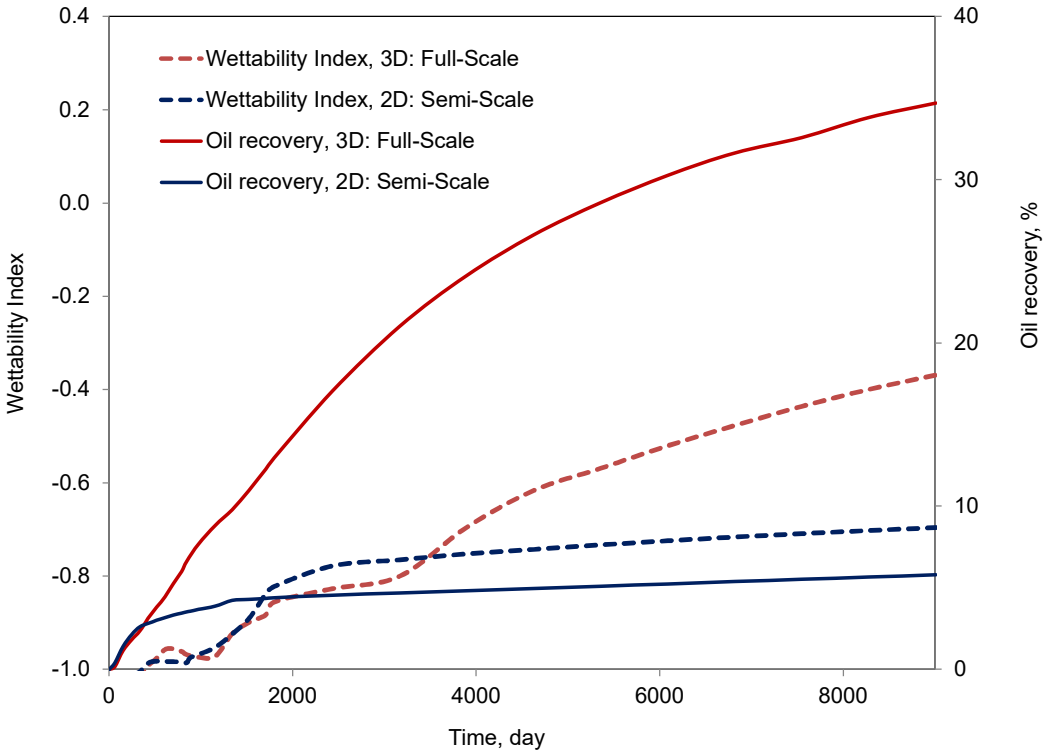

Figure 5.3.2: Wettability vs. oil recovery prediction for 1.4 PV polymer injection.

Examination of pressure barrier issues during polymer flooding EOR

To examine the polymer front between an injector and a producer, 3D models were established based on the description for each field. For vertical wells, the length of the polymer bank was presented in the *x*-direction in the model, and for horizontal wells, it was presented in the *y*-direction, as illustrated by **Figure 5.3.3**. Simulations were performed to estimate the pressure gradient in the oil bank during polymer injection under three viscous oil conditions. Simulations were performed using CMG IMEX and properties are listed in **Table 5.3.1**. In this report, we are focusing on the analysis of the Milne Point case.

Table 5.3.1: General property of simulation area for the three heavy oil fields.

Reservoir property	Oil Fields		
	Milne Point	Tambaredjo	Pelican Lake
Well geometry	Horizontal	Vertical	Horizontal
Well spacing, ft	1179	443	574
Oil viscosity, cp	300	600	1650
Injection layers	8	5	2
Ave permeability, md	1032	4066	3030
Ave. thickness, ft	1.70	24.06	4.4
Max. permeability contrast	1.86	22.32	1.22

Ave. porosity	0.35	0.19	0.30
Polymer viscosity, cP	45	45 ~ 85	22
S_{wi}	0.220	0.120	0.224
k_{rw} at S_{or}	0.18	0.15	0.216
Bubble point pressure, psi	1382	290	305
Reservoir pressure, psi	1600	485	420

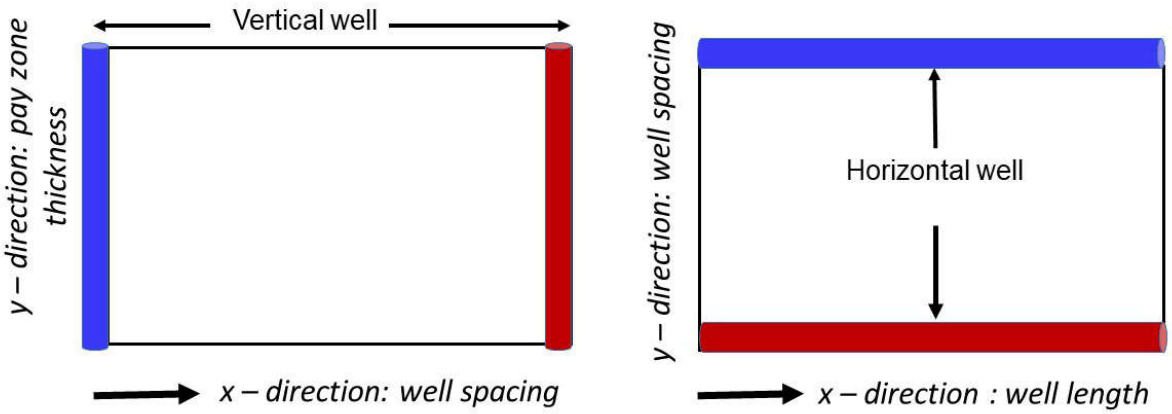

Figure 5.3.3: Illustration of polymer advancing direction in simulation models.

In the current work, we focused on the pressure gradients anticipated within the oil bank during the polymer flood. In the model which generated the green curve in **Figure 5.3.4**, eight vertical layers were used in the simulation model to represent the NB sand in the Milne Point field. The green curve is the predicted pressure gradient within the oil bank that remains constant for most of the polymer flood. The other curves in **Figure 5.3.4** show predictions, assuming the oil in the reservoir was more viscous than 300-cp. The black curve in **Figure 5.3.4** indicated that the pressure gradients within the oil bank become greater as the polymer flood progresses and as the reservoir oil becomes more viscous (because of the increased polymer/oil mobility ratio as the oil viscosity is raised while keeping the polymer viscosity fixed at 45 cp) at a certain polymer injection volume (0.67PV). We suspect that the increase in pressure gradient will not actually materialize within the oil bank because of viscous fingering and vertical equilibrium effects.

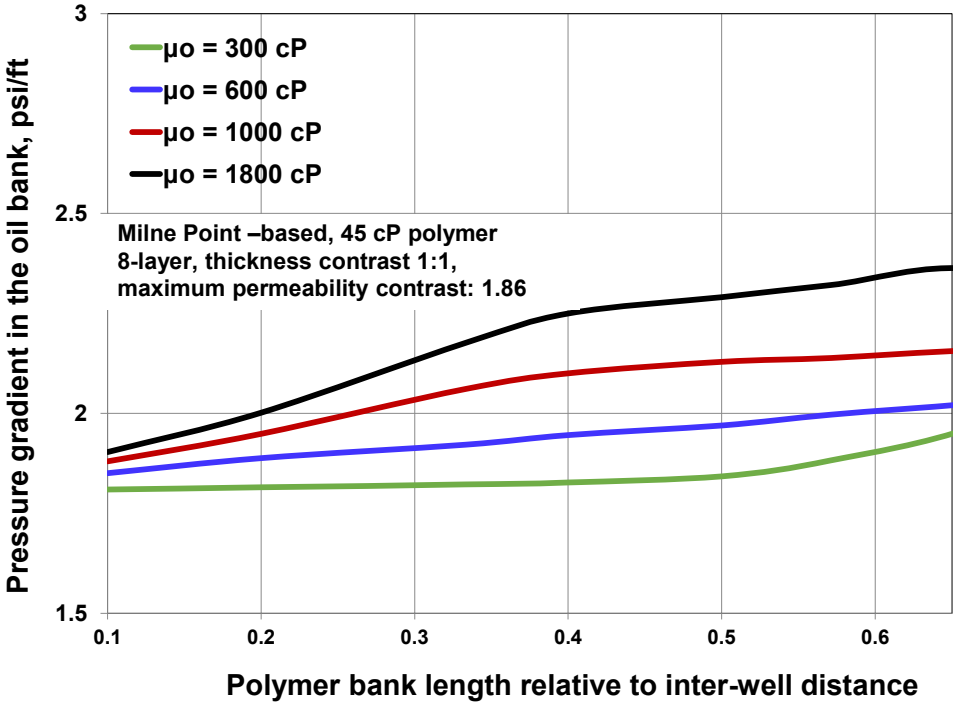

Figure 5.3.4: Simulation predicted pressure gradients in the oil bank for Milne Point case.

Geomechanic Behaviors during Polymer Flooding

In order to examine the effects of geomechanics on polymer flooding, four rock parameters were incorporated into the full-field scale model: Poisson's ratio, Young's modulus, Modulus of rigidity, and Bulk Modulus. All four parameters were discussed by Rutqvist (Rutqvist, et al. 2009) and Masui (Masui, et al. 2005) under unconsolidated sand rock and soil conditions. In the simulation, three functions were studied to observe how deformation strain or mean stress to the rock formation changed.

Stress Development along ICD in Lateral Direction. Effective stress (basically means total stress – pore water pressure), tensile stress, and shear stress, as well as porosity behaviors along the length of two horizontal injection wells during polymer flooding when porosity acts as a function of pressure, temperature, and total mean stress formula. The work will be valuable for later studies in injectivity and productivity prediction from a geomechanics view.

Our findings in the effective stress which developed along the horizontal wells are:

(1) Effective stress around the two injection wells decreased about 50% on average in tensile direction after 1.5 years polymer injection.
(2) In both injection-well discharge areas, the least stress observed was near the middle well bore locations along the horizontal directions.
(3) For the two injection wells, the geomechanically corrected porosity shows slight changes due to injection rate and injection pressure variation.

(4) The increasing and decreasing degrees of shear stress observed in the two injection wells indicate the possibilities of vertical fractures opening or closing.

Figure 5.3.5 and **5.3.6** describe the effective and shear stress development under the porosity corrected by geomechanical effect during the first 1.5 years polymer injection. In the figures, the vertical bars in the maps indicate the ICD (injection control device) numbers. The curves represent the different time stages.

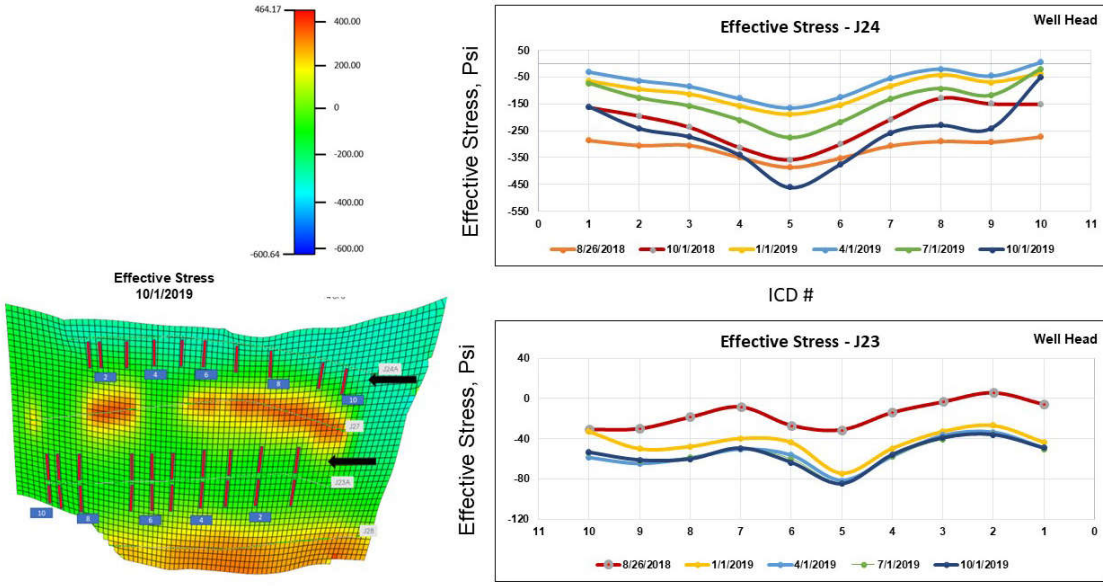

Figure 5.3.5: Effective stress development along two horizontal injectors during polymer flooding.

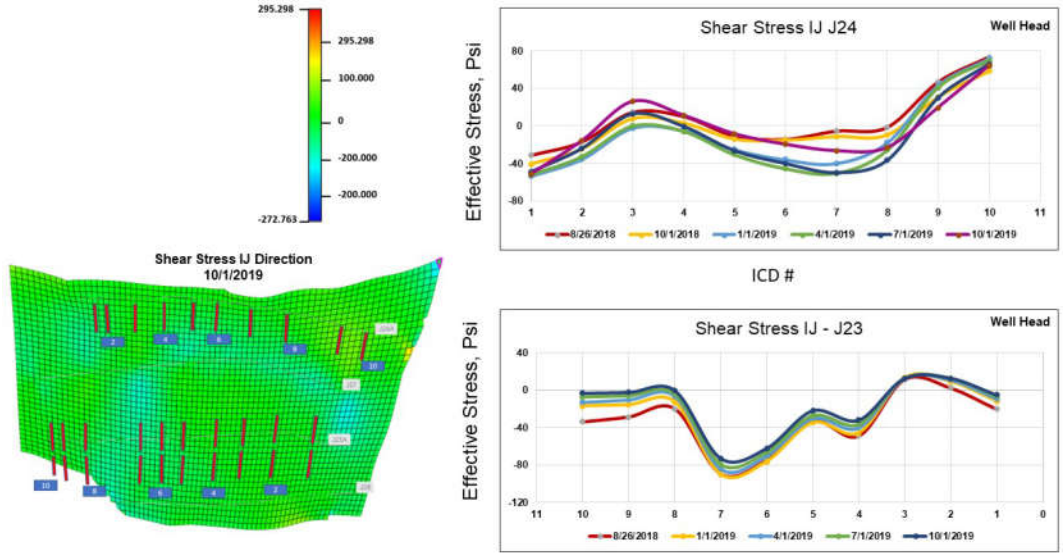

Figure 5.3.6: Shear stress development along two horizontal injection wells during polymer flooding.

Maximum and Minimum Stress Development along TVD Direction. The effective stress and shear stress development in two injection wells were studied. In most subsurface conditions, the vertical stress is to be considered as maximum principal stress, and the minimum or intermediate principal stress is assumed to be horizontal. Profile analysis on the maximum and minimum stress will be valuable for later studies in injectivity and productivity prediction from a geomechanics view. **Figure 5.3.7** illustrates the changes of minimum stress, maximum stress, as well as reservoir pressure of four polymer pilot wells along TVD direction, which is represented by blue, orange, and green lines. The negative values in the two injection wells stand for stress in tensile expansion, and the positive values are in compressive development. **Figure 5.3.8** shows the map of maximum stress development in the perforated layers along TVD direction of Well #J27.

Based on geomechanical simulation, we observed:

(1) For the two production wells, the minimum stress change in horizontal along TVD direction was less than 100 psi, and the maximum stress changes ranged from 300 to 500 psi from well to well. Reservoir pressure changes ranged from 1200 to 1000 psi from well to well. The result indicates that productivity has not been affected by stress change significantly.

(2) For the two injection wells, both minimum and maximum principal stress were developed in tensile direction in the range of 300 to 500 psi from Layer 1 to Layer 8. The reservoir pressure is basically reflecting the bottom-hole-pressure change to date. Since the stress developed in tensile direction, the formation pore volume was assumed to increase due to regional porosity corrected by geomechanical property during injection, which indicates increased injectivity occurred during polymer flooding.

(3) As illustrated in **Figure 5.3.8**, for Well #J27, there is less than 200 psi difference during polymer flooding from well head to well toe, and no significant stress development among layer to layer due to the reservoir homogeneity in vertical.

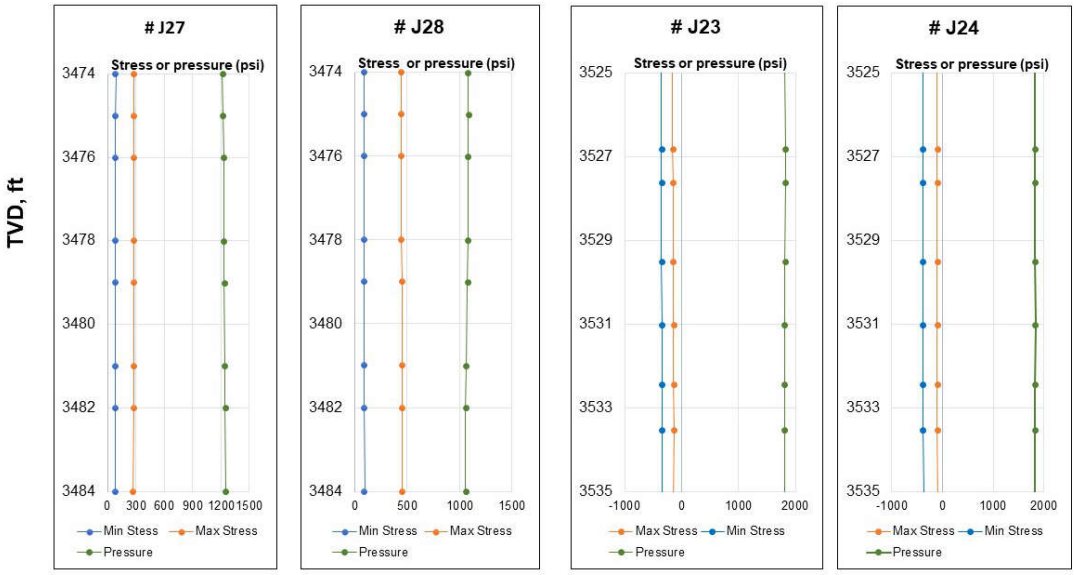

Figure 5.3.7: Principal stress development along TVD direction during polymer flooding.

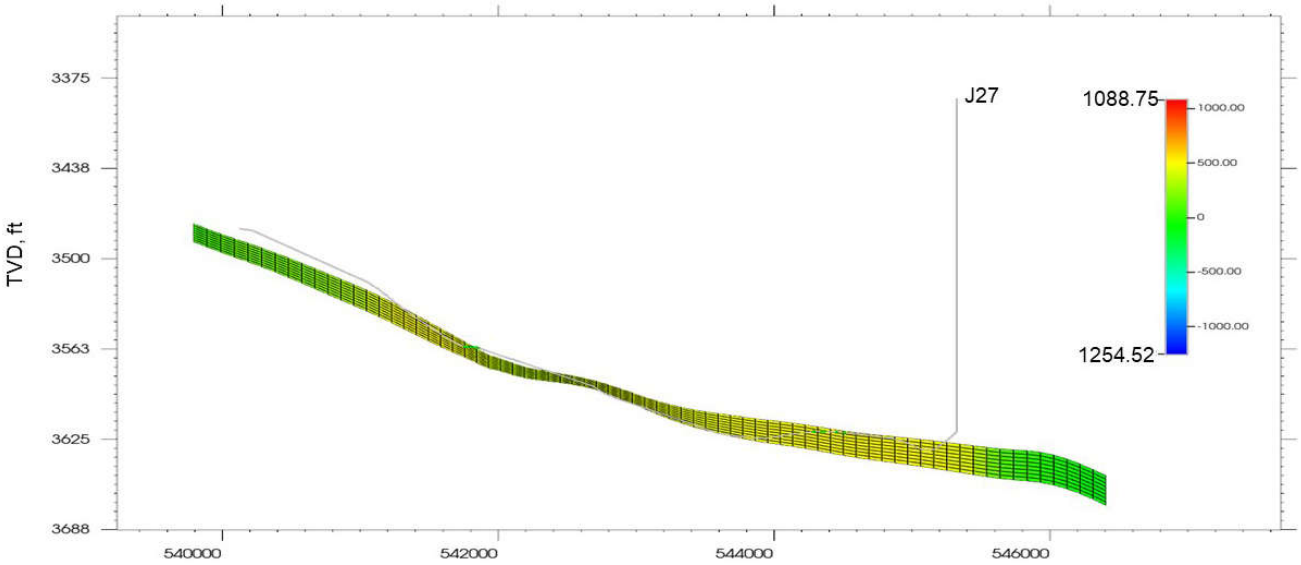

Figure 5.3.8: Principal stress development along TVD of Well #J27 direction during polymer flooding.

III. Full field-scale 3D models case design for history match using permeability strips classification is used for polymer formula injection strategy optimization and economic evaluation.

Base Model

The base reservoir simulation model was run in CMG IMEX™ prior to history matching work. Simulated water cut results for both producing wells for all models are shown in **Figure 5.3.9**. The base model results are indicated with the blue line, while the black circles represent the actual production history. As can be seen, the base model fails to replicate the early water breakthrough and high water cut observed in the actual production data. Furthermore, it does not capture the magnitude of water cut reduction observed during the polymer flooding period, nor does it capture the increase in water cut in J-28 in 2021. This demonstrates that the model must be calibrated to the production data before it is useful for forecasting.

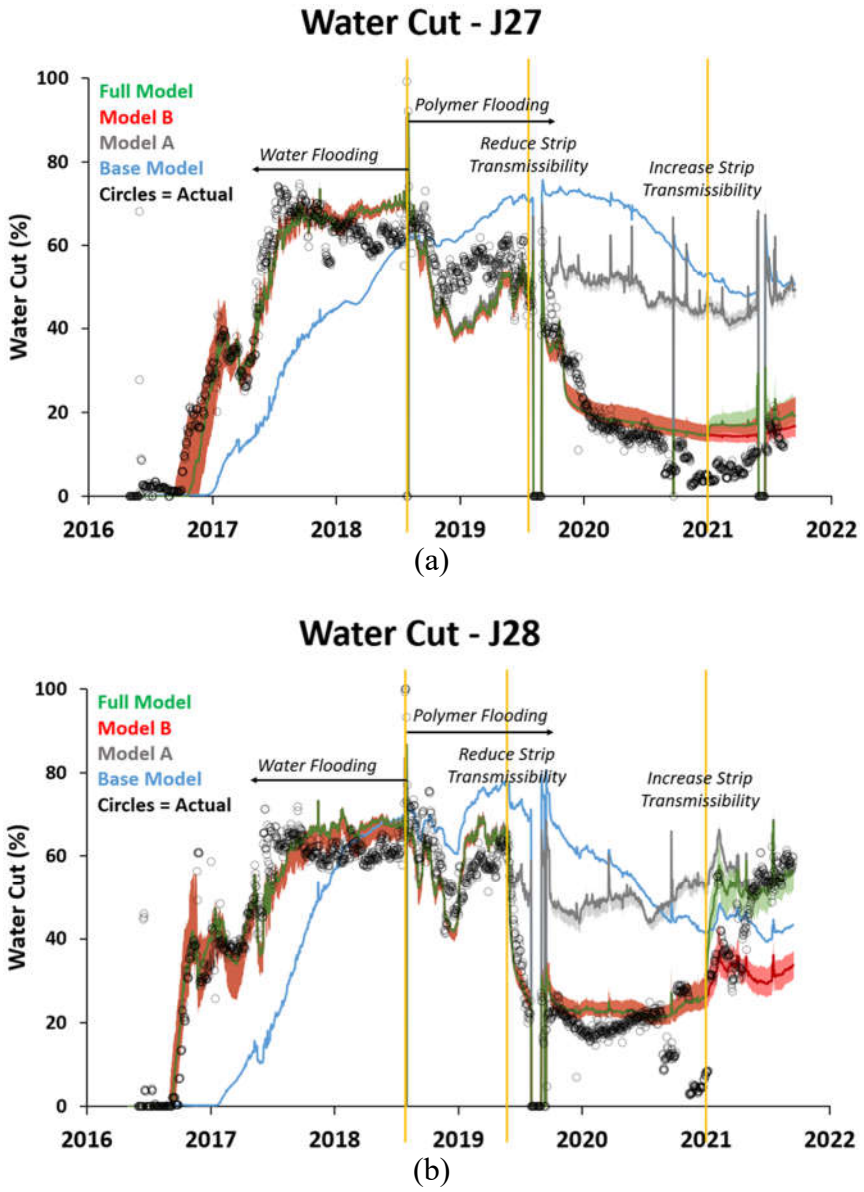

Figure 5.3.9: Water cut simulation results for (a) J-27 and (b) J-28.

Step-wise history matching models and predictions

In order to match the early water breakthrough and high water cut observed during the waterflood period, transmissibility contrasts were introduced to the reservoir model in the form of the strip and block arrangement as shown in **Figure 5.3.10** and **5.3.11**. Then, transmissibility multiplier values, along with other history matching parameter values are tuned to conduct history matching.

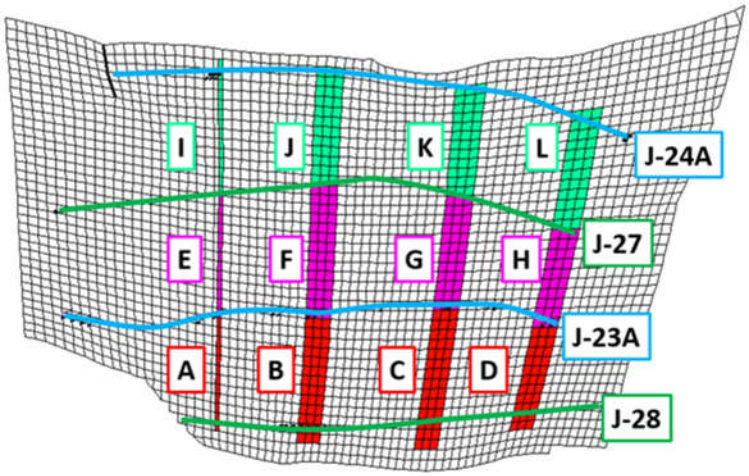

Figure 5.3.10: Location of high transmissibility strips (colored) in the model.

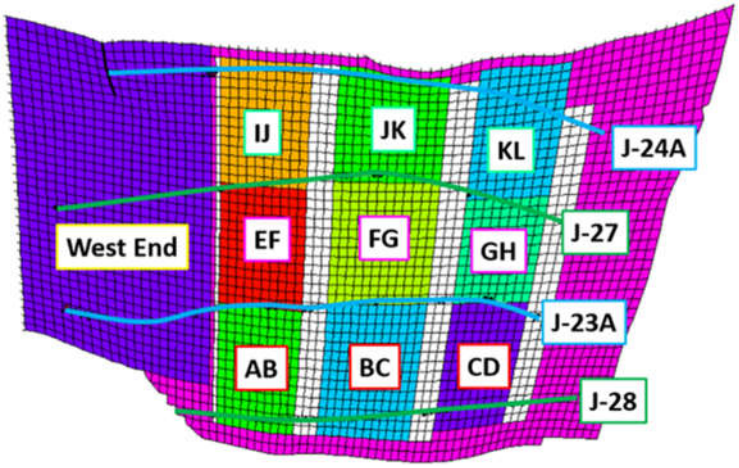

Figure 5.3.11: Location of inter-strip-blocks (colored).

This first history match attempt, with transmissibility contrasts introduced to match the early production history, is referred to as "Model A." The resulting water cut history match for Model A is indicated in gray in **Figure 5.3.9**, with the best matched model results indicated with the dark gray line and the range of results from the top 24 models represented with the light gray shaded area. The introduction of transmissibility contrasts successfully recreated the early water breakthrough and high water cut observed during the waterflood period. An adequate history match is maintained through the first eight months of the polymer flood period. However, the model fails to replicate the significant reduction in water cut observed after the polymer flood has matured after eight months. Thus, Model A successfully history matches the data through mid-2019 but is inadequate afterwards.

Model A is unable to replicate the dramatic 50% decrease in water cut observed in mid-2019. To reproduce this extreme behavior, the three-cell width strips (i.e., B, C, D, F, G, H, J, K, L in **Figure 5.3.10**) were removed. Furthermore, the half-cell width strip (i.e., A, E, and I in **Figure 5.3.10**) transmissibility was reduced. Finally, an additional accumulative "blanket" transmissibility

multiplier was applied between each well pair. This is justified by the necessity to maintain a reasonable BHP match, thus continuing to honor the reservoir injectivity and deliverability. This new model is referred to as "Model B". The resulting water cut history match for Model B is indicated in red in **Figure 5.3.9**, with the best matched model results indicated with the dark red line and the range of results from the top 24 models represented with the light red shaded area. The first gold line indicates the timing of the reduction in strip transmissibility. As can be seen, the reduction in the transmissibility contrast successfully recreated the low water cut observed after the polymer flood benefits became apparent in mid-2019. The water cut history match is adequate for J-27 for its entire history, but is inadequate for J-28 in 2021. Here, the actual water cut increased rapidly to nearly 60% by August 2021, and Model B is unable to replicate this surge.

In order to match the high water cut encountered in J-28 in mid-2021, one-cell width high transmissibility strips were returned in between J-23A and J-28. Furthermore, the half-cell width strip transmissibility was increased to match the higher produced polymer concentration in both producing wells. Finally, an additional accumulative "blanket" transmissibility multiplier was applied between J-23A and J-28 to maintain a reasonable BHP match and thus continue to honor the actual reservoir deliverability and injectivity. This new model, matched through all current production data, is referred to as the "Full Model". The resulting water cut history match is shown green in **Figure 5.3.9**. The dark green line indicates the results from the best matched model, while the light green shading displays the range of values achieved by the top 24 models. The additional gold line indicates the timing of the increase in strip transmissibility in 2021. Note that the one-strip width blocks needed to be opened in January 2021 to ensure a reasonable match of the produced polymer concentration, even though this results in an earlier increase in water cut in J-28 than was observed in the actual data.

The oil recovery forecasts produced by Model A, Model B, the Full Model, and waterflooding alone are compared in **Figure 5.3.12**. As can be seen, Model A produces the most pessimistic results, Model B is the most optimistic, and the Full Model (including the anticipated water surge in J-27 at the start of 2022) predicts an intermediate oil recovery. Importantly, all three polymer flooding models predict significantly higher oil production under polymer flooding compared to waterflooding alone.

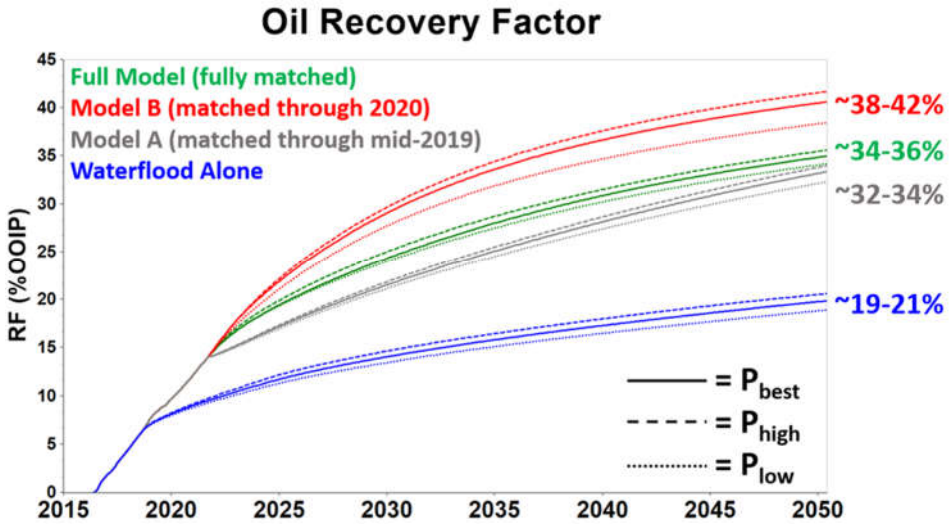

Figure 5.3.12: Predicted oil recovery for each forecasted simulation case. The best matched model forecast for each case is indicated with a solid line, the most optimistic forecast for each case is indicated with a dashed line, and the most pessimistic forecast for each case is indicated with a dotted line.

Effect of Retention Tailing

The producing water cut and polymer concentration history match using the Full Model with and without the retention tailing effect are shown in **Figure 5.3.13** and **5.3.14,** respectively. The use of the linear model in place of the tailing model increases the water cut and decreases the produced polymer concentration during 2020 and 2021, reducing the quality of the history match. This indicates that the inclusion of the retention tailing effect is significant to the success of this history matching process.

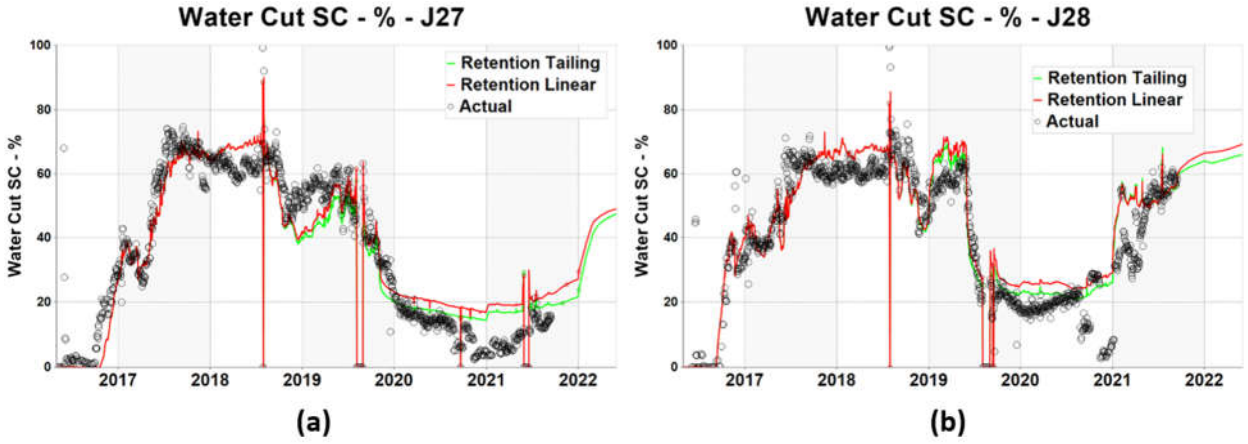

Figure 5.3.13: Producing water cut history match for (a) J-27 and (b) J-28, with and without the retention tailing effect.

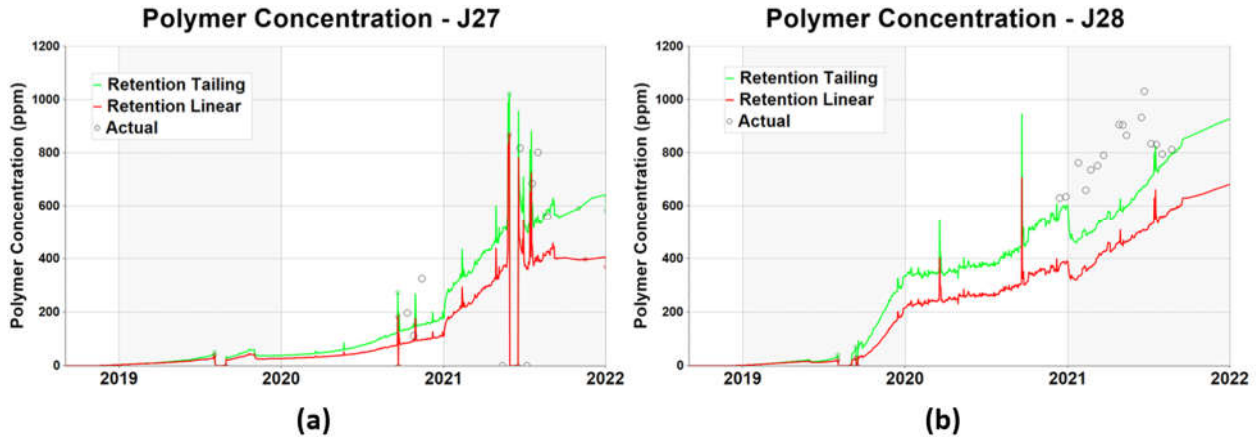

Figure 5.3.14: Produced polymer concentration history match for (a) J-27 and (b) J-28, with and without the retention tailing effect.

The incorporation of retention tailing results in a higher anticipated oil recovery than the simpler but less accurate linear model. By 2050, the linear model predicts an oil recovery of 33.2%, notably lower than the 35.0% predicted by the forecast with the retention tailing effect.

Main findings of practical significance

- Capillary pressure has no significant impact on polymer effectiveness for the target reservoir using the polymer flooding EOR method.
- Polymer retention is affected slightly by the composition of bivalent cations or monovalent cations in the injection water. The residual resistance factor only affects polymer adsorption during polymer propagation. Large heterogeneity in areal direction led to less apparent polymer adsorption – suggesting for the heterogeneous cases that high polymer viscosities might be needed to overcome the heterogeneity. For a vertical heterogeneity oil zone, permeability is a dominant factor for polymer absorption but not the variance of the polymer retention in different layers – suggesting multiple injection formulations designing for the sweep efficiency improvement. Polymer retention is only affected at the initial stage of polymer propagation with the well geometries.
- Formation salinity was reduced by a factor of about 10 after low salinity polymer solution injection. The highest ion exchange by sodium ion occurred around 0.20 PV with high illite content (25%); and the salinity decrease was more apparently compared with a low illite content. Calcium was more active with illite. A greater amount of calcium was exchanged at higher illite content. With respect to magnesium exchange, no obvious difference was noted if illite content was low and retention was low compared to when no clay exists. Magnesium exchange was more active when illite content was high or the polymer retention was high.
- For the 1-PV injection in a 2-section core, the greater rate of pressure increase indicated fast polymer advance along the core with less polymer adsorption in the first section. The lower rate of pressure increases in the section indicated slower polymer propagation. History matches are in agreement with experimental observations.

- For 1750 ppm 3630S polymer, viscosity at 1 s^{-1} is about twice that at 7.3 s^{-1} as experimental results. With a 2183 mD native NB#3 sand, Darcy's velocity is about 1/20 (ft/day) of shear rate in a viscometer 1 s^{-1} shows similar results compared using shear rate effect.
- The polymer retention tail lasted longer during most of produced polymer relative to injected polymer with high polymer concentration, indicate the high polymer retention occurred during this period. Tail lasting longer during 90-100% of produced polymer relative to injected polymer with less permeability, indicate the high polymer retention occurred during this period. With slow injection rate, most polymer retention occurred during the middle of injection with longer tail lasted. With high polymer concentration, or low permeability, high polymer retention tails last longer. However, the polymer retention values could be ignored during 2 PV injection for the reality (0 ~ 60 μg/g). At various injection rates, high polymer retentions are expected with high volume polymer injection (> 10 PV). Within the periods of 1 to 2 PV of polymer injection, all polymer retentions are low based on history matches on experimental results. High injection rate led to fast polymer retention building up accompanying the longer tailing length. However, the tailing lengths have no significant difference with medium or ultra-low injection rates.
- Well-graded sand with a certain proportion of large particle size exhibits a fast polymer propagation with a short tail adsorption. Poorly graded sand with feldspar mineral presented (black) exhibits a slow polymer propagation with a longer tail adsorption due to the possibility of dissolved clay produced by water absorbing. Since adsorption is a surface phenomenon, adsorption increases with the increase in the surface area of the adsorbent. In other words, more finely divided or rougher the surface of adsorbent, the greater will be the surface area and hence the greater will be the adsorption.
- Oil-wet wettability status observed in both areal heterogeneous plane and 3D heterogeneous geometries from water flooding stage and polymer flooding stage. Oil-wet degree exhibits stronger in the areal heterogeneous direction. Wettability status changes to the weakly oil-wet direction with more polymer injection. Polymer retention exhibited lower values in the areal heterogeneous direction compared to the 3D geometry. In the first 22% PV injection, a low polymer retention (< 40 μg/g) observed for the actual field model. Polymer retention might suggest wettability changing from oil-wet to weak oil-wet direction still with a low retention when polymer injection reaches 1.4 PV. The change tendency of polymer retention is consistent with the lab result for NB sand studies. For 2-D, 1-Layer heterogeneity in areal direction model, oil recovery basically stabilized for a long time because of the oil-wet wettability status. However, for the 3-D heterogeneity model, oil recovery exhibits an increasing trend as wettability index changed from strong oil-wet to intermediate-wet direction.
- Given the Milne Point heterogeneity, both new history match approaches (multiple relative permeability curves with low K_{rw} endpoints and high permeability channels) have been employed and have resulted in reasonably robust history matching as far as the low water cut is concerned.
- EOS flash calculations with multiple hydrocarbon compositions modeling are a useful tool for reaching a satisfactory numerical simulation result in GEM.
- Viscous fingering number incorporation provided a basic match of the production data, but not a very good agreement in the later stage of water cuts for this specific numerical simulation model.
- From the view of geomechanics, after polymer injection, rock exhibits mostly brittle behavior (elastic) until rupture. Using current geomechanical parameters in the model, a notable water cut change was predicted due to pore volume (porosity) change. These changes were caused by strain

deformation or stress change. Effective stress around the two injection wells decreased about 50% in average in tensile direction after 1.5 years polymer injection. In both injection-well discharge areas, the least stress observed was near the middle well bore locations along the horizontal directions. For the two injection wells, the geomechanically corrected porosity show slight changes due to injection rate and injection pressure variation. The increasing and decreasing degrees of shear stress observed in the two injection wells indicate the possibilities of vertical fractures opening or closing. Porosity distribution (variation and average from Layer 1 to 8) does not affect tensile stress (part of effective stress) very much. However, effective stresses are less when the porosity distribution was set to an average value compared to the porosity distribution with variable values; Shear stress trends were similar between two sets of porosity variations. For the two production wells, the minimum stress change in horizontal along TVD direction were less than 100 psi, and the maximum stress changes about 200 psi from well to well. Reservoir pressure changes were in a similar range from well to well. The result indicates that productivity has not been affected by stress change significantly.

- Transmissibility contrasts had to be introduced to the model to simulate early water breakthrough during waterflooding of heavy oil, which forces the viscous fingering behavior believed to motivate the early water breakthrough. These transmissibility contrasts had to be reduced to simulate the restoration of injection conformance from tertiary polymer flooding. Transmissibility contrasts were reintroduced to replicate a water surge event observed during polymer flooding in one of the production wells, which may represent fracture overextension resulting from polymer injection in the unconsolidated formation.
- Machine-assisted history matching procedures allowed many parameters to be varied independently, producing a more reasonable calibrated model than manual procedures. This is gauged by the reduced frequency of transmissibility changes in time and the simultaneous matching of producing water cut, produced polymer concentration, and BHP.
- The proper definition of retention in the simulation model, incorporating a retention tailing effect, was useful to match the producing water cut and produced polymer concentration simultaneously.
- All calibrated simulation models predict significantly higher oil recovery from polymer flooding compared to waterflooding alone.
- Oil recovery of polymer flooding is sensitive to the occurrence and timing of a similar water cut surge event in the other producing well (i.e., J-27). If the event can be delayed or avoided, oil recovery will increase.
- A simulation model calibrated for waterflooding may not accurately capture the full benefit of an EOR strategy such as polymer flooding.
- The predictive capacity of a simulation model is limited by the flow behavior captured in the production history. Thus, a previously calibrated simulation model may no longer be valid for predictions if events occur to change this flow behavior.

Topical publications

1) *Wang Dongmei, Shane Namie, Randall Seright, "Pressure Modification or Barrier Issues during Polymer Flooding Enhanced Oil Recovery", Geofluids, vol. 2022, Article ID 6740531, 15 pages, 2022.*
2) *Polymer Flood Field Test Of Heavy Oil On Alaska North Slope Via Machine Assisted Reservoir*

Simulation, SPE-209443-MS, SPE Virtual Improved Oil Recovery Conference, 25–29 April 2022.

3) *Namie, S., Wang, D., Yin, Z., Radu, G., Samson, N., Dandekar, A., Cercone, D., Ciferno, J., & Xindan, W. (2021). Challenge Solutions for a Significant Water Cut Reduction History Match on Heavy Oil Polymer EOR. 82nd EAGE Annual Conference & Exhibition, 1–5.*
4) *Wang, X., Keith, C.D., Zhang, Y., Dandekar, A., Ning, S., Wang, D., Edwards, R., Barnes, J., Cercone, D.P. and Ciferno, J.P., History Matching and Performance Prediction of a Polymer Flood Pilot in Heavy Oil Reservoir on Alaska North Slope, SPE-206247-MS, SPE Annual Technical Conference and Exhibition, 21 - 23 September 2021 in Dubai, U.A.E.*

5.4 Implementation of Polymer Flood Field Pilot in Milne Point

Design of the pilot

Test site

The pilot area is selected at J-pad of the Milne Point field (**Figure 5.4.1**) which is located approximately 30 miles northwest of Prudhoe Bay Field and 15 miles Northeast of Kuparuk field on the North Slope of Alaska. Milne Point field was discovered in 1969 and production began in November 1985. Operated and owned by Conoco, production from the field was suspended between January 1987 and April 1989 due to low oil prices. The average production rate from April 1989 through December 1993 was 18.2 MBD (thousand barrels per day). In January 1994, BP acquired 91.2% interest and became field operator and then acquired the remaining interest in 2000. As a result of additional drilling and facilities construction, production peaked at 59.1 MBD in July 1998. In November 2014, Hilcorp acquired 50% interest in Milne Point field and assumed operatorship, then Hilcorp became 100% owner in July 2020. Oil production rate ranged 18 to 22 MBD from 2014 to 2018 but recently increased to over 37 MBD due to new developments using extended horizontal wells (up to 12,000 ft) in the Schrader Bluff heavy oil reservoir at the new Moose Pad as well as other existing drilling pads in the field.

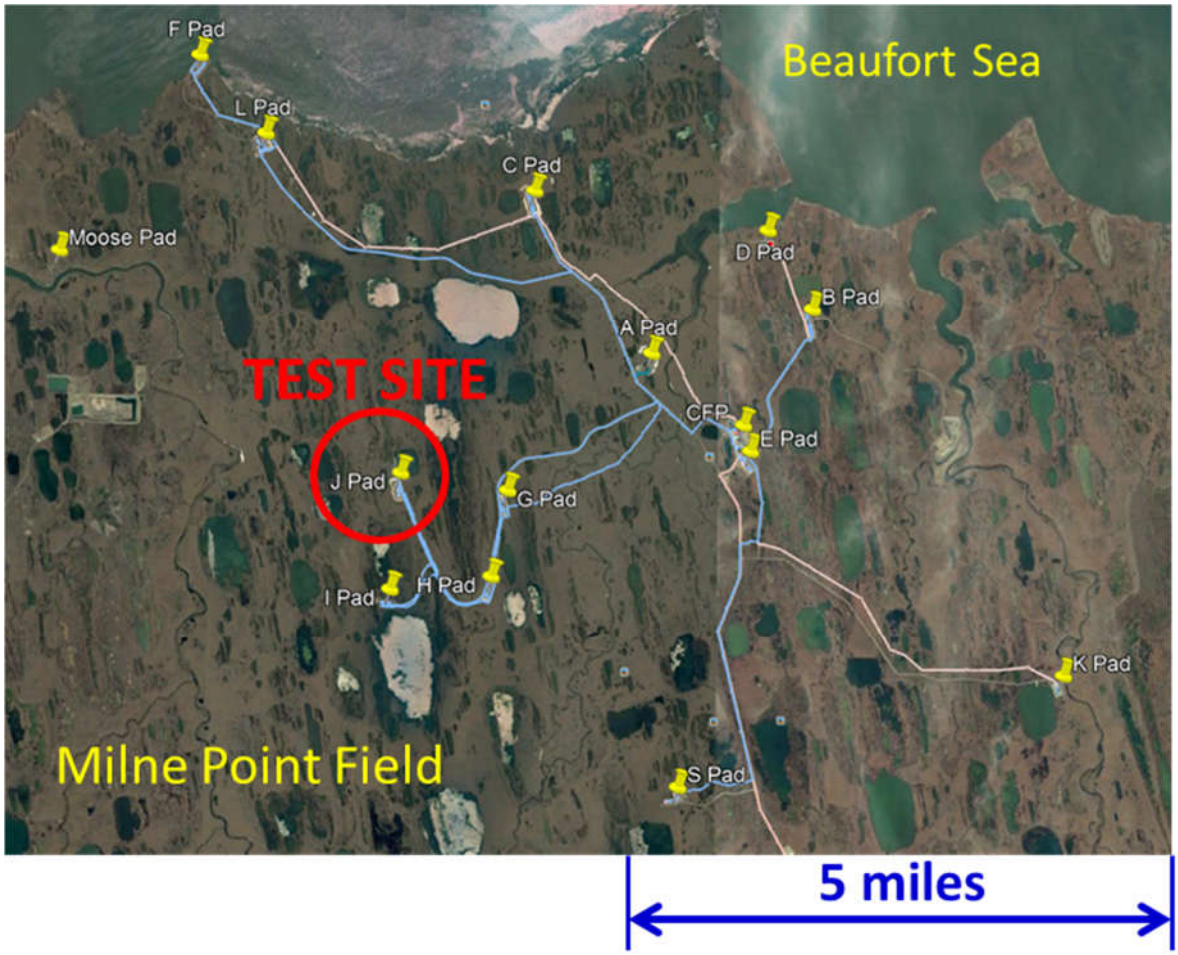

Figure 5.4.1: Location of the pilot area at Milne Point J-pad.

The Milne Point field consists of four separate oil-bearing formations, listed from shallowest to deepest: Ugnu, Schrader Bluff, Kuparuk, and Sag River. The Ugnu formation is a shallow and unconsolidated sandstone reservoir containing heavy oil which is yet to be developed. The sandstones of the Kuparuk formation contain light oil and have historically been the main producing reservoir at Milne Point. The Sag River is the deepest hydrocarbon-productive formation in Milne Point with very light oil.

The Schrader Bluff formation was deposited in the Late Cretaceous period and was composed of several marine shore face and shelf deposits (McGuire et. al 2005). **Figure 5.4.2** is a typical log of the Schrader Bluff formation at Milne Point field which is divided into the O-sands (OA and OB) and the N-sands (NA through NF). The project wells are completed in the NB sand which is a thin and unconsolidated shallow marine sandstone with a thickness of 10-18 feet in the J-Pad area of Milne Point. Porosity is approximately 32% and permeability ranges from 500 md to 5000 md. Oil gravity is about 15 degrees API in the project area with a viscosity of ~300 cP at the reservoir conditions.

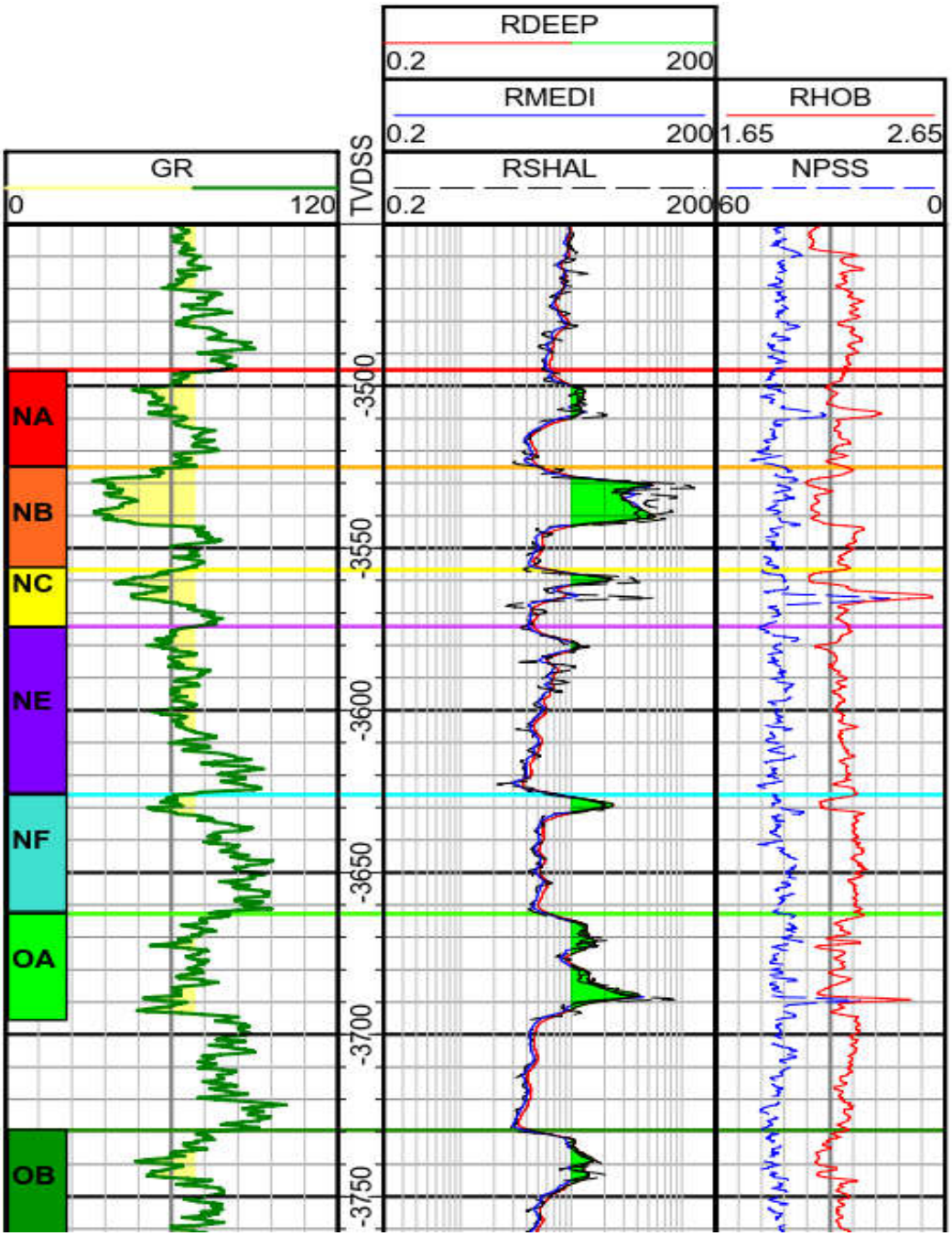

Figure 5.4.2: Type log of the Schrader Bluff formation at Milne Point.

Figure 5.4.3 is a subsurface map showing the horizontal well patterns involved in the project which consists of two injectors (J-23A and J-24A) and two producers (J-27 and J-28) drilled into the Schrader Bluff NB-sand. The lengths of the horizontal wellbores are from 4200 to 5500 feet and the inter-well distance is approximately 1100 feet.

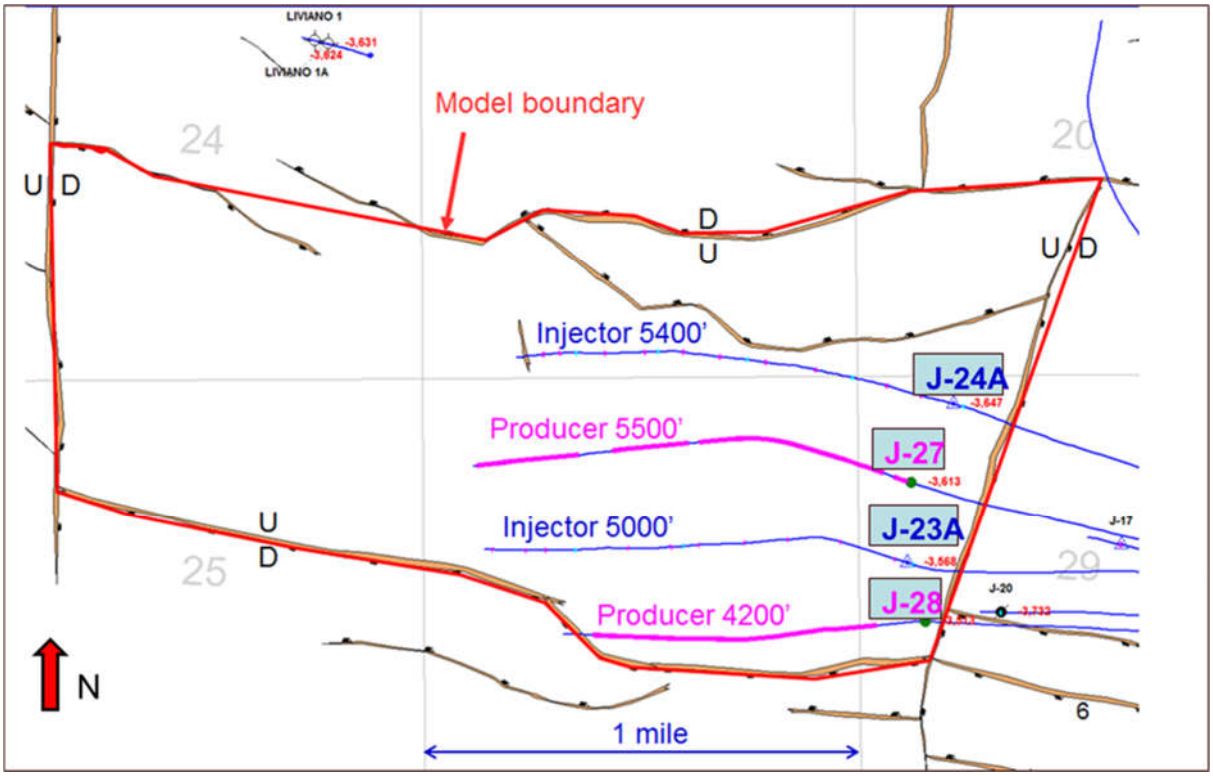

Figure 5.4.3: Project well patterns.

Figure 5.4.4 is a wellbore diagram for injector J-24A which is similar to that of J-23A. The injectors are completed with 4-½" liners equipped with injection control devices (ICD) and swell packers to divide the wellbores into segments. There are 10 ICD's installed in J-24A, each contains ten ⅛" nozzles which are used to regulate water flow along the wellbore. In case there is a thief zone that creates fast connection between the injector and producers, the ICD's in that section of the wellbore will act like chokes to limit water flow into the thief zone.

Water injection started in June 2016 at J-23A and February 2017 at J-24A prior to polymer injection. Approximately 2 million barrels of water was injected into the 2 pilot patterns before polymer startup, which is approximately 12 percent of the total pore volume of the 2 patterns.

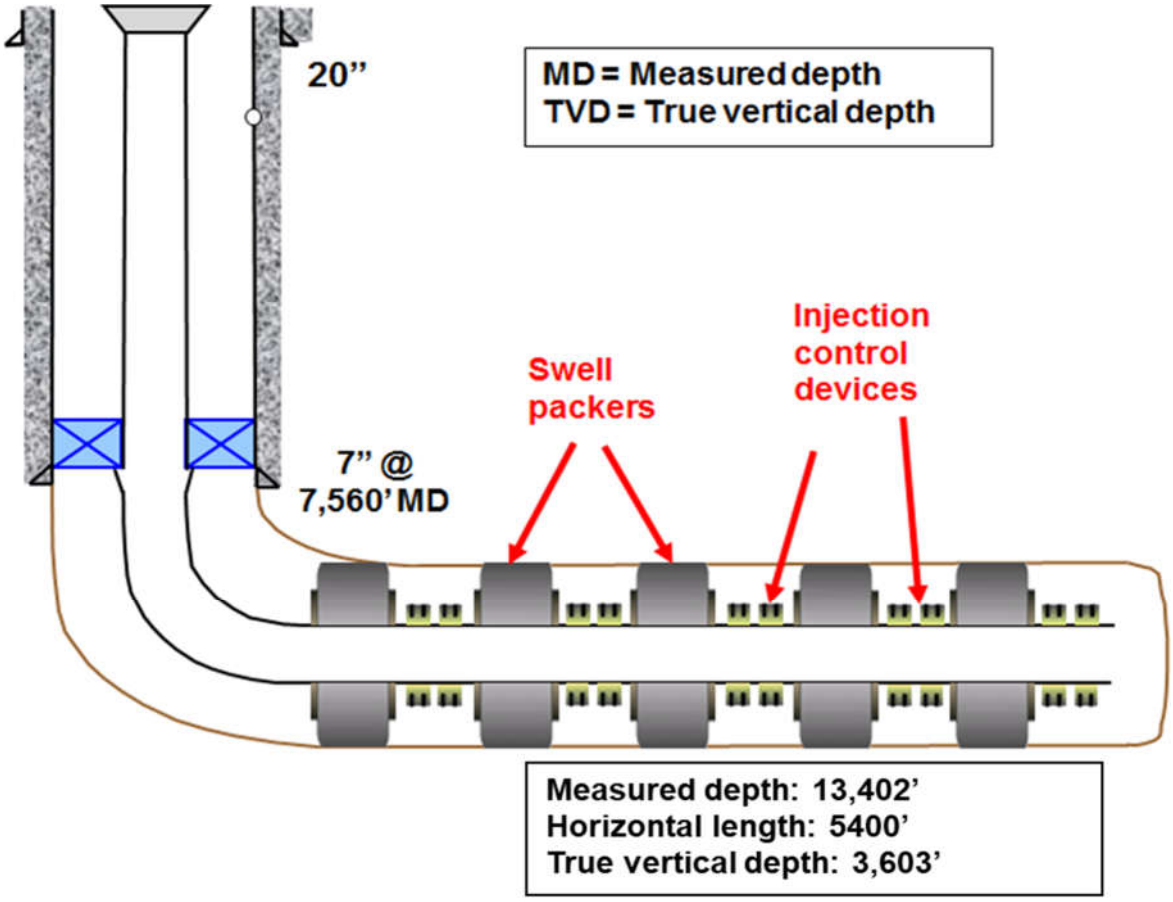

Figure 5.4.4: J-24A wellbore diagram.

Polymer injection Unit

A commercially available, partially hydrolyzed polyacrylamide (HPAM) polymer, Flopaam 3630 by SNF, was chosen for the pilot test based on the oil viscosity, reservoir permeability, and the vendor’s initial lab test results. The polymer injection unit (PIU) was custom designed and manufactured for this project. As shown in **Figure 5.4.5**, the initially installed PIU consisted of 5 modules: the pressure letdown module, the injection pump module, the polymer make-down module, the hopper and the utility module. Polymer powder was transported and stored in super sacs, each containing 750 kg (~1650 lb) of polymer. The super sacs were loaded onto the hopper with a forklift and the polymer was fed into the polymer make-down unit below where it was mixed with water to make a mother solution. After 100 minutes hydration time in the tank, the mother solution was slipstreamed into the main water supply that fed into 3 triplex positive displacement injection pumps in the pumping unit, one for each injector plus a spare.

Figure 5.4.5: Polymer injection unit (source: SNF).

The PIU was installed at the project site in the summer of 2018 and started with water injection for a few days before ramping up polymer injection. Polymer injection started on August 28, 2018 at 600 ppm ramping up to1800 ppm in about 10 days to achieve the initial target polymer viscosity of 45 cP which was deemed to give a unit mobility ratio in the reservoir. Later, the target viscosity was reduced to 30 cP based on the actual injector performance and the understanding that the in-situ polymer viscosity should be higher than the measured viscosity due to the low shear conditions in the reservoir.

The water used for making polymer solution is produced from a source water well (J-02) completed in the Prince Creek formation overlying the Ugnu formation which contains relatively fresh water supply with total dissolved solids of 2600 milligram per liter and total hardness of 280 milligrams per liter. Shortly after polymer startup, we noticed that the source water contains more hydrocarbon gas than expected forcing us to stop injection and modify the electrical components to meet the Class I Division 2 standards (API RP 500 – Recommended Practice for Classification of Locations for Electrical Installations at Petroleum Facilities Classified as Class I, Division 1 and Division 2). Lesson learned here was that operator involvement earlier in design or improved vendor understanding of end user capabilities/needs would likely have resulted in a shorter tie-in window and lower costs.

The polymer injection unit was modified in June 2020 by installing a silo at the test site to improve operation safety and reduce the cost for polymer transportation. Polymer is now transported in bulk from Louisiana to the North Slope by a combination of rail, boats, and trucks. At the test site, polymer is fed pneumatically from the silo to the polymer slicing unit as shown in **Figure 5.4.6**.

Figure 5.4.6: Polymer injection unit with silo.

Polymer solution quality control

Proper Quality Control (QC) is the key for a successful polymer flood. If there is an unexpected early rise in injection pressure, it can be caused by the reservoir itself, or by poorly hydrated polymer. It is therefore important to eliminate poorly hydrated polymer as a cause. Poorly hydrated polymer can be caused by issues such as: water properties (salinity, oxygen content, PH value), freeze protection fluids (diesel/methanol) in source water, polymer dosing/wetting process not running consistently, poor polymer quality from supplier, insufficient hydration time, or insufficient mixing in the hydration tank.

As part of the normal operation of the polymer unit, the following parameters are measured on a daily basis: filter ratio, viscosity, dissolved O_2 concentration, total dissolved solids, PH, and conductivity. The most important parameters to monitor are filter ratio which indicates if the polymer solution will propagate through the reservoir, and polymer viscosity which ensures proper mobility ratio for effective oil displacement.

Initially, a commonly accepted definition of polymer solution filter ratio was adopted (Levitt and Pope, 2008) which was defined as the ratio of the time needed to filtrate from 180 cc to 200 cc to the time needed to filtrate from 60 cc to 80 cc using a specified filtration device. If this ratio was less than 1.2, the polymer solution was considered good enough to flow through the reservoir rocks without blocking. Filter ratio testing was developed as a laboratory analysis and implementing this method in the oilfield required some extra care. After several iterations, standard sampling procedure was established to ensure consistent and unsheared polymer samples were collected for routine testing. For some special bottle tests, the sheared polymer sampling method was used to predict separation and emulsions.

Figure 5.4.7 shows the automated measurement and the intervals used for the filter ratio calculation. In the specific example below the ratio is 1.10, which is considered a passing number. The derivative and the linear fit are also shown in the figure, as any deviation from the linear trend indicated a bad filter ratio. Actions are taken if poor filter ratios are measured. However, it was noticed in the field this filter ratio method sometimes failed to recognize poor polymer hydration.

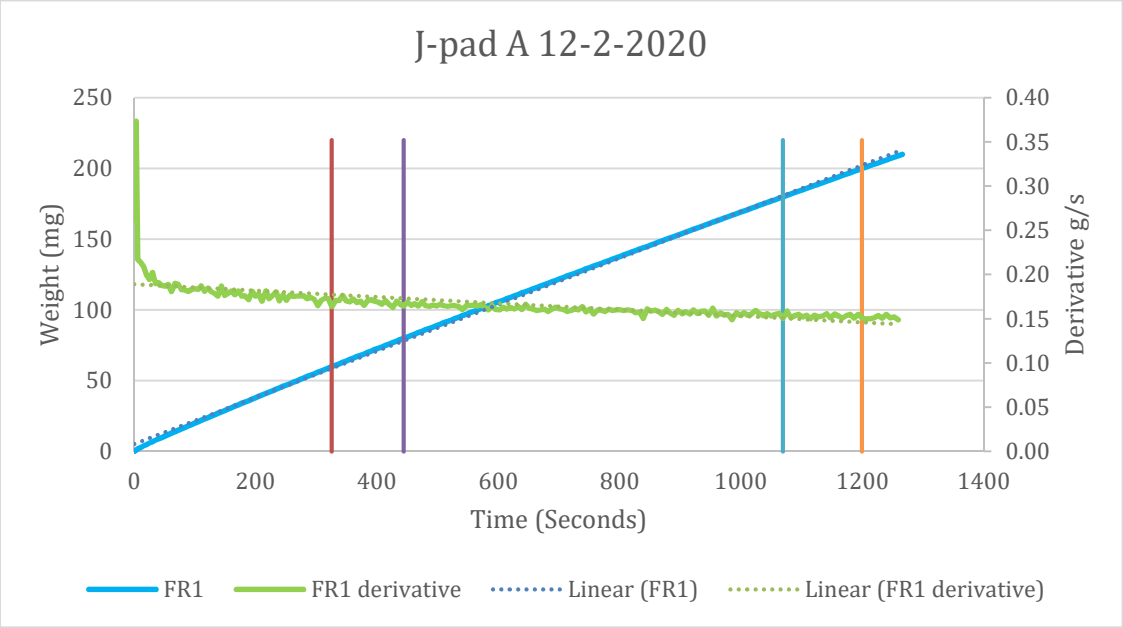

Figure 5.4.7: Automated measurement for polymer solution.

To improve polymer QC, a new definition of filter ratio was implemented (Driver et. al., 2018). It was defined as

$$FB_{\beta} = \frac{1+\beta 190cc}{\beta 70cc} \tag{5.4.1}$$

where $\beta = \frac{2a}{b}$, a and b are first and second quadratic equation coefficients fitted to volume versus time plot. This equation was considered to provide better filtration estimate because it uses the full curve of volume versus time. It was also found that β filter ratio method was less susceptible to human errors. This method was able to indicate poorly hydrated polymer when the prior method did not.

Summary of key results

Polymer Injection Activity Log

- 8/23 polymer injection unit (PIU) online with water
- 8/28 polymer injection starts
- 9/25 PIU shutdown

  - More HC gas found in source water
  - Modify and reclassify PIU to Class I Div II
- 10/15 Resume polymer injection
  - Ran downhole gauge
  - Performed post polymer step rate test
- 11/9 J-23A shut in for PFO while waiting for pump repair
- 11/16 J-24A shut in for PFO while repairing augur
- 12/3 Resume polymer injection
- 1/17/19 Attempted IPROF for J-23A, but tool covered by black goo
- 3/28/19 Pumped 8 kg Tracer T-801 into J-24A
- 3/29/19 Pumped 8 kg Tracer T-803 into J-23A
- 3/29/19 Coil tubing clean out J-23A, repeat IPROF.
  - Tool did not go all the way down, got partial results
  - ICD#1=5.6%, ICD#2=27.8%, ICD#3=40.7%
  - 74% polymer injecting into first segment (heel-2766')
- 6/7/19-6/14/19 J-28 false polymer positive by flocculation test
- 6/19/19 shut down PIU due to polymer hydration issues
- 6/22/19 PIU back online, J-23A rate decreased by 400 bpd, J-24A by 200 bpd
- 7/6/19 J-23A PFO test, no damage identified
- 7/8/19 Treat injectors with hot KCL water to remove damage – not effective
- 7/15/19 J-23A and J-24A step rate test
- 7/18-8/28/19 straight water or low concentration polymer while diagnosing
- 8/29/19 polymer hydration problems resolved, resume polymer injection
- 9/2/19 J-23A and J-24A step rate test
- 12/2/19 shut down PIU to repair augur and replace plungers
- 12/6/19 back online with new plungers
- 1/9/20 install automated filter ratio test
- 5/20/20 Shutdown due to pad maintenance
- 5/21/20 water flush
- 5/26/20 resume polymer injection
- 6/16/20 SD PIU, switch to silo for polymer feed
- 7/4/20 resume polymer injection with silo, reduce viscosity target to 30 cp
- 10/10/20 Shut in J-24A for drill-by
- 10/24/20 Shut in J-23A, J-27, J-28 due to power loss
- 11/1/20 restart polymer skid with water
- 11/5/20 restart polymer injection with low concentration 600-800 ppm
- 1/28/21 J-24 back on polymer injection
- 3/2/21 Gelling issues, clean out and flush
- 5/24/21 J-27 ESP failed following a power failure within MPU
- 6/18/21 J-27 back on production after ESP change out
- 7/3/21 J-23A Injection profile log, good data for ICD #1-6, tractor failed after ICD #6
- 7/4/21 J-24A Injection profile log, no data due to tractor failure
- 8/9/21 switched to Flopaam 3430 polymer at 1500 ppm

- 10/9/21 J-27 lost BHP after field shutdown
- 11/16/21 switched back to Flopaam 3630 polymer at 1200 ppm
- 6/8/22 research group visited polymer injection site
- 7/26/22 J-27 ESP failed again
- 8/24/22 J-27 Replace failed ESP with jet pump

Polymer Injection Performance

As of September 30, 2022, a total of 1,410,625 lbs of polymer had been injected into the two injectors and the total amount of polymer solution injected was 2.99 million barrels which was approximately 18.8% of the total pore volume in the 2 flood patterns. **Figure 5.4.8** shows the history of polymer concentration and viscosity with a current target viscosity of 30 cP. Currently, the injected polymer concentration was set at 1200 ppm and the viscosity varied from 20 to 30 cp. The measured polymer solution viscosity in the lab (at 7.3 1/s) has been lower than the target viscosity. However, since the share rate in the reservoir is much lower (~ 1.0 1/s) than 7.3 1/s, the polymer viscosity would be about 40 cp in the reservoir based on lab measured viscosity versus shear rate curves.

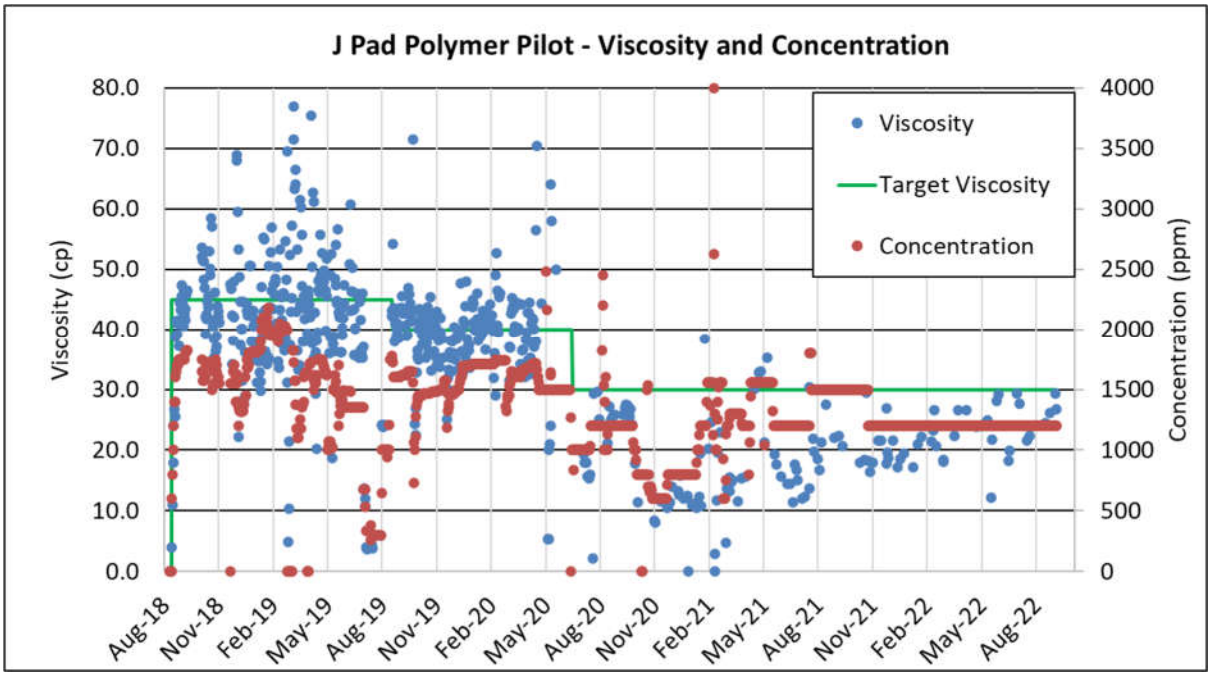

Figure 5.4.8: Polymer concentration and viscosity vs. time.

Figure 5.4.9 presents daily injection rate and pressure for J-23A which shows that the injection rate stabilized at 1800 barrels per day (bpd) with a wellhead injection pressure of approximately 750 psi in the last few months. As of September 30, 2022, a total of 1,032,609 pounds of polymer have been injected into J-23A and the cumulative volume of polymer solution injected is 2.21 million barrels

representing approximately 23.1% of the total pore volume of the flood pattern.

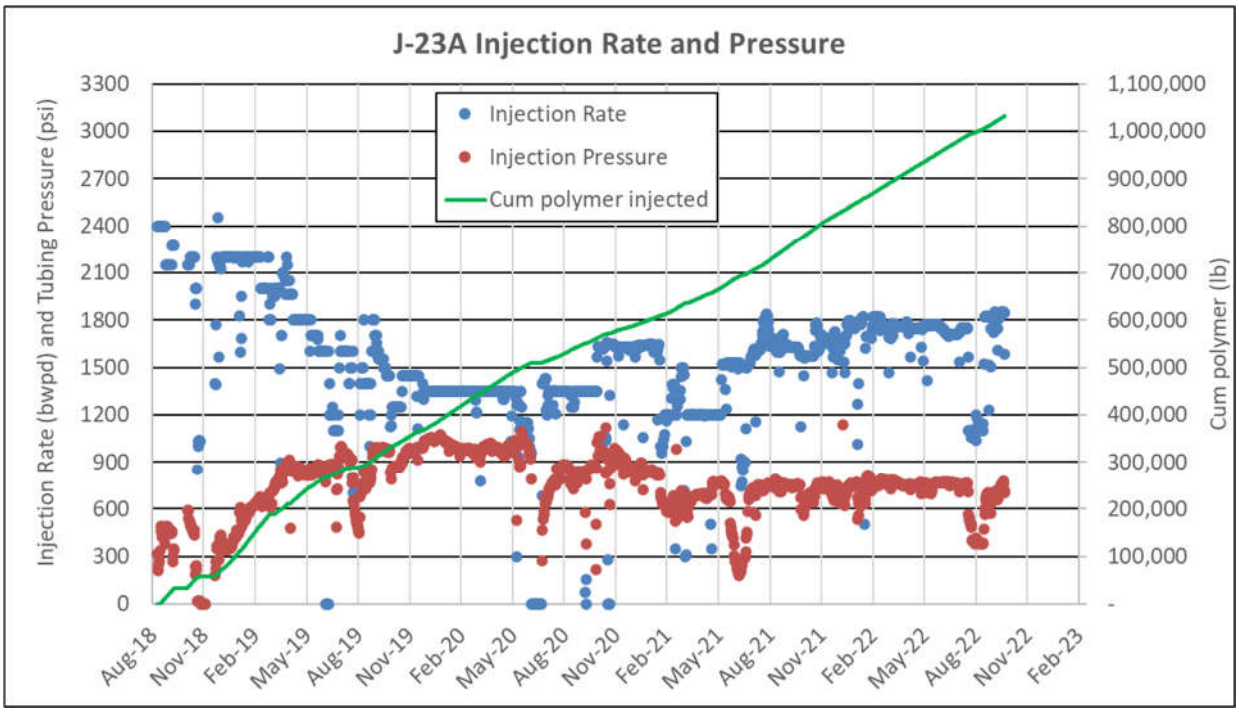

Figure 5.4.9: J-23A injection rate and pressure.

Figure 5.4.10 presents daily injection rate and pressure for J-24A. Recently, the injection rate stabilized at ~450 bpd at a wellhead pressure of approximately 750 psi. To date, a total of 378,016 pounds of polymer have been injected into J-24A and the cumulative volume of polymer solution injected is 0.78 million barrels representing 12.3% of the total pore volume of the flood pattern.

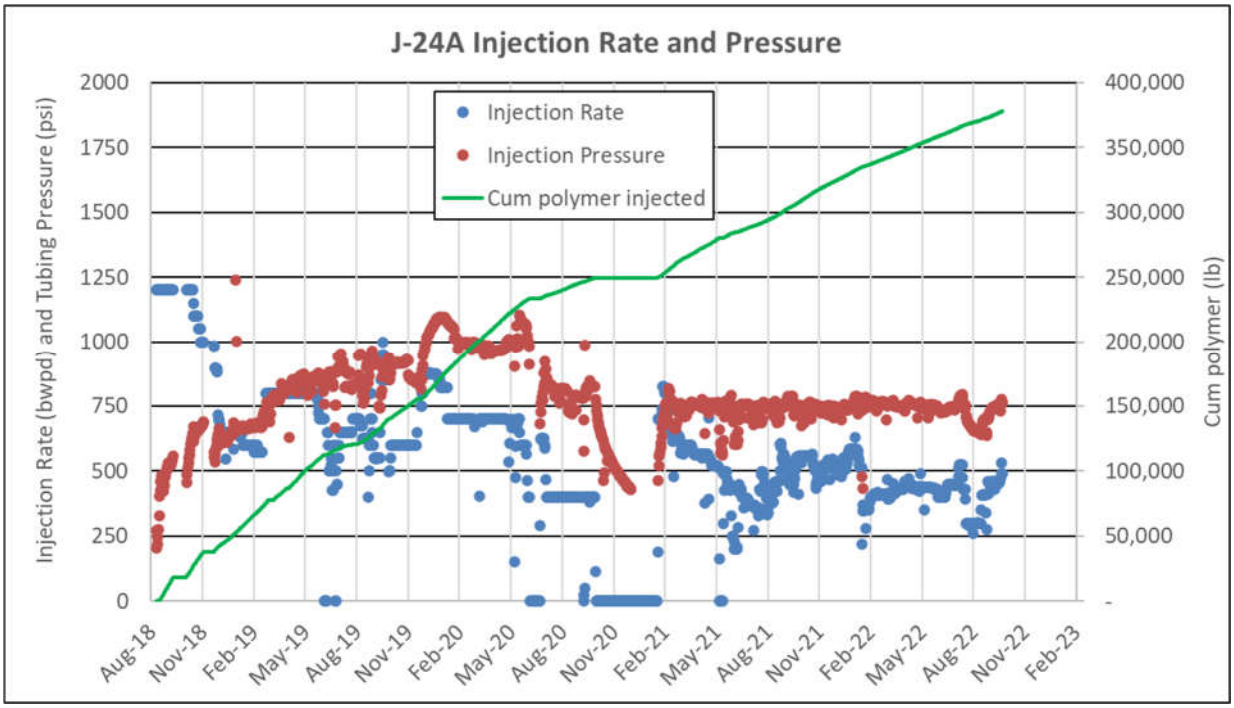

Figure 5.4.10: J-24A injection rate and pressure.

Figure 5.4.11 is a Hall Plot (Hall, 1963) for both J-23A and J-24A, which plots the integration of the differential pressure between the injector and the reservoir versus cumulative water injection. The data would form a straight line if the injectivity stays constant over time, curve up if the injectivity decreases and vice versa. During the early times of polymer injection, injectivity of both injectors was decreasing due to the high polymer viscosity as well as some poorly mixed polymer. After some improvements on the PIU, the injectivity stabilized for about 2 years followed by an increase which was likely due to polymer breakthrough combined with the decrease in polymer viscosity. During the last year of the pilot, the injectivity of both injectors stabilized again.

The injector performance during the 4-year pilot test has proven that sufficient polymer injection can be achieved via horizontal wells in the Schrader Bluff formation. The pilot has also proven that polymer transportation and mixing can be done properly under the arctic conditions of the Alaska North Slope.

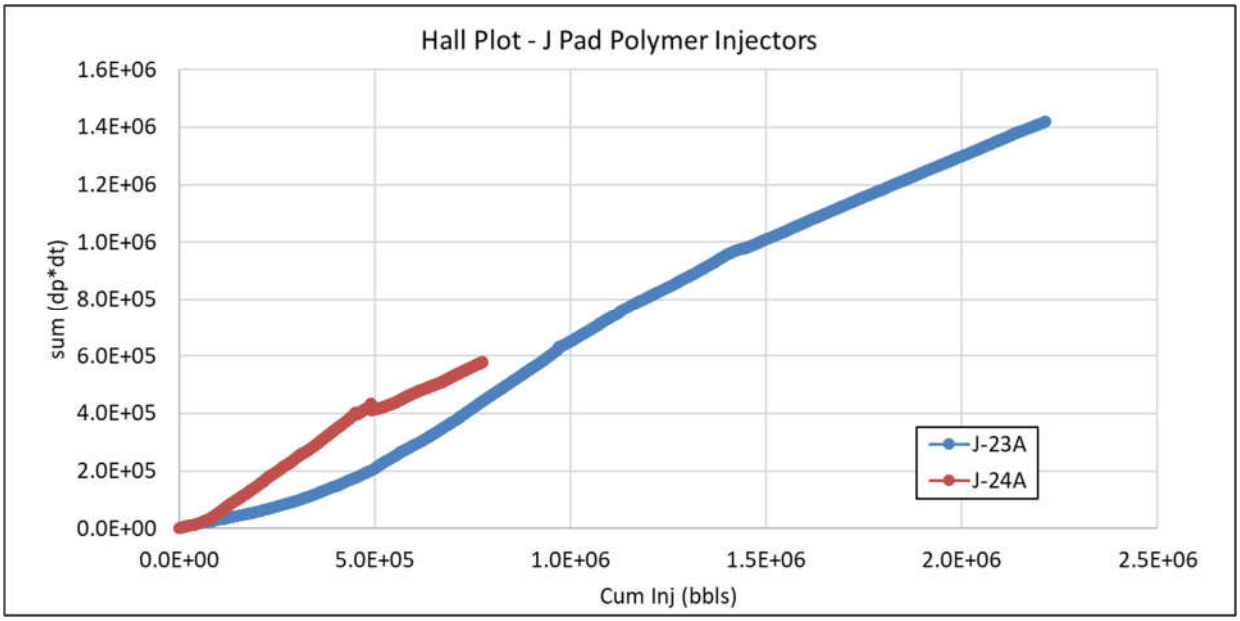

Figure 5.4.11: Injection Hall plot.

Production Performance

Figure 5.4.12 depicts the production performance of producer J-27 which is supported by both injectors, J-23A from the south side and J-24A from the North. The oil rate declined from late 2018 to late 2019 due to decreasing injection rate after polymer startup, but the water cut decreased dramatically due to the effect of polymer. Then from late 2019 to mid-2021, the oil rate inclined from ~500 bpd to ~800 bpd as the water cut decreased from ~65% to less than 10%. On May 24th, 2021, the ESP in producer J-27 failed after 5 years of service which was longer than the average ESP run life at Milne Point field. The ESP was changed out and the well was put back on production on June 18th, 2021. Then on July 26th, 2022, the ESP in J-27 failed again after a short 13 months of service. A rig workover was conducted to replace the failed ESP with a jet pump and the well was put back on production on August 24th. Current oil rate is approximately 600 bpd. The water cut inclined from ~10% in mid-2021 to ~40% in mid-2022. The sharp increase in water cut after the jet pump startup was likely caused by measurement errors since the jet pump uses water as power fluid. Recent well tests show that the water cut in J-27 stabilized at ~50%.

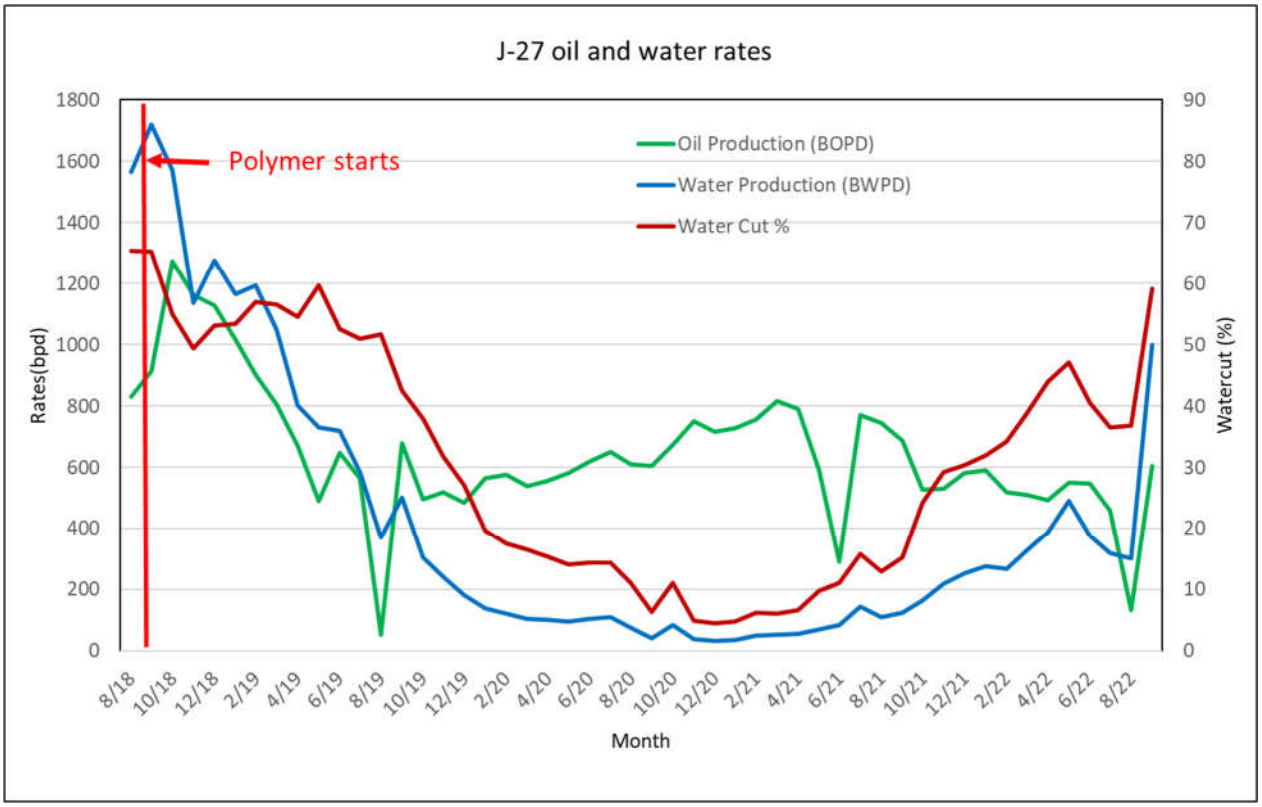

Figure 5.4.12: J-27 production performance.

Figure 5.4.13 depicts the production performance of producer J-28 which is supported only by J-23A from the north since the south side is adjacent to a sealing fault. Water cut decreased from 70% at the start of polymer injection to less than 10% by the end of 2020. The fast response in water cut shortly after polymer startup is most likely caused by polymer blocking off the water fingers developed during the prior waterflood process. The oil rate inclined from early 2019 to late 2019 and then stabilized at 500-550 bpd. The water cut started to increase since early 2021 along with polymer breakthrough. In May 2022, water cut increased drastically from 57% to 73% and the oil rate decreased from ~550 to ~370 bpd, indicating some additional polymer breakthrough. Recently, oil rate stabilized at ~360 bpd and water cut stabilized at ~70%.

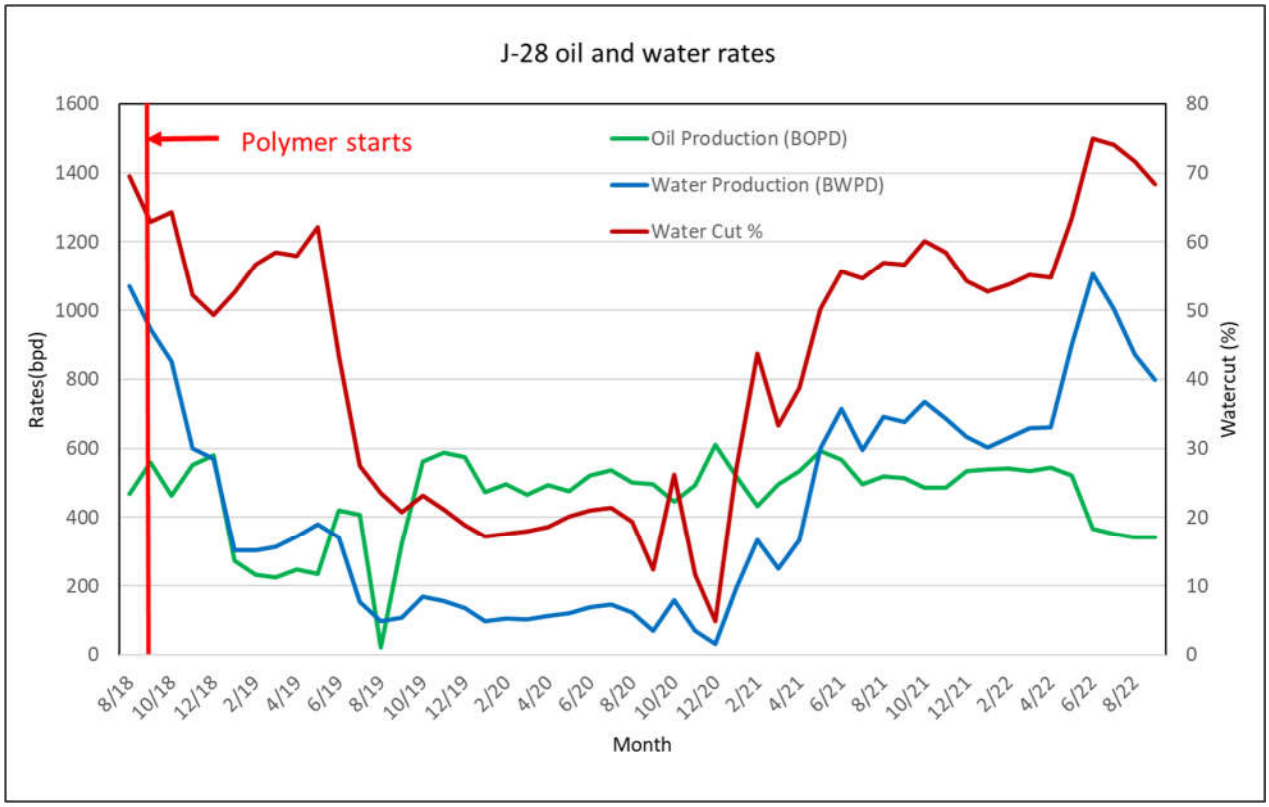

Figure 5.4.13: J-28 production performance.

Monitoring Polymer Breakthrough

Since the start of polymer injection, produced water samples have been collected bi-weekly when possible and analyzed onsite using the clay flocculation test, as well as in the laboratory via chemiluminescent nitrogen analyses to detect the presence of produced polymer in the production stream. Polymer production was first confirmed in the water sample collected on 10/10/2020 from producer J-27 with a polymer concentration of 197 ppm, while polymer was first seen from J-28 in the 12/13/2020 sample with a polymer concentration of 629 ppm. This means that polymer breakthrough time is approximately 26-28 months in the pilot patterns. Detailed data of produced polymer concentration are summarized in **Section 5.1** of this report.

EOR benefit

Figure 5.4.14 plots the actual oil production rate with polymer flood compared with predicted oil rate had waterflood continued without polymer. The difference between the two curves is deemed as EOR benefit. Current oil rate is approximately 950 bopd from the two producers and the predicted oil rate without polymer injection is about 250 bopd, giving an estimated EOR benefit of approximately 700 bopd. During the pilot period, oil rate increased by 700-1000 bopd over predicted waterflooding rate. Polymer flooding more than tripled oil rate compared with waterflooding alone.

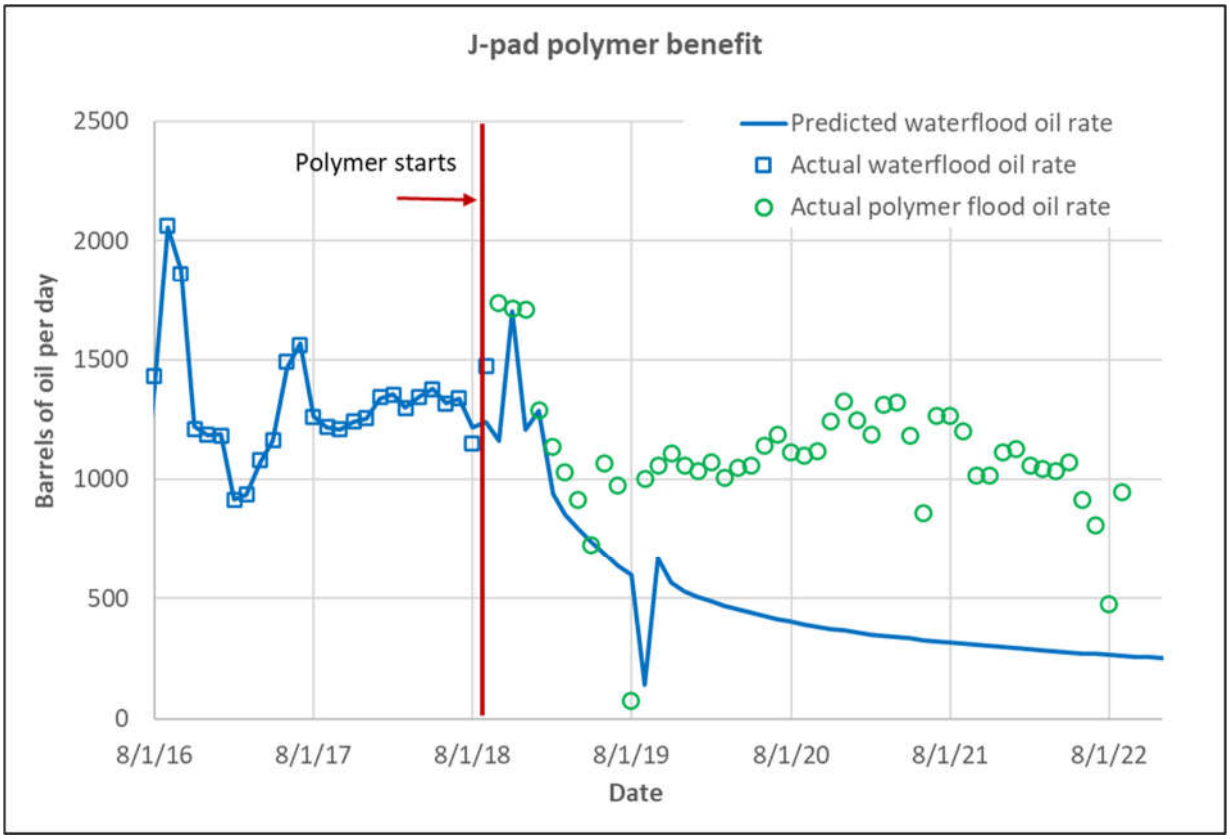

Figure 5.4.14: Incremental oil rate over waterflood.

As of the end of September 2022, estimated cumulative Incremental Oil Recovery (IOR) is approximately 832,000 bbls from polymer injection and cumulative polymer injected is 1,410,000 lbs. If we define polymer utilization as the ratio of cumulative amount of polymer injected to cumulative IOR, polymer utilization of this pilot would be approximately 1.7 pounds of polymer injected per barrel of incremental oil produced (lbs/bbl) which is much lower than the polymer utilization numbers reported in the literature on any other polymer flood projects around the world.

Main findings of practical significance

The pilot test lasted four years and one month at Milne Point J-pad. Here are the main findings of practical significance:

- Polymer can be cost effectively shipped in bulk volumes to the North Slope of Alaska via a combination of rail, boats, and trucks. Polymer can be sufficiently mixed and pumped year-round under the arctic conditions.
- High viscosity polymer solution can be injected at sufficient rate via horizontal wells to perform polymer flooding EOR in the Schrader Bluff heavy oil reservoir.
- Polymer flood drastically reduced water cut from ~70% to less than 10% one year after polymer startup.

- Polymer breakthrough timing was 26-28 months from the start of polymer injection into the 2 pilot patterns.
- During the pilot period, oil rate increased by 700-1000 bopd over predicted waterflooding rate. Polymer flooding more than tripled oil rate compared with waterflooding alone.
- During the 4-year pilot period, cumulative polymer utilization was 1.7 lbs of polymer per barrel of incremental oil produced, which was the best polymer flooding performance indicator ever reported in the world.

Topical publications

1) *Samson Ning, John Barnes, Reid Edwards, Walbert Schulpen, Abhijit Dandekar, Yin Zhang, Dave Cercone, Jared Ciferno: First Ever Polymer Flood Field Pilot to Enhance the Recovery of Heavy Oils on Alaska North Slope – Producer Responses and Operational Lessons Learned. Virtually presented at the 2020 SPE ATCE, October 28, 2020.*
2) *Samson Ning, John Barnes, Reid Edwards, Kyler Dunford, Abhijit Dandekar, Yin Zhang, Dave Cercone, Jared Ciferno: First Ever Polymer Flood Field Pilot to Enhance the Recovery of Heavy Oils on Alaska North Slope – Polymer Injection Performance, Unconventional Resources Technology Conference Denver, CO July 22-24, 2019.*

5.5 Analysis of Effective Ways to Treat Produced Water Containing Polymer

The polymer molecules and/or fine clay particles that may get migrated (note the unconsolidated formation) along with the produced fluids has the potential to negatively impact the oil-water separation, which is one of the major concerns for field operators at the Milne Point Unit (Chang, 2022). The formation of complex and stable emulsions, that may get exacerbated by the ESPs used in lifting production from polymer flooding, could upset the separation facilities and disrupt existing field operations; consequently, leading to production impairment and even risk outweighing the benefits of the polymer pilot. Chang (2022) has tabulated problems encountered in polymer flooding projects from other parts of the world. Therefore, a systematic study to investigate the potential emulsion problems (and their solution), related to polymer breakthrough, at the J-pad polymer pilot is important from the standpoint of overall success of the project. Accordingly, numerous parametric and mechanistic experimental studies were conducted throughout the course of the project in order to examine the behavior of the emulsions for developing and documenting a practical treatment for processing the produced stream containing oil, water, spent polymer and clay. The two topical publications, RPPRs and the PhD thesis (Chang, 2022) provide extensive details and specifics of all the experiments and the results; however, included below is the design of experiments, key results summary and the main finings of practical significance.

Design of experiments

The experiments that were designed and conducted were planned in such a way that enabled qualitative as well as quantitative testing of a multitude of variables such as water cut, salinity, oil type, polymer concentration, clays, emulsion breakers, and additives. All emulsions were analyzed using either microscopy, visual bottle tests and/or turbiscans. Performance criteria such as separation efficiency, time, BS&W, oil content in water etc. were utilized to rank the emulsion breakers. **Table**

5.5.1 provides a concise summary of all the experiments.

Table 5.5.1: Test matrix for emulsion studies to screen an emulsion breaker (and additive).

Parameters/Variables	Mechanisms	Test Fluids and Materials	Test Conditions	Screening Criteria/Evaluation of Results
• 20% and 50% WC • Produced water TDS 5,230 ppm (pH 9.0) and 6,656 ppm (pH 5.61) • Polymer concentration 0–800 ppm (sheared and unsheared) • Four oil-soluble and one water-soluble emulsion breaker 10 – 500 ppm dosage • Compound emulsion breakers • KCl concentration 0–20,000 ppm • Clay concentration 0–0.25 wt% (clay addition to oil vs. water)	• Drop size distribution • Particle size analysis • Micromorphology of emulsions • IFT using pendant drop • Interfacial viscoelasticity	• Filtered produced water • Produced dead heavy oil (ρ and μ of 0.9557 g/cm^3 and 3,500 cP) • Flopaam 3630S of 18-20 million Dalton and 30% hydrolysis • Commercial emulsion breakers E12, E18, N16, R13 and DEPO11 • Na-Mt, Ca-Mt, Kaolinite and Illite clays	• Polymer mother solution diluted to desired concentrations • Polymer solution viscosity measured at shear rates of 100 – 750 S^{-1} • Emulsions prepared by a homogenizer at 5,000 and 15,000 rpm for 3 mins to mimic ESP shearing • Fixed temperature of 130°F and atmospheric pressure	• Demulsification efficiency • Separation speed • Separated water clarity or OIW • Dosage rate • BS&W • Rag layer • Turbiscan Stability Index • Elastic modulus E′ and loss modulus E″ • Dynamic and equilibrium IFT • Drop size • Radar chart

Summary of key results

In this section representative results that are primarily related to the screening criteria in **Table 5.5.1** are presented and discussed that lead to the screened emulsion breaker (and additive) and the main findings. **Figure 5.5.1** and **5.5.2** present the demulsification efficiency as a function of time or

separation speed and the separated water quality at 50% WC for no polymer and 800 ppm concentration, respectively. Generally, a superior performance of both E12 and the E18 emulsion breakers is clearly seen from both figures, for a 50% WC (and 800 ppm polymer), which is representative of the producer performance at the late stage.

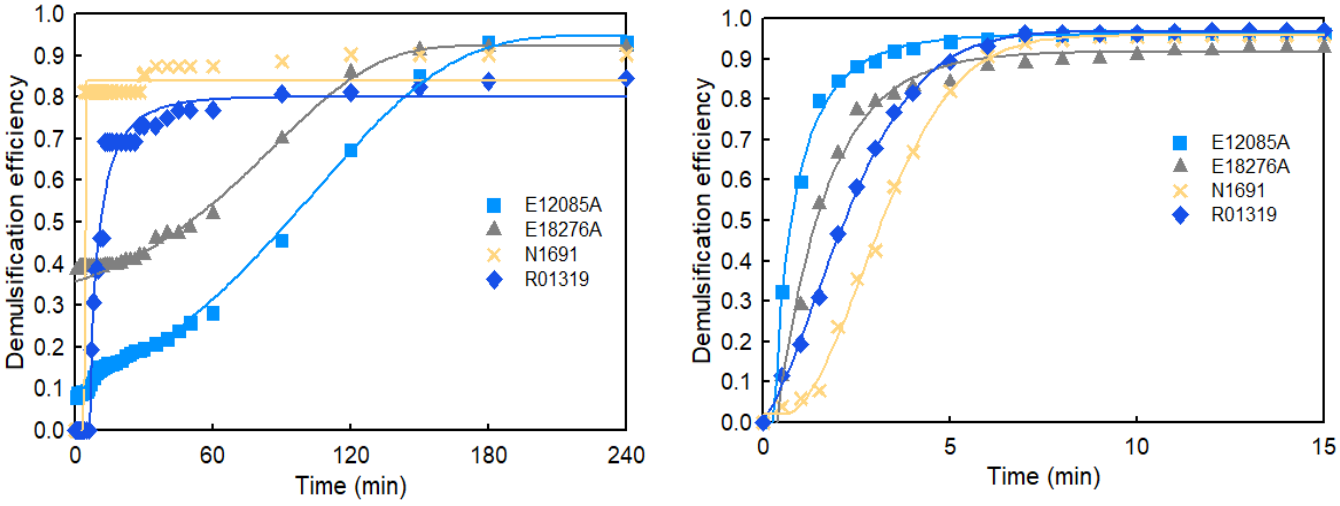

(a) No polymer (b) 800 ppm polymer

Figure 5.5.1: Demulsification efficiency and separation speed for the tested emulsion breakers (dosage 100 ppm) at 50% WC (Chang et al. 2020).

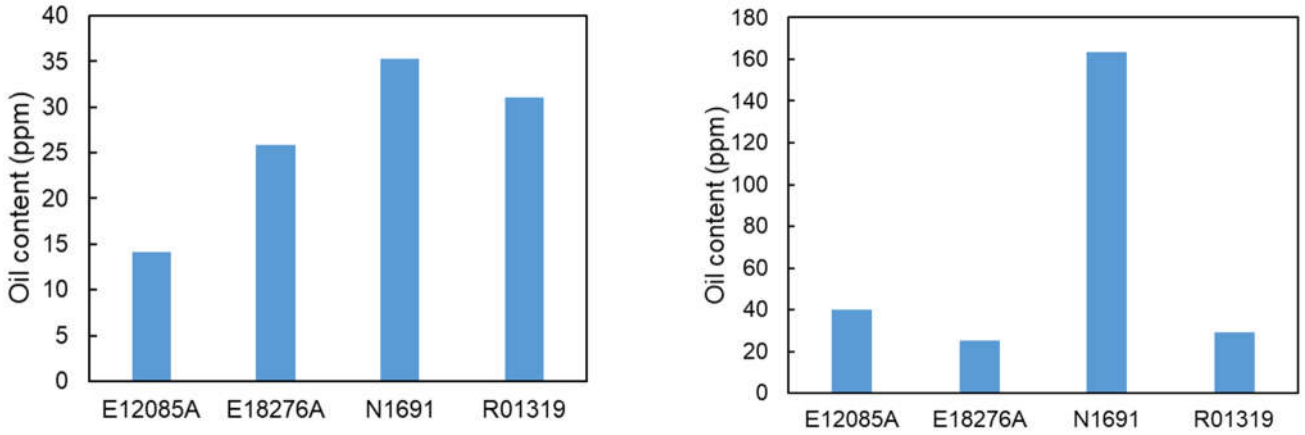

(a) No polymer (b) 800 ppm polymer

Figure 5.5.2: Oil content in separated water for the tested emulsion breakers (dosage 100 ppm) at 50% WC (Chang et al. 2020).

Given the relatively better efficacy of the E18 emulsion breaker (compared to E12) based on other conditions (Chang et al., 2020), it was selected for dosage comparison. Although the separation efficiency increased with the dosage rate, it was at the expense of higher OIW. Therefore, compound emulsion breakers also were tested to investigate if their individual chemistries could be leveraged in

a blend. **Figure 5.5.3** compares the performance of equal part compound emulsion breakers E12+N16, E12+R13, and E12+E18, with E12. The E12+E18 combination is the most promising, which achieved a faster and more efficient separation. Although the OIW for E12+E18 is a bit higher than E12 alone and twice the E12+N16 blend, the values for all cases are much less than the 100 ppm threshold (personal communication with Hilcorp cited in Chang et al. 2020).

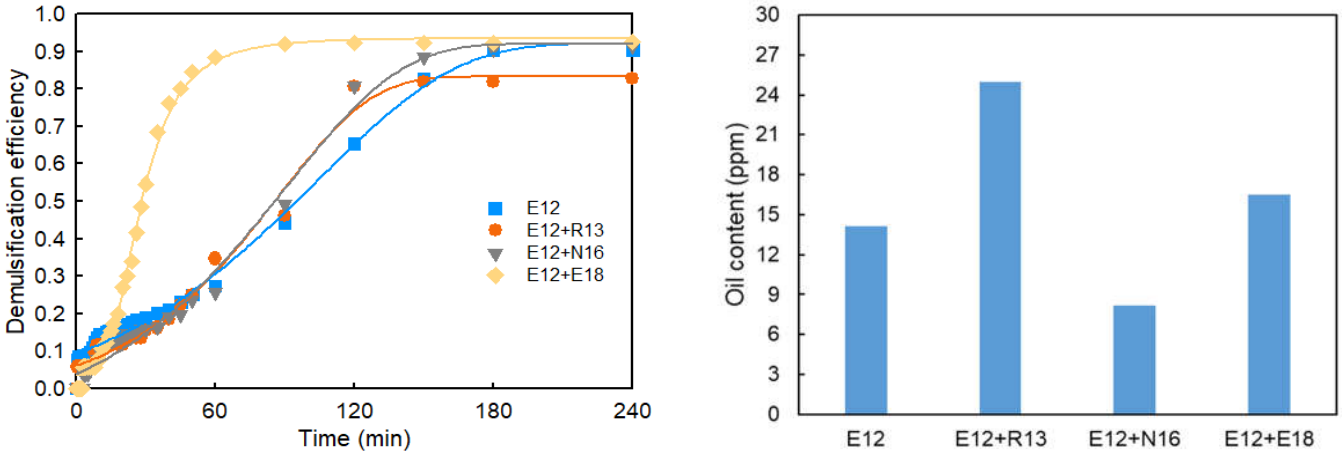

Figure 5.5.3: Demulsification efficiency and oil content in separated water for E12 and equal part blends with E18, R13 and N16 at a 100 ppm dosage for 50% WC and no polymer (Chang et al. 2020).

In order to provide an integrated screening criteria for the tested emulsion breakers, the four different performance indicators, namely demulsification efficiency, water clarity, separation speed and dosage were combined in the form of a radar or spider chart. For example, the demulsification efficiency is expressed by a ratio of V_s and V_t, where the former is the separated water volume at 4 hours and the latter is the total water volume. A 100% efficiency or a value of 1 means complete separation or demulsification. Equations for other performance indicators (see Chang et al., 2020) are similar; in that a value of 1 is ideal or perfect. A radar chart with the four performance indicators will have four corners with a maximum value of 1 and thus the extent spanned by a given emulsion breaker determines the overall efficacy. **Figure 5.5.4** shows two radar charts for a side by side comparison of the tested emulsion breakers and the blends. In the absence of polymer (**Figure 5.5.4 a**), both E12 blends show a somewhat similar better performance; however, overall the expanse of the E12+E18 blend toward the corners of the radar chart is much more uniform. **Figure 5.5.4 b** compares the same two E12 blends and E12 and R13, respectively, at 50% WC and 800 ppm polymer concentration. Although in terms of the demulsification efficiency, separation speed and dosage all the tested emulsion breakers exhibit similar performance, water clarity is markedly better in the case of E12+E18 blend. Therefore, given the superiority of the E12+E18 blend it was subjected for further evaluations.

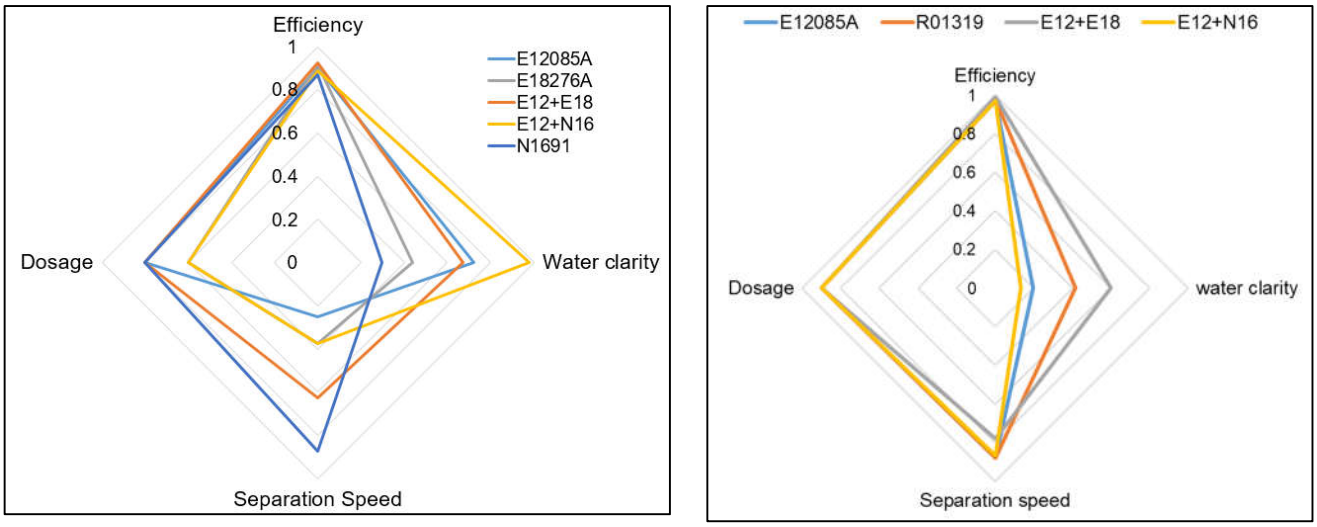

(a) No polymer (b) 800 ppm polymer

Figure 5.5.4: Radar chart for the tested emulsion breakers and blends at 50% WC (Chang et al. 2020).

In the subsequent set of testing, the emulsification characteristics and the electrolyte-optimized demulsification was investigated. First the morphology of the emulsions containing varying polymer concentrations was investigated that included separation behavior; drop size distribution (DSD); interfacial tension and interfacial dilational rheology. **Figure 5.5.5** shows the influence of Flopaam3630S on the emulsion characteristics at 75% WC. At all tested Flopaam 3630 concentrations, the emulsion tends to separate into two phases that includes the top w/o emulsion and the bottom separated water which is o/w emulsion within the given time frame. It is observed that the OIW rapidly increases with Flopaam 3630 concentration, imposing a potential challenge to reduce the oil content to a level that is acceptable either from a discharge or reinjection point of view. At all tested Flopaam 3630 concentrations, a concentrated o/w emulsion layer, sandwiched between the top w/o emulsion layer and the bottom separated water layer is always observed during the separation process. This intermediate layer persists and gets aggravated with time.

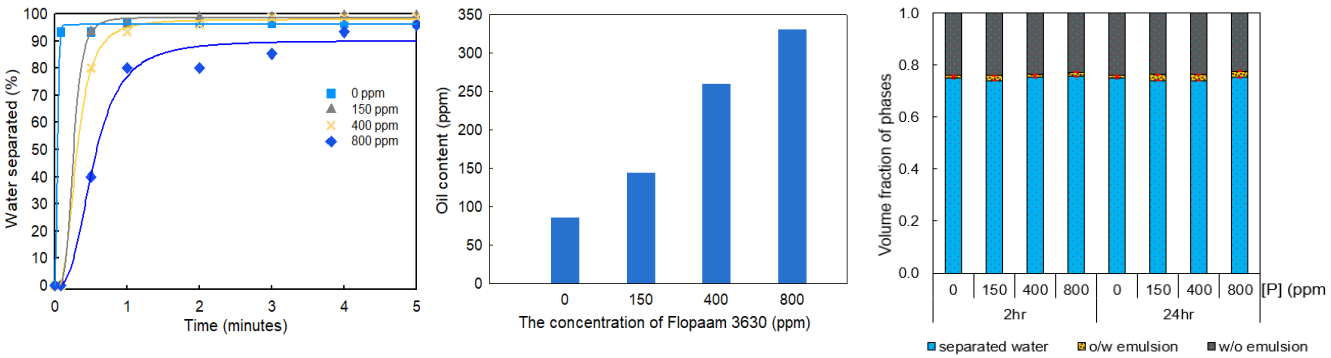

Figure 5.5.5: The effect of Flopaam 3630 on separation kinetics, quality of separated water, and phase volumes at 75% WC in the emulsion formed under moderate shearing conditions (Chang et al. 2022).

The emulsion characteristics were also studied using the DSD (200 × magnification observed under microscope), which is one of the most critical parameters dictating emulsion stability. As a rule of thumb, the smaller droplet size results in a more stable emulsion (Moradi et al. 2010). **Figure 5.5.6** shows the influence of Flopaam 3630 concentration on DSD for emulsion right after the homogenization. It is observed that the emulsion free of Flopaam 3630 is relatively unstable owing to the presence of a great number of larger droplets. The increase in the frequency of smaller droplets and the decrease in the number of larger droplets indicate the enhanced emulsion stability as Flopaam 3630 concentration rises. Apparently, this result is qualitatively consistent with the bottle test result discussed above.

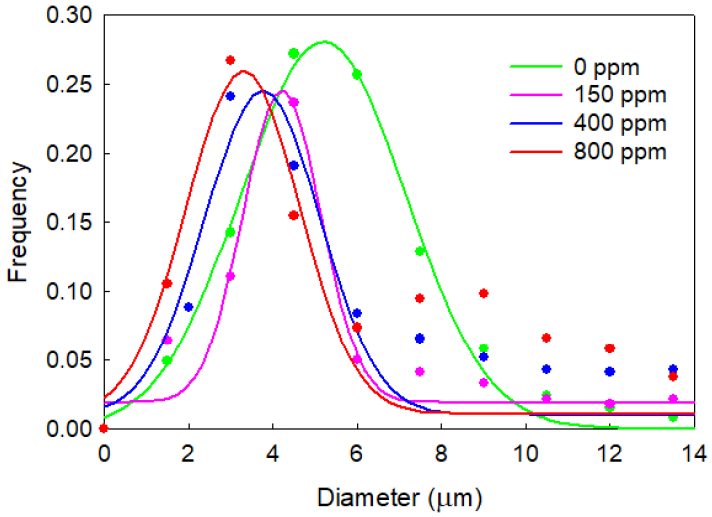

Figure 5.5.6: DSD as a function of Flopaam 3630 concentrations for emulsions right after the homogenization (Chang et al. 2022).

From a mechanistic standpoint, IFT and interfacial dilational rheology measurements also were carried out to further probe the emulsion characteristics. IFT measurements using the pendant drop method were performed to illustrate the penetration of Flopaam 3630 molecules at the oil/water interface. Though the equilibrium IFTs varied within the range of 9.4–10 mN/m, the values were independent of the concentration (0 – 450 ppm) suggesting that Flopaam 3630 cannot diffuse and absorb onto the oil/water interface owing to its weak interfacial activity. Therefore, it was deduced that neither the dynamic IFT nor equilibrium IFT is well correlated with the emulsion stability, vis-a -vis IFT is not the determinant factor to the stability of the emulsion containing Flopaam 3630. This finding provides further evidence for the poor interfacial activity of Flopaam 3630 molecules as suggested by the equilibrium IFT measurements. The storage modulus E′ and the loss modulus E″ at frequencies ranging from 0.01 to 1 Hz were also found to be independent of Flopaam concentrations (0 – 800 ppm), which suggests that polymer has a negligible role in the interfacial rheology. The IFT and interfacial dilational rheology data for the tested Flopaam concentrations is shown in **Figure 5.5.7**.

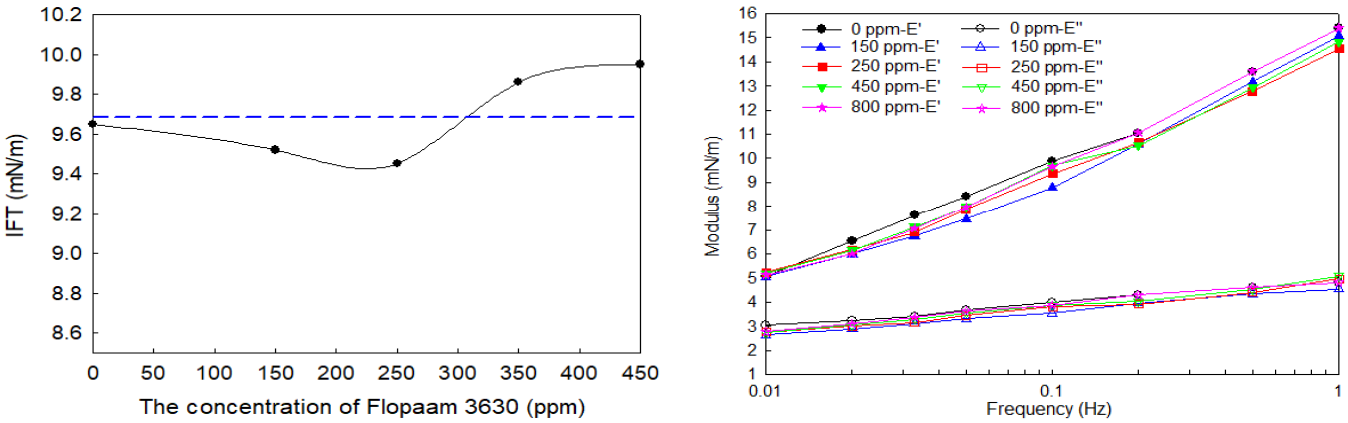

Figure 5.5.7: The equilibrium IFT, storage and loss moduli E′ and E″, respectively (Chang et al. 2022).

In the following batch of experiments, the effect of the compound emulsion breaker (E12+E18), electrolyte KCl, and a combo of E12+E18+KCl were also investigated under moderate and vigorous mixing. The Flopaam concentration was fixed at 800 ppm in all the tests. The BS&W in the oil phase, the volume percentage of the intermediate layer, and the OIW were measured to characterize the performance of these demulsifiers. In addition, IFT and interfacial rheology measurements were carried out to better understand the demulsification mechanisms. **Figure 5.5.8** depicts a side by side comparison of BS&W and OIW for moderate and vigorous mixing, respectively. As seen in **Figure 5.5.8 a**, even at a low dosage rate the addition of demulsifiers reduces the BS&W, OIW, and eliminates the intermediate layer, but in particular the superior performance (as also documented in other tests) of the compound E12+E18 emulsion breaker stands out with the lowest BS&W and OIW. However, under vigorous mixing conditions and the 10 ppm dosage the E12+E18 emulsion breaker results in nearly 4 times higher BS&W and two orders of magnitude greater OIW, which drastically reduces when the dosage is increased by a factor of 10 (**Figure 5.5.8 b**); consequently, increasing the treatment cost. This was one of the motivating factors to test inorganic electrolytes such as KCl from an economic viewpoint.

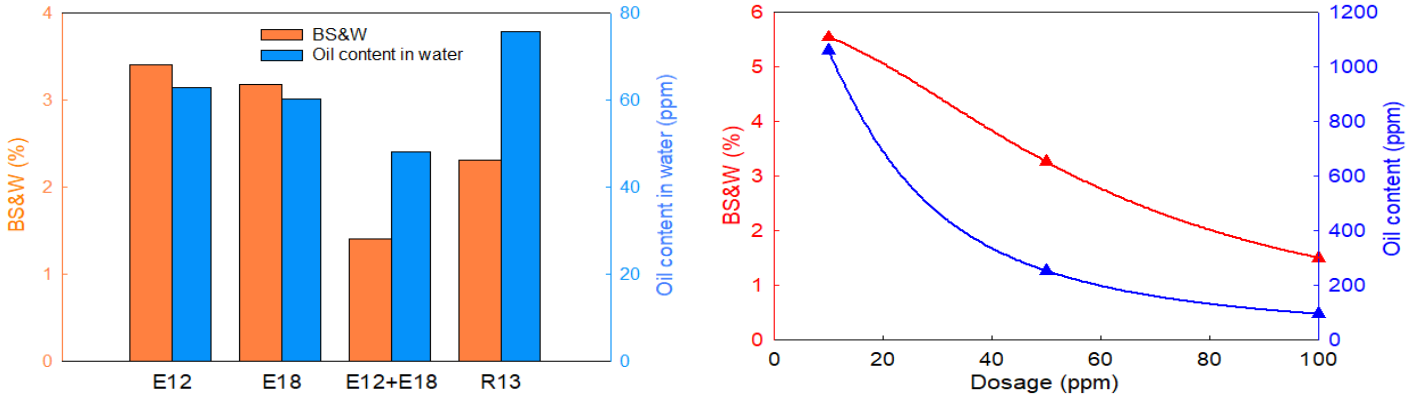

(a) Moderate mixing (10 ppm dosage) (b) Vigorous mixing (E12+E18)

Figure 5.5.8: Effect of dosage, mixing and emulsion breakers on BS&W and OIW at 75% WC (Chang et al. 2022).

Thus, the applicability of KCl alone and combined with E12+E18 to treat the emulsions with and without Flopaam 3630 under vigorous mixing conditions was investigated in this study. As shown in **Figure 5.5.9**, the elevated KCl concentration brings down both BS&W as well as OIW for all the tested cases. However, the presence of polymer adversely affects the performance of KCl. For this reason, the performance of KCl combined with E12+E18 at a dosage of 10 ppm and 50 ppm was evaluated to develop a more cost effective demulsification formula. The positive effect of adding the compound emulsion breaker is demonstrated in the second right graph of BS&W and OIW, in **Figure 5.5.9**. Although the increase in KCl concentration reduces both BS&W and OIW there appears to be a threshold, in that at concentrations as high as 20,000 ppm the 0 ppm and 50 ppm dosage emulsion breaker curves tend to merge. A careful examination of these results thus suggest that a synergistic combination of 8,000 ppm KCl and 50 ppm E12+E18 could be considered as optimal for treating the emulsions. Another notable advantage of this combination is the complete elimination of the intermediate layer as shown in the right most graph in **Figure 5.5.10**.

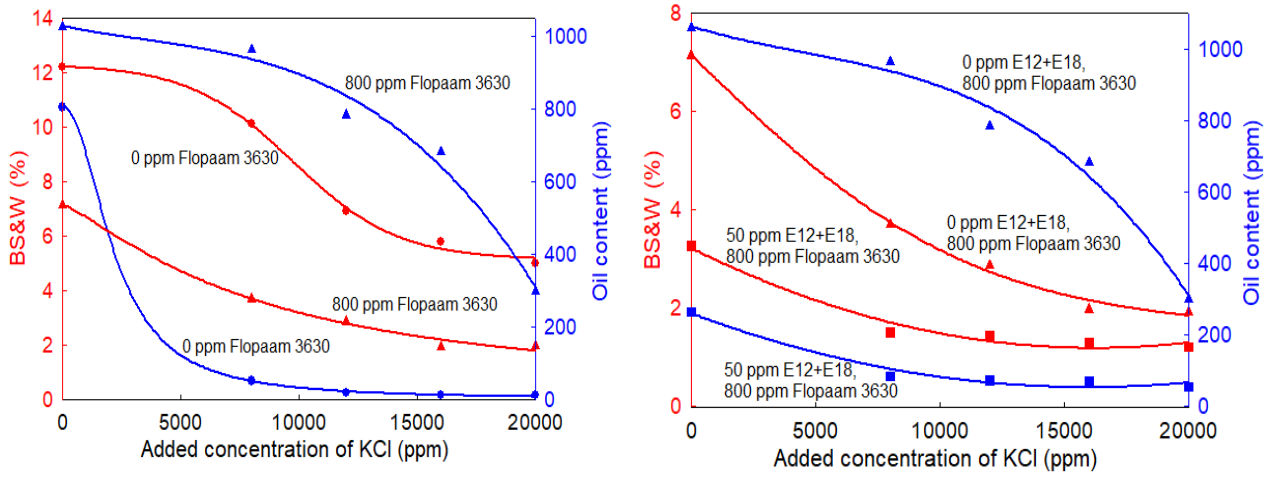

Figure 5.5.9: Effect of KCl alone and combined with 50 ppm E12+E18 on emulsions formed, with and without Flopaam, under vigorous mixing conditions (Chang et al. 2022).

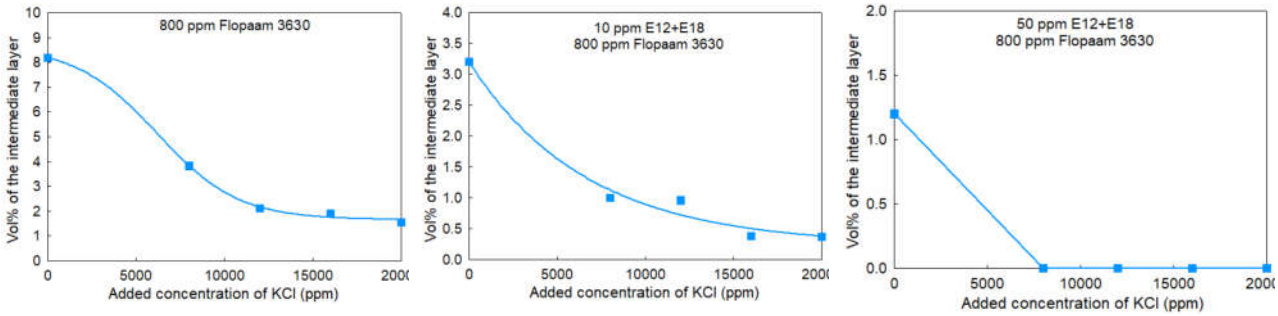

Figure 5.5.10: Effect of KCl alone and combined with 50 ppm E12+E18 on volume % of the intermediate layer, with Flopaam, under vigorous mixing conditions (Chang et al. 2022).

Similar to the earlier studies, IFT and interfacial dilational rheology measurements for KCl additions

also were carried out to further probe the emulsion characteristics from a mechanistic standpoint. **Figure 5.5.11 a** compares the dynamic IFT of multiple emulsion breakers at a concentration of 200 ppm in heavy oil which equals 50 ppm in the total emulsion. With the addition of emulsion breakers, the oil/water IFT immediately decreases and is subject to two stages. The rapid decline of IFT at the first stage is correlated to the diffusion and absorption of emulsion breaker molecules. The IFT values in **Figure 5.5.11 a** are listed in the ascending order of IFT, which actually corresponds with the OIW trend in **Figure 5.5.8 a**. The effect of KCl concentration on equilibrium IFT is shown in **Figure 5.5.11 b**, which indicates that no matter with or without the emulsion breaker, the addition of KCl does reduce the IFT, vis-à-vis inverse proportionality to the ionic strength. Note that the KCl was added to the aqueous phase in concentrations of 10,667, 16,000, 21,333, and 26,667 ppm, which is equivalent to 8,000, 12,000, 16,000, and 20,000 ppm in the total emulsion, respectively. Considering the results depicted in the right most graph of **Figure 5.5.9** and **Figure 5.5.11**, the BS&W, OIW and IFT, respectively, all decrease with increasing ionic strength; thus, lower IFT is likely correlated with better demulsification performance.

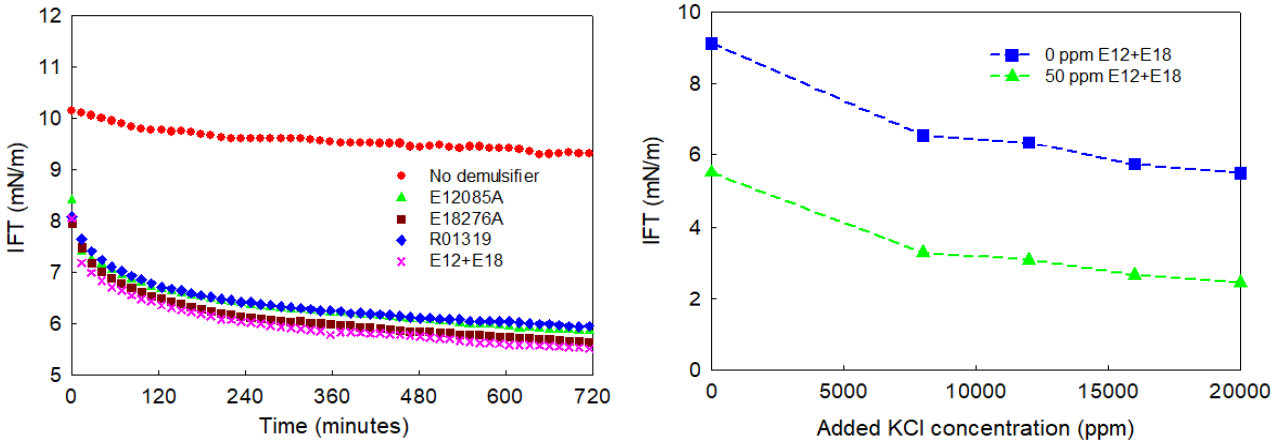

Figure 5.5.11: The oil–water IFT with and without different emulsion breakers (no KCl) and as a function of KCl concentration with and without the addition of 50 ppm E12+E18 emulsion breaker (Chang et al. 2022).

Apart from the capacity of demulsifier molecules to absorb onto the oil/water interface, another important factor in determining the demulsifier performance is the alteration of interfacial viscoelasticity. As shown in **Figure 5.5.12**, compared to the sample without the demulsifier, all four demulsifiers could reduce the elastic modulus E′ and loss modulus E″, respectively. In particular, the effect of the E12+E18 emulsion breaker is relatively much more pronounced. If the IFT values in the left most graph of **Figure 5.5.11** and the modulus values in **Figure 5.5.12** are considered, then it can be readily noted that the compound emulsion breaker E12+E18 shows the lowest IFT and interfacial dilational rheology, contributing to the lowest BS&W and OIW.

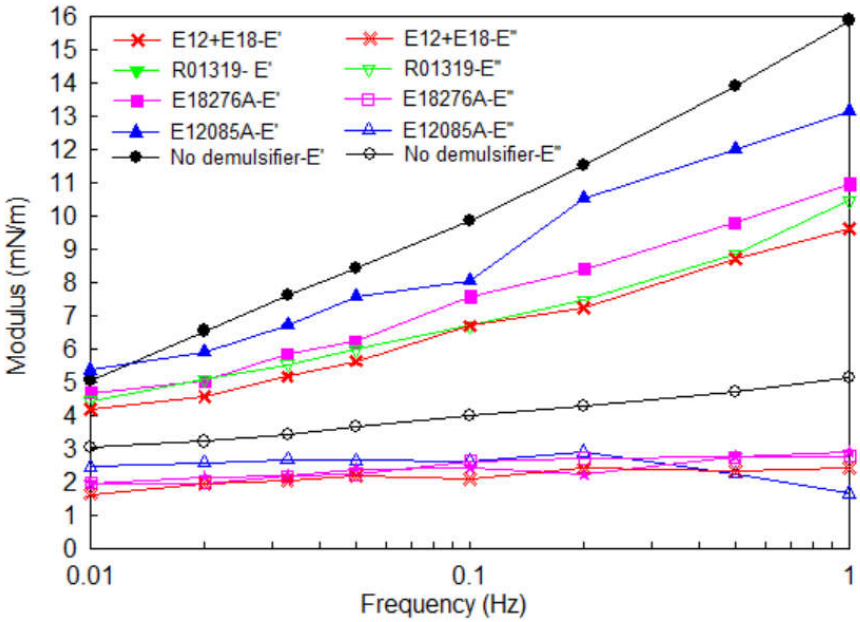

Figure 5.5.12: The interfacial dilational rheology after the addition of demulsifiers (both E′ and E″ are presented in the same graph), Chang et al. (2022).

Given the unconsolidated nature of the formation and the abundance of clays, the final set of experiments were conducted to investigate the influence of clays. Because, the fine clay particles and polymer molecules carried with the produced liquid could potentially affect the oil/water separation, which is one of the major added concerns for field engineers. Specifically, the experiments focused on the influence of clay type, clay concentration, polymer shearing status, and polymer concentration on the emulsification behavior of the produced liquid. All emulsions were 50% WC or 1:1 ANS oil and produced water ratio. The traditional bottle test method was replaced with an advanced equipment known as Turbiscan® Lab (Formulaction, France), to investigate the effect of various factors on emulsion stability. This particular instrument can characterize the destabilization process in the dispersed system based on multiple light scattering principle, the theory of which is described in Chang (2022). A parameter termed as Turbiscan Stability Index (TSI) can be defined to measure the stability of the scanned dispersed system, which compares every scan of a measurement to the previous one, as per a time based scheme, Chang (2022). The higher TSI value represents the lower emulsion stability, and vice-versa.

The temporal variation of TSI for the four tested clays at a fixed concentration of 0.1 wt% is shown in **Figure 5.5.13**. In each case, the TSI value of the emulsion increases with time, as would be expected, implying the decrease in the stability of the emulsion with extended time. The presence of clays relatively reduces the TSI value of the emulsion, resulting in enhanced emulsion stability. During the tests, we also noticed that when the clay is absent, a very loose o/w emulsion is formed right after homogenization and can easily separate into its individual phases with nearly complete separation. In contrast, a complex emulsion system is generated with the addition of clay particles, as shown in the inset of **Figure 5.5.13**. The complex emulsion system consists of the upper tight w/o

emulsion and the lower loose o/w emulsion. Undoubtedly, the tight w/o emulsion formed with the addition of clay resulted in the increased emulsion stability due to the high viscosity of the continuous heavy oil phase against phase separation. The formation of w/o emulsion with the addition of clay might be ascribed to the polar interactions between clay particles and polar heavy ends such as asphaltenes and resins in the crude oil (7.7% and 14.7% respectively in the oil, Chang (2022), making the hydrophilic clay particles more oil-wet (Buckley and Liu 1998; Hunter et al. 2008; Jeon and Hong 2014; Mironova and Ilyin 2018; Umar et al. 2018; Zhang et al. 2022). The direct evidence for the change in clay wettability is that no settlement of clay particles is noticed in the separated water phase. The emulsion stability from highest to lowest is listed as follows: Ca-montmorillonite > Na-montmorillonite > kaolinite > illite. The difference in emulsion stability with different clay types could be attributed to differences in the clay structures (Bergaya et al. 2006).

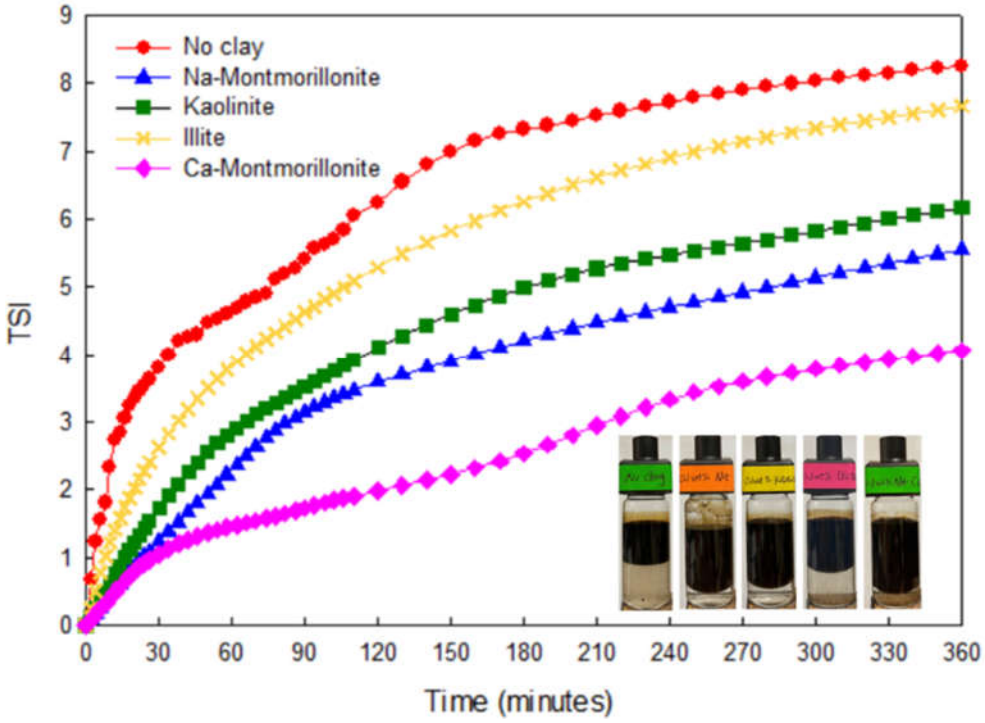

Figure 5.5.13: The effect of clay type on TSI values of emulsions at a fixed clay concentration of 0.1wt% in oil (0.05wt% in emulsion). Note clay is added to the oil phase and emulsion does not contain Flopaam, Chang (2022).

In a subsequent test, the effect of clay concentration on emulsion stability when clay was added to the oil phase, was studied using the TSI values of emulsions at 6 hours and visual observation on emulsion separation after 24 hours. At clay concentrations above 0.05 wt%, the TSI values noticeably descend with increasing clay concentration for all tested clay types, indicating that the emulsion stability increases with clay concentration. These results and the back scattering profiles of all the tests are described by Chang (2022). However, given the predominance of illite in the heavy oil reservoirs on Alaska North Slope (Jones 2010), much of the remaining tests that also included sheared and unsheared Flopaam, focused on illite. **Figure 5.5.14** compares the effect of polymer and fixed (0.25

wt%) illite concentration on the stability of emulsions for two scenarios of clay addition to oil and clay addition to the aqueous phase, respectively.

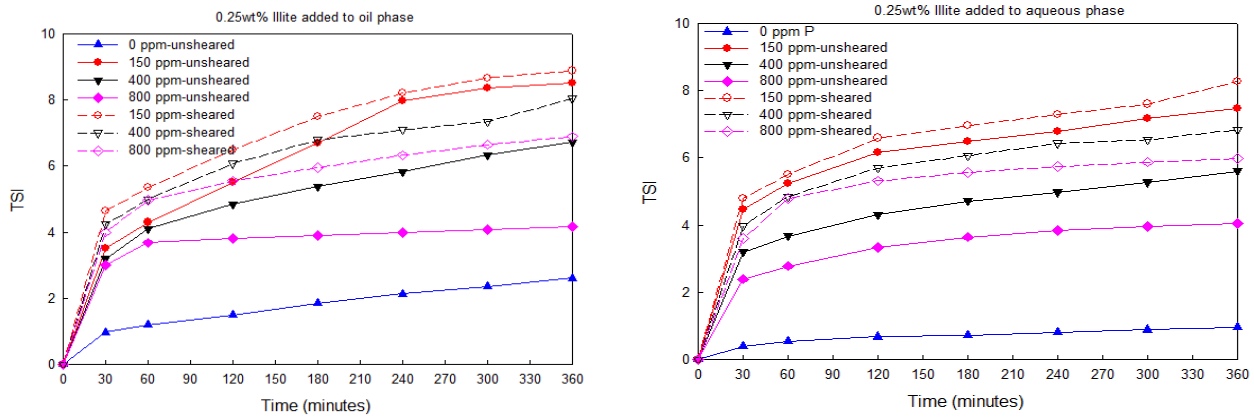

(a) illite added to the oil phase (b) illite added to the aqueous phase

Figure 5.5.14: The effect of Flopaam on the TSI of emulsions stabilized by illite addition to the oil and aqueous phases, respectively, Chang (2022).

As shown in **Figure 5.5.14**, whether the polymer is sheared or not, the presence of Flopaam in both cases of clay addition results in higher TSI values, meaning a considerable reduction in the emulsion stability. In both cases (unsheared/sheared polymer and clay additions), the TSI values decrease with increasing polymer concentration, implying that emulsion stability increases with increasing polymer concentration. The TSI of the emulsion with sheared polymer (all dashed curves) is higher than that with unsheared polymer at all tested polymer concentrations; although, the difference between $TSI_{sheared}$ and $TSI_{unsheared}$ gradually narrows with decreasing Flopaam concentration. Nevertheless, shearing results in lower emulsion stability at the same polymer concentrations. As far as the mode of clay addition is concerned, although the TSI values differ significantly in the absence of Flopaam, the emulsion stability in the presence of polymer appears to be somewhat independent as indicated by similar TSI values. This is also supported by the similarities in the visual observations in **Figure 5.5.15**.

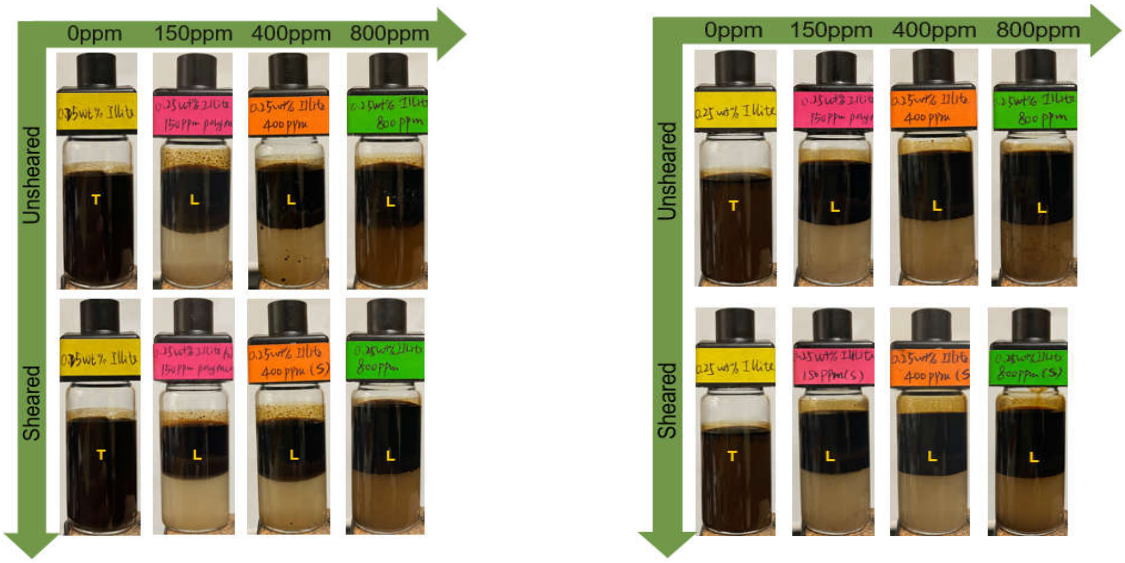

(a) illite added to the oil phase (b) illite added to the aqueous phase

Figure 5.5.15: Visual observation on emulsion separation after 24 hours for 0.25 wt% illite addition to the oil and aqueous phases, respectively, Chang (2022).

Given the emulsion characteristics discussed above, illite and sheared polymer were used to prepare the emulsions to further investigate the effect of polymer on emulsion stability at various clay concentrations. As shown in **Figure 5.5.16**, at relatively smaller clay concentration (circa region I), the presence of polymer lowers the TSI values in comparison to the no polymer case; however, this trend is significantly reversed with increasing clay concentration (circa region II). These results demonstrate that there is a synergistic effect between clay and polymer, influencing emulsion stability. It had been reported that anionic polymer could adsorb onto the clay particles by the hydrogen bonding between the nitrogen from the acrylamide group of the polymer and the deprotonated oxygen from the clay surface (Long et al. 2006; Nakatani et al. 2021; Quezada et al. 2021). At low surface coverage, the polymer-clay interaction could establish a bridging force, causing the formation of large clay aggregates and thus the flocculation. At high surface coverage, smaller clay aggregates are formed due to the repulsive force between the negative group of the adsorbed polymer around the clay particles. The surface coverage is affected by the clay and polymer properties and depends on the clay/polymer ratio, Chang (2022).

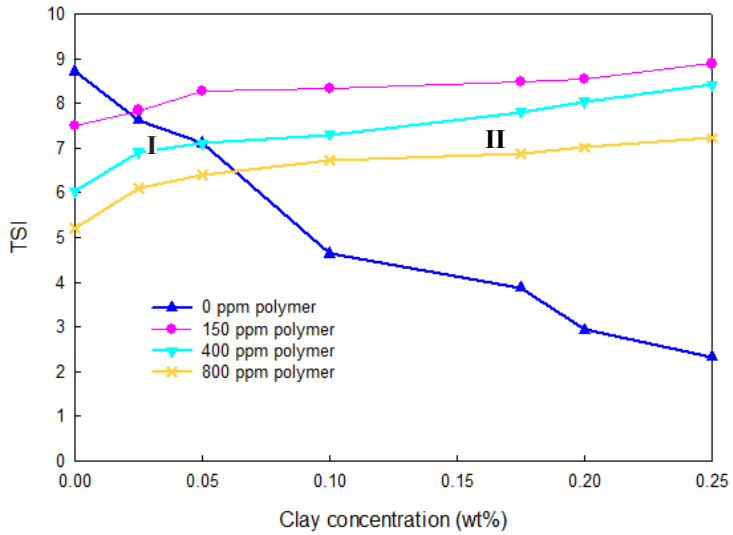

Figure 5.5.16: Synergistic effect of illite and sheared polymer on emulsion stability when illite was added to the oil phase, Chang (2022).

The final experiments reverted to the traditional bottle test methods to evaluate the effectiveness of a new emulsion breaker (DEPO11) in comparison to E12+E18. All tests included fixed illite concentration of 0.25 wt%, with and without Flopaam, at 50% WC. Qualification of the new emulsion breaker and E12+E18 (and additive) was mainly based on the performance criteria such as separation kinetics, BS&W and OIW. After the addition of 500 ppm demulsifiers, the water separation was recorded for 6 hours and the BS&W was measured after 24 hours to quantify the quality of the separated oil. The results for the test in the absence of polymer are shown in **Figure 5.5.17 (a)** and **(b)**, respectively. Clearly, from a separation efficiency standpoint, the performance of DEPO11 is much inferior; however, the clarity of the separated water is the best (see labeled middle tube in **Figure 5.5.17 b**) and the BS&W in the separated oil is relatively low (sediment 0.06% and water 1.42%). In contrast a 1:1 blend of E12+E18 and DEPO11 or simply a ternary blend of 25%E12+25%E18+50%DEPO11 is much more effective, resulting in a nearly 90% demulsification efficiency and the lowest BS&W (sediment 0.06% and water 0%); although the color of the separated water phase is not "water white" as is the case with DEPO11. The E12+E18 blend alone results in a comparable separation kinetics, but has the highest BS&W (sediment 0.06% and water 3.69%). Thus, E12+E18 and DEPO11 could work synergistically to improve the demulsification performance and could become the most applicable demulsifier for emulsions containing clay particles.

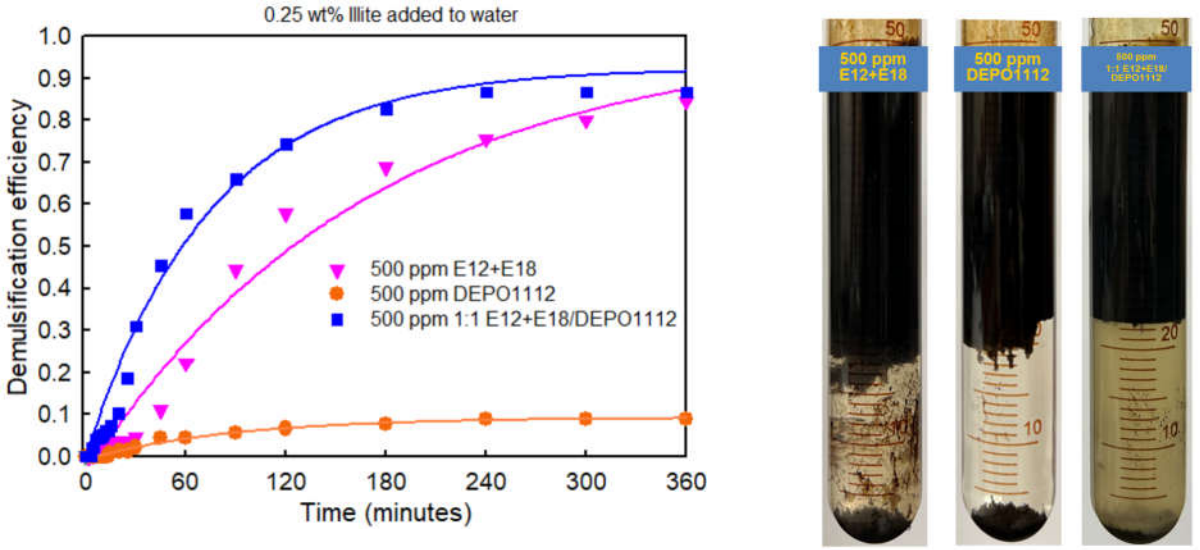

(a) separation kinetics in 6 hours (b) photos of final separation after 24 hours

Figure 5.5.17: The performance of demulsifiers for emulsion stabilized by 0.25wt% illite in the absence of polymer.

As mentioned earlier, the above experiments were also carried out in the presence of sheared polymer at a fixed concentration of 800 ppm. However, in this testing E12+E18 and the additive KCl was also evaluated, especially to compare the performance with the ternary blend of E12+E18+DEPO11. The dosage of E12+E18 varied from 0 to 100 ppm. It was observed that in all the tests, emulsions generated were very loose and tended to separate within 5 minutes. Due to the minor difference in separation speed, the separation kinetics are not included in the evaluation and only BS&W and OIW are used as the performance criteria to screen the most efficacious emulsion breaker. The results are plotted in a bar chart in **Figure 5.5.18**. Clearly, without any emulsion breaker, both the BS&W as well as OIW are the highest. The 50 ppm and 100 ppm dosage of E12+E18 does result in the reduction of BS&W and OIW accordingly; the values are still deemed high and unacceptable. Compared to E12+E18 alone, though DEPO11 has a better ability to reduce the solid and water content, the OIW is still relatively high. This was the primary reason the combinations of E12+E18 with DEPO11 and KCl were also evaluated from the standpoint of synergy. Even though a 1:1 combination of E12+E18 and DEPO11 reduces the BS&W, the OIW is still high and on the other hand, comparatively, adding 8,000 ppm KCl to E12+E18 proves to be much more effective in substantially reducing the BS&W and bringing the OIW to acceptable standards. Thus, the combination of E12+E18 and KCl becomes the most applicable demulsifier formula to treat the emulsion containing both polymer and clay particles.

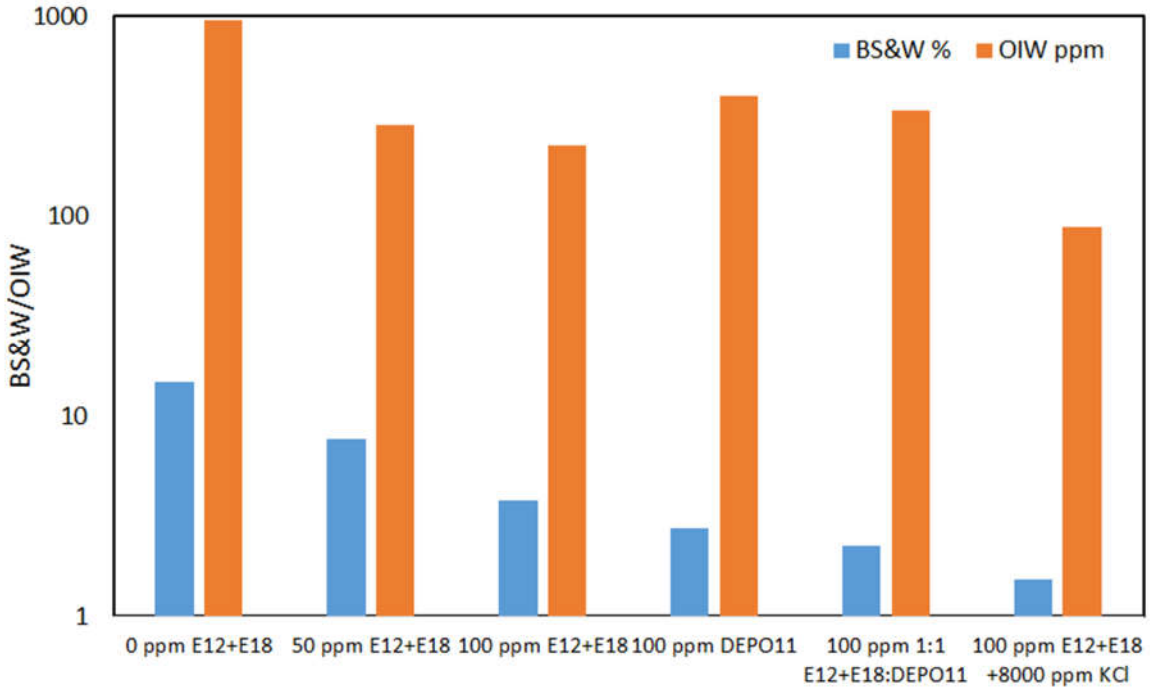

Figure 5.5.18: The performance of demulsifiers for emulsion stabilized by 0.25wt% illite in the presence of 800 ppm sheared polymer.

Main findings of practical significance

- Most importantly, one single emulsion breaker chemistry is inadequate in treating heavy oil emulsions, thus necessitating a combination with another emulsion breaker, and possibly an additive.
- IFT is not the determinant factor to the stability of the emulsion containing polymer.
- The narrow range of measured IFTs are independent of the polymer concentration, suggesting that polymer is not a surface active agent.
- In the absence of emulsion breaker, the oil-water separation efficiency and oil content in water is negatively impacted by increasing polymer concentration.
- All tested clay particles, whether they are added to oil or water, could convert the loose o/w emulsion to the tight w/o emulsion as clay concentration increases, eventually increasing the emulsion stability.
- At a fixed clay (illite) concentration, the presence of polymer (unsheared or sheared) remarkably reduces the emulsion stability.
- A composite emulsion breaker (E12+E18) and KCl result in superior demulsification performance at polymer concentrations as high as 800 ppm, which is based on the BS&W and oil content in separated water.

Topical publications

1) *H. Chang, Y. Zhang, A.Y. Dandekar, S. Ning, J.A. Barnes, W. Schulpen: Emulsification Characteristics and Electrolyte-optimized Demulsification of Produced Liquid from Polymer*

Flooding on Alaska North Slope. SPE Production & Operations February 2022.

2) *H. Chang, Y. Zhang, A.Y. Dandekar, S. Ning, J.A. Barnes, R. Edwards, W. Schulpen, D. Cercone, J. Ciferno: Experimental Investigation On Separation Behavior of Heavy Oil Emulsion for Polymer Flooding On Alaska North Slope. SPE Production & Operations Journal, June 2020.*

5.6 Polymer Fouling of Heater Tubes

In heavy oil production systems, owing to lower formation temperatures and oil densities closer to water, it is quite common to elevate the temperature of the produced stream for better separation of oil and water. A heater-treater system is currently in use at the Milne Point Unit central processing facility (CPF), where the commingled production from all the pads (including J-pad) is heated from 130^{o}F to 170^{o}F for better separation in a three phase separator. Clearly, achieving this degree of elevation in the process fluid temperature in any type of heat exchanger (fired tube etc.) requires what is known as high enough "skin" temperature (regardless of process fluid inside or outside) to effect the heat transfer. Although this can be typically optimized by a combination of low residence time–high skin temperature and vice–versa, a reasonably high enough skin temperature is nevertheless necessary to elevate the process fluid temperatures. This is precisely where the problem lies when it comes to the breakthrough polymer in the production stream in that the polymer when exposed to high temperatures will form a fairly solid deposit, that is not easy to mechanically remove, or "foul" the heating surface, thereby reducing the overall heat transfer coefficient. If the process fluid is flowing inside the tube, then the fouling will be inside and outside when the process fluid is outside. Therefore, similar to the emulsion issues discussed in the previous section, polymer induced fouling of heater tubes also can become a major bottleneck for an otherwise successful polymer flood. In order to address this concern, a systematic experimental fouling study to investigate the potential fouling problem at the CPF was undertaken to ensure overall success of the project. In particular, the objective was to identify the HPAM phase change temperature (also known as cloud point) and its spacing with respect to fouling propensity/severity so that a threshold or safe operating skin temperature guideline could be established. Accordingly, both static as well as dynamic fouling studies were conducted, which are detailed in the two topical publications, RPPRs and the MS thesis (Dhaliwal, 2021). However; included below is the design of experiments, key results summary and the main findings of practical significance.

Design of experiments

The experiments that were designed and conducted were planned in such a way that enabled qualitative as well as quantitative testing of a multitude of variables and scenarios such as induced fouling inside and outside, static vs. dynamic, residence time, skin temperature, polymer concentration and the heating surface metallurgy. The metric or performance indicators used in these tests included visual detection of cloud point, deposit/fouling rate based on mass balance and pressure drops to detect incipient fouling. Note that most of the tests were conducted in the absence of the oil phase – possibly mimicking the worst case scenario because it is believed that the oil present may actually be somewhat of a "lubricating film" that may minimize the deposition. **Table 5.6.1** provides a concise summary of all the experiments.

Table 5.6.1: Test matrix for fouling studies to identify threshold heater-treater operating temperature.

Parameters/Variables	Mechanisms	Test Fluids and Materials	Test Conditions	Screening Criteria/Evaluation of Results
• 100% WC • Less than 100% WC attempted • Synthetic formation brine TDS 26,840 ppm (pH 7.2) • Polymer concentration 0–800 ppm (unsheared) • Static test tubing OD of 0.25 inch and length of 6.5 inch. OD specified because fouling is outside • DSL tubing ID of 0.055 inch and loop length of 10.08 ft. ID specified because fouling is inside	• Phase change or cloud point • Morphology of deposit(s)	• DI water for synthetic brine preparation • Synthetic white oil of 20 cP viscosity – attempted • Reagent-grade NaCl; $NaHCO_3$; $CaCl_2$ • Flopaam 3630S of 18-20 million Dalton and 30% hydrolysis • Cu; CS and SS tubing	• Polymer mother solution diluted to desired concentrations • Skin temperature 165–350°F • Process fluid heated from 77–122°F • Cloud point measurement from 165–250°F • Fixed DSL flowrate of 3.94 mL/min to achieve a (field) residence time of 1.194 min	• Visual detection of cloud point • Mass balance • Deposit rate for static tests • XRD and ESEM • Pressure drop for dynamic tests

Summary of key results

In this section, as per the design of experiments in **Table 5.6.1**, first the fundamental phase change or cloud point measurements of the polymer solutions are presented. These are followed by the representative results that are primarily related to the static and dynamic fouling tests. Lastly, the calculated fouling factors are discussed.

Cloud point measurements of the prepared polymer solutions (0–800 ppm) were carried out through temperature scanning in the range of 165 to 250°F, as shown by the scheme in **Table 5.6.2**. The prepared solutions were placed in the special glass bottles, sealed using Teflon tape and then these bottles were placed in a preheated oven at 165°F and heated for 24 hours. Following this, the

containers were taken out for visual inspection of phase change, and subsequently, the oven temperature raised to the next temperature and the heating time repeated.

Table 5.6.2: Experimental scheme for cloud point measurements of polymer solutions.

Temperature (°F)	Heating Period	Duration of Heating (hours)
165	0-24	24
180	24-48	24
200	48-72	24
220	72-96	24
240	96-120	24
250	120-144	24

Figure 5.6.1 shows the state of the tested polymer solutions at four different temperatures. At 165°F and 220°F the solutions in the bottles are stable and have a clear appearance, similar to the fresh state, indicating no phase change. However, at 230°F the samples with polymer exhibit a milky/opaque appearance, which means that the cloud point is bracketed between 220 and 230°F, ultimately leading to a precipitation severity at 250°F. Our findings show that fluid temperature has a significant influence on the hydrolysis of the polymer, which is similar to that reported by Ryles (1988). Polymer hydrolysis increases at elevated fluid temperatures, which increases the carboxylate content in the solution, making the polymer prone to precipitation by combining with divalent Ca^{2+} cations from the brine. As will be shown later, the results of the cloud point tests are consistent with the findings from the deposit tests. At skin temperatures of 165 and 200°F (< cloud point) the fouling tendency is not severe, but an abrupt increase in deposit rate occurs when the tube skin temperature is 250°F (> cloud point), as the polymer hydrolyzes to a greater extent and combines with Ca^{2+} cations to precipitate and aggravate the fouling tendency on the heating tube.

(a) at 165°F

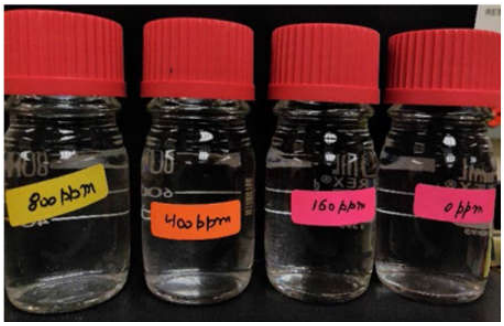

(b) at 220°F

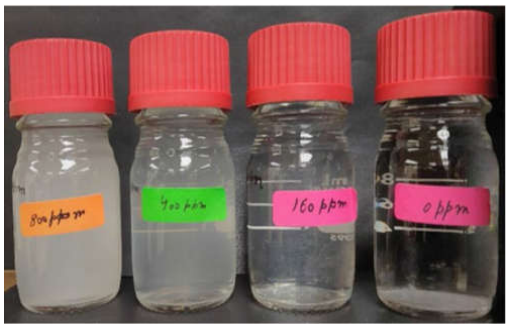

(c) at 230°F

(d) at 250°F

Figure 5.6.1: State of the polymer solutions after heating at the stated temperatures for 24 hours.

All static deposition tests were conducted on copper, carbon steel and stainless steel at 165, 200 and 250°F without polymer and at a concentration of 800 ppm. Using the indigenously designed and developed set-up, as described in Dhaliwal et al. (2022), the testing solution that is initially at 77°F is heated to 122°F by the internally circulated hot oil to mimic the inlet and outlet conditions in the heat exchanger. After reaching the desired testing solution temperature, it is replaced with a fresh batch and again heated to 122°F, but using the same U-tube. This sequence is repeated 5 times (named as 5 runs) and after the termination of the test, the cumulative deposit or fouling of the outside of the U-tube is quantified by mass balance and the solid deposit subjected to XRD and SEM analysis. The logic behind the repetitive testing lies in the fact that the same heat exchanger tubes (U-tube in this case) would be heating the continuously produced fluids stream (testing solution in this case). **Figure 5.6.2** shows the Effect of skin temperature, tube material, and polymer on deposit rate at 165°F, 200°F, and 250°F, respectively. The main objective of this study is to understand the fouling tendency in the heat exchanger if using different heating tube materials (i.e., copper, carbon steel, and stainless steel). Thus, the result is to help the operator to choose the proper tube material, if necessary, to prevent severe fouling issues in the heat exchanger in the future. As shown in **Figure 5.6.2**, by comparing the results of carbon and stainless steel, the deposit rate on stainless steel tube is less than carbon steel tube under the same test conditions. If we compare the copper tube and stainless steel tube results, the copper tube and stainless steel tube exhibit nearly similar deposit rates at the skin temperatures of 165 and 200°F, in the absence of the polymer. However, when polymer is present the stainless steel tube shows a fairly high deposit rate than copper at 165 and 200°F. The copper tube shows nearly equal deposit rates for 0 and 800 ppm polymer concentration when the skin temperatures are 165 and 200°F. At the skin temperature of 250°F (> cloud point), copper, carbon steel, and stainless steel tubes show similar deposit rates when no polymer is present. However, in the presence of polymer, deposit rates in carbon and stainless steel are comparable, and most importantly nearly half that of copper, at 250°F. Overall, fouling is a result of factors such as surface roughness and thermal conductivity; however, in the case of polymer solutions, cloud point is perhaps the most influential. Additional mechanisms have been discussed in Dhaliwal et al. (2022).

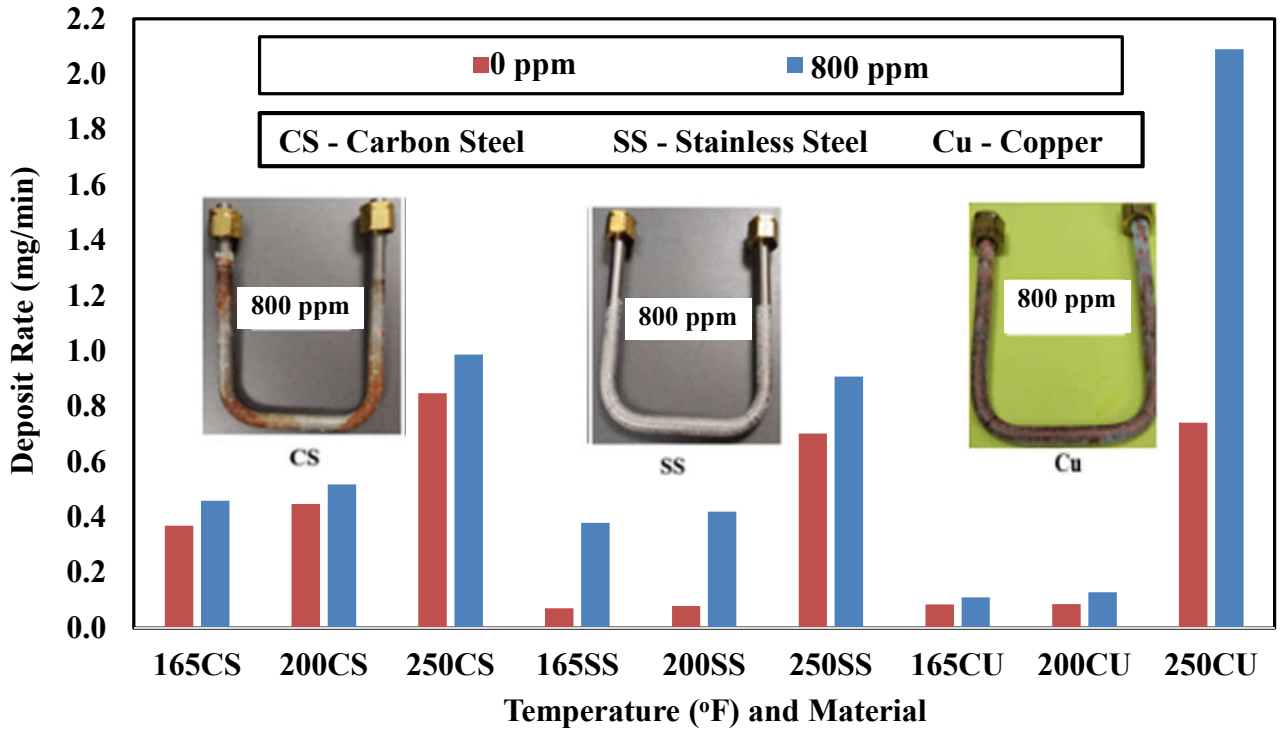

Figure 5.6.2: Deposit rate (cumulative deposit/total heating time) with and without polymer on tested tube materials at different skin temperatures.

The morphology and composition of the deposit at 350°F on copper tube was studied using, namely ESEM and XRD. Although due to the limitation of XRD, polymer fouling cannot be explicitly identified as diffraction peaks in the patterns. However, a comparison of XRD scans of the deposit with and without polymer can certainly reveal the subtleties and relative influence of polymer. Dhaliwal et al. (2021) showed that the most significant difference in the two XRD patterns occurs at the angle of approximately °2θ = 29 (represents the calcite peak). For e.g., the presence and absence of a peak at °2θ = 29, with 800 ppm polymer and without polymer, respectively, indicating that the presence of polymer in the solution may be conducive to the formation of one more type of calcite mineral scale. Besides, the noticeable background noise can be observed in the two patterns between the angles of °2θ = 15 and °2θ = 24, which may represent some byproducts resulting from the interaction between polymer and mineral salts. The ESEM images of the deposit or fouling generated with and without polymer were much more revealing in terms of the differences. As seen in **Figure 5.6.3 a**, the mineral crystals are irregular and naturally compact together, so the bonding between the mineral crystals is weak, and the mineral crystals generally appear to have less adhesion on the tube surface, which can explain why the pure mineral scale is brittle and easily scraped off (Dhaliwal et al., 2021). However, the presence of polymer clearly alters the overall deposit morphology, in that the deposit tends to bond to the mineral scale crystals forming a three-dimensional network structure, becoming denser with the increase in polymer concentration (**Figure 5.6.3 b**). In general, this kind of network structure of polymer-induced fouling is stronger than the simple compaction of the pure mineral scale, and it also has more adhesion to the tube surface, making it tougher and more

challenging for mechanical removal, Dhaliwal et al. (2021).

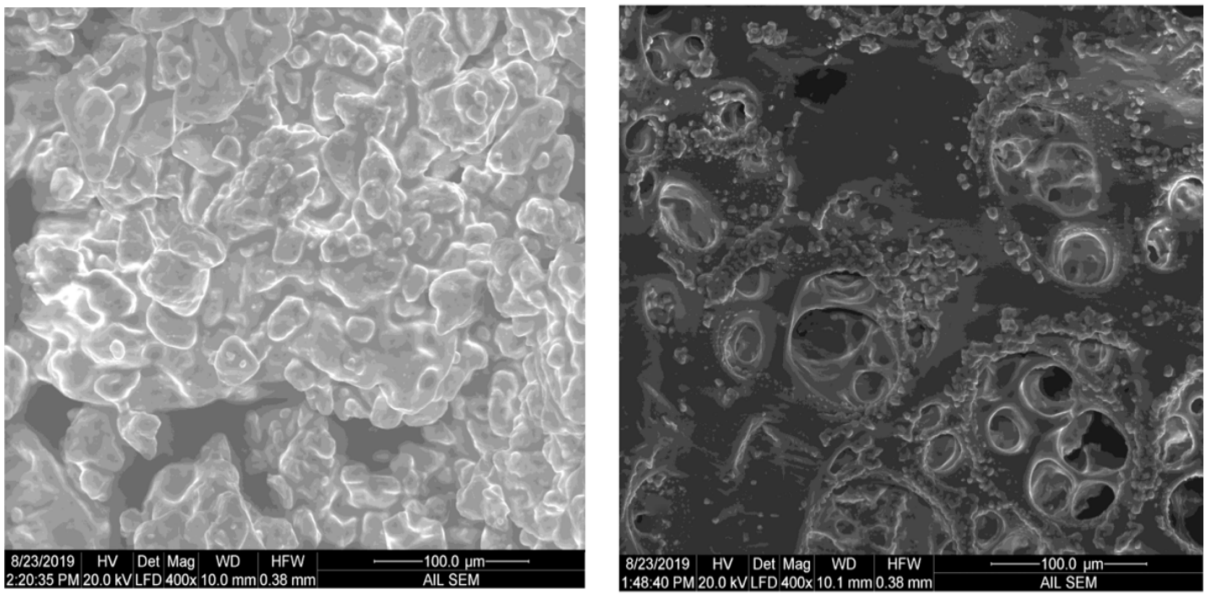

(a) Without polymer (b) 800 ppm polymer

Figure 5.6.3: ESEM pictures of fouling generated on the copper tube at a skin temperature of 350ºF, modified from Dhaliwal et al. (2021).

In the dynamic deposition tests, stainless steel was the only material tested at 165, 200, 250 and 350ºF, respectively without polymer and at a concentration of 400 ppm. In a flowing heat exchange system, the two operational parameters are namely the flow velocity and the residence time. Our indigenously designed and developed laboratory-scale flow loop (Dhaliwal et al., 2022), cannot concurrently satisfy both process parameters. However, we believe residence time is much more critical and rigorous, and accordingly, all the DSL tests have been designed and conducted to confirm the influence of skin temperature and the presence of polymer on fouling in heat exchangers under fixed residence time of 1.194 minutes. Note that this is the same as experienced by the produced fluids in the CPF heat exchangers. Thus, based on our experimental setup, a flow rate of 3.94 mL/min was determined to obtain the same residence time (1.194 minutes) for fluids as the field pilot. For the most part, all DSL tests qualitatively evaluate the fouling tendency based on the sudden and significant pressure drop across the flow loop under flowing conditions. Note that the pressure drops utilized in the fouling evaluation serve as qualitative indicators; vis-à-vis the absolute values are not of a particular consequence. In other words, a constant, flat pressure drop vs. sudden and significant spike in pressure drop, indicating no blockage and blockage owing to fouling, respectively.

Although the primary goal was to experimentally determine the fouling due to polymer, for a baseline comparison and to assess the proper operability of the DSL, some tests were carried out without polymer. **Figure 5.6.4** shows the pressure drop vs. time for the tests conducted at the skin temperatures of 165ºF and 350ºF, respectively. As seen in **Figure 5.6.4**, the differential pressure across the tube was almost constant for the entire 4-hour duration of the test, indicating no deposit or

fouling.

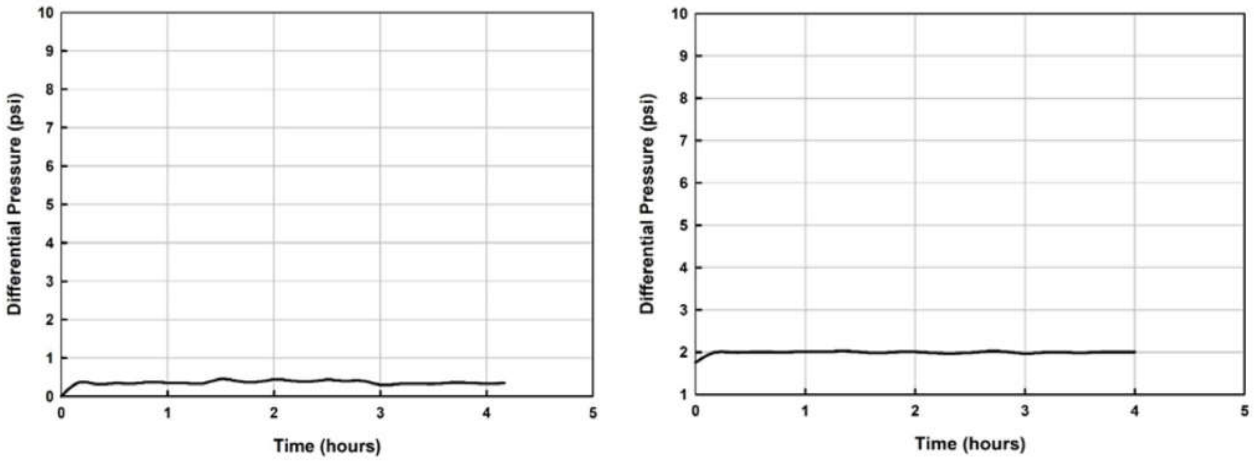

(a) 165°F (b) 350°F

Figure 5.6.4: Differential pressure data for the tested temperatures without polymer, Dhaliwal et al. (2022).

Based on the raw differential pressure vs. test duration data for the DSL results (Dhaliwal et al., 2022) at two temperatures below and above the cloud point, respectively, at a polymer concentration of 400 ppm, a composite plot is prepared as shown in **Figure 5.6.5**. As seen in the plot, the pressure drops vs. test or flow duration at 165°F and 200°F is fairly flat indicating that at these temperatures, basically there appears to be no blocking vis-à-vis fouling. However, the notable spikes in the pressure drop at 250°F and 350°F clearly demonstrate blockage due to fouling; note that this occurs much earlier, i.e., 68 hours@350°F, compared with 178 hours@250°F. The polymer solution cloud points and the associated phase change measurements discussed earlier corroborate the static as well as dynamic fouling data.

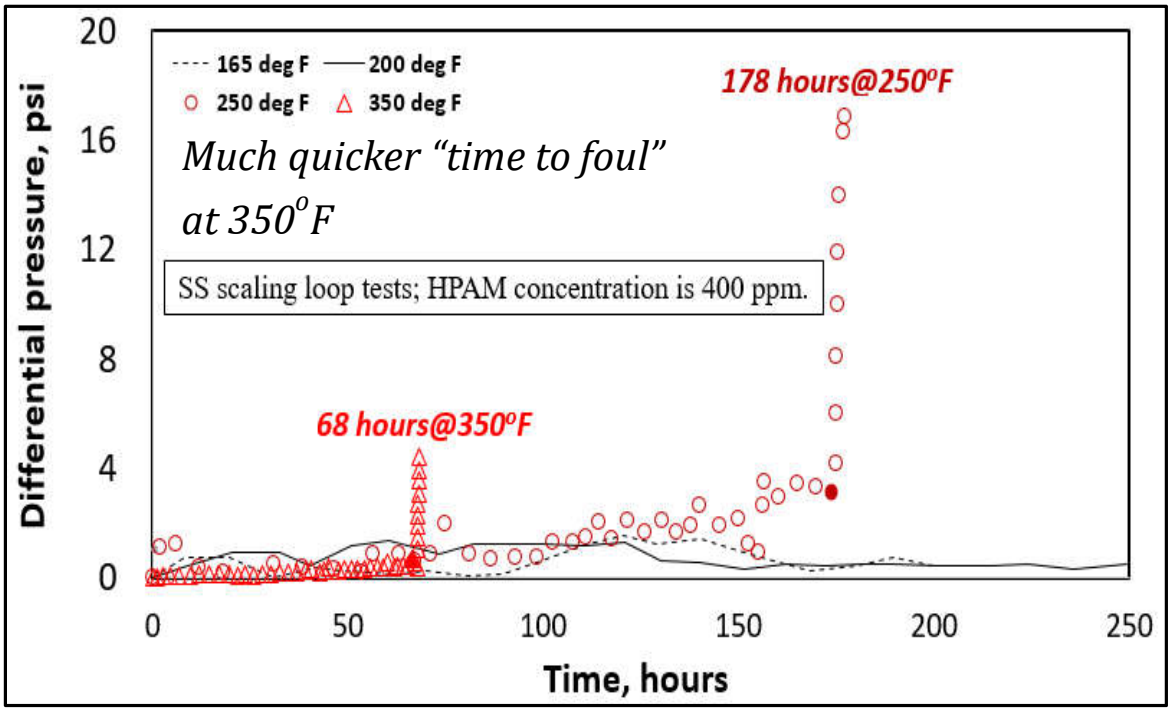

Figure 5.6.5: Differential pressure vs. test or flow duration in the DSL experiments conducted in stainless steel tubes at a polymer concentration of 400 ppm (modified from Dandekar et al., 2021).

Recall that our fouling tests have been conducted without the presence of oil – which certainly is an unknown in that the oil present may actually be somewhat of a "lubricating film" that may minimize the deposition. Considering the use of high temperatures and the volatility (safety issue) of the real oil, DSL experiments using a synthetic low flash point high viscosity mineral oil were conducted. However, these experiments had to be aborted after several attempts (tested up to a very high WC) due to the formation of strong (highly viscous) emulsions that lead to the circulation pump reaching the "over pressure" mode rather quickly. After reviewing the previous data from DSL experiments, we believe that maintaining the heater-treater skin temperature less than 250°F is a good conservative guideline.

The static and dynamic deposition data was also used in the estimation of what is known as 'fouling factor", which is denoted by R_f and defined as $(1/U_f) - (1/U_c)$, where U_f and U_c are the overall heat transfer coefficients under fouling and clean conditions, respectively. U_c values for single tubes can be easily computed based on the tube ID (D_i), OD (D_o) and the thermal conductivity (k_t) of tube material,

$$U_c = \frac{2k_t}{D_i Ln\left(\frac{D_o}{D_i}\right)} \qquad (5.6.1)$$

The thermal conductivities of Cu, CS and SS used in the fouling factor calculations are 386; 45 and 20 W/m/K (Dhaliwal et al., 2022); consequently, the U_c values calculated based on the IDs (in m) are in W/m^2/K. Calculation of U_f values, however, requires **Equation 5.6.1** to be re-written in a series form to account for the deposit layer (see **Figure 5.6.6**). **Equation 5.6.2** is mathematically consistent, in that; in the absence of fouling or deposit the second term in the denominator will be zero such that $U_f = U_c$, whereas the formation of deposit will result in a non-zero value of this second term, i.e., $U_f < U_c$.

$$U_f = \frac{2}{\frac{D_i Ln(D_o/D_i)}{k_t} + \frac{D_o Ln(D_d/D_o)}{k_d}} \tag{5.6.2}$$

(a) Static tests on Cu, CS, SS, (process fluid) deposit on outside

(b) Dynamic tests in SS, (process fluid) deposit inside

Figure 5.6.6: Schematic illustration of fouling or deposit in the static and dynamic tests used in R_f estimations.

The mass of the deposit and the pressure drop were used in the estimation of deposit thicknesses (and thus D_d) for the static and dynamic cases, respectively. Note that in the case of 165°F and 200°F, the deposit thickness is considered as zero given the constant pressure drop (**Figure 5.6.5**). In the calculations of U_f and subsequently R_f, a thermal conductivity (k_d) of 0.5 W/m/K was assumed for the polymer deposit. This is a reasonable approximation given the ~0.25–0.75 W/m/K thermal conductivities of (similar) polymeric materials typically employed as insulators in offshore flowlines. The temporal evolution of fouling factors based on the static experiments and single values of fouling factors from the DSL experiments are shown in **Figure 5.6.7**. The rapid rise in the fouling factors and continually increasing trend with the elapsed time for all the tested tube materials is readily apparent in the static case, and similarly a high value of fouling factor for the dynamic case. The differences between the two fouling factor plots should be noted though, that is the polymer concentration and the heating time/flow duration (the point at which the ΔP spikes). Although the static and dynamic fouling factors are not directly comparable, if the static SS data were to be extrapolated to a duration as long as 178 hours, with consideration for the different polymer concentrations, then the fouling factors would likely be within a similar order of magnitude.

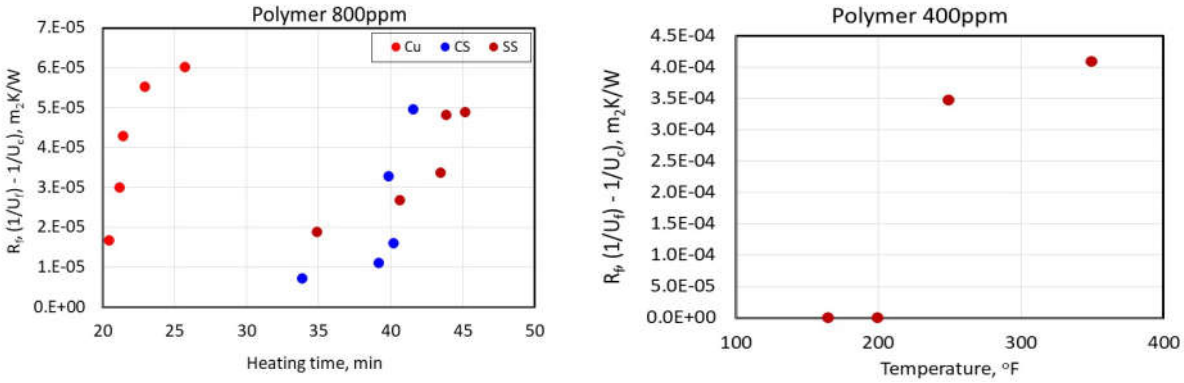

(a) Static tests on Cu, CS, SS at 250°F; deposit outside

(b) Dynamic tests on SS; deposit inside

Figure 5.6.7: Estimated fouling factors for static and dynamic cases.

Main findings of practical significance

- HPAM cloud point is 230°F, which is the "threshold" skin temperature.
- The cloud point corroborates with the static fouling tests as well as the dynamic scaling loop tests.
- The polymer deposit is akin to a molten plastic that bonds to the metal and thus not amenable to any mechanical intervention like the metallic scrubbing brushes that are typically used in cleaning the heat exchanger tube inside.
- So what does this mean from an operational standpoint? If the skin temperature exceeds the cloud point then the pressure drop will instantaneously increase (process fluid inside, and thus deposit inside) after a short period - somewhat akin to what would be the case with hydrate blockage.
- Consequences of a blocked heat exchanger tube such as this are obvious, i.e., flow as well as heat transfer (significant drop in U value) impeded!
- Lower skin temperature is a caveat, vis-à-vis somewhat of a trade off or compromise in that if the skin temperature is low then longer to heat from 70–110°F but the tubes are safe and vice-versa.
- HPAM fouling is unavoidable or "unstoppable", which means there is no known "inhibitor" for the current conditions that can prevent this or elevate the cloud point. ATBS polymer supposedly has an elevated cloud point (Personal communication with Director R&D, SNF).

Topical publications

1) *Dhaliwal, Y. Zhang, A.Y. Dandekar, S. Ning, J.A. Barnes, W. Schulpen: Experimental Investigation of Polymer-induced Fouling of Heater Tubes in the First-ever Polymer Flood on Alaska North Slope – Part II SPE Production & Operations. Accepted for publication in SPE Production & Operations, March 14, 2022.*
2) *Dhaliwal, Y. Zhang, A.Y. Dandekar, S. Ning, J.A. Barnes, R. Edwards, W. Schulpen, Cercone, D. and J. Ciferno: Experimental Investigation of Polymer Induced Fouling of Heater Tubes in The First Ever Polymer Flood Pilot On Alaska North Slope. SPE Production & Operations February 2021.*

5.7 Feasibility of Commercial Application of the Proposed Advanced Polymer Flooding in ANS Heavy Oil Reservoirs

As described in **Section 5.3**, a reservoir simulation model was constructed and calibrated to predict the oil recovery of the field pilot which demonstrated that polymer flooding is indeed technically feasible to significantly improve the heavy oil recovery on the Alaska North Slope. However, the economic performance of the pilot, critical to determining its success, is another key metric used in assessing the overall performance of the field pilot. Accordingly, this last task focused on evaluating the project's economic performance by integrating the calibrated simulation model with an economic model. Basically, three different history-matched models, namely the Full Model, Model A, and Model B (see **Section 5.3** for details) were employed in the economic analysis of polymer flooding incremental to waterflooding. Note that each of these three models had three different cases of (1) best history-matched model (P_{best}); (2) most optimistic (P_{high}) and (3) most pessimistic (P_{low}). Subsequently, the "best-matched Full Model", which is intermediate between Model A and B, respectively, was used (as a base case) in the economic and design sensitivity analysis to provide recommendations for continued operation of the ongoing field pilot and future polymer flood designs. This task provides important insight for the broader discussion of polymer flood design from the economic perspective. Details are included in the topical publication, RPPRs and the MS thesis (Keith, 2022). However; included below is the design of simulation cases, key results summary and the main findings of practical significance.

Design of economic analysis cases

The various numerical reservoir simulation models obtained by history matching that are described in **Section 5.3** segue into the economic analysis evaluation. For this purpose, the following matrix as shown in **Table 5.7.1** was utilized. The incorporation of various economic and sensitivity parameters in conjunction with the performance indicators enabled the determination of economic feasibility of the polymer field pilot.

Table 5.7.1: Simulation matrix for economic evaluation of polymer flood pilot.

Reservoir Simulation Models (see Section 5.3)	**History Matching**	**Economic Parameters**	**Sensitivity Parameters**	**Performance Indicators**
• Model A • Model B	• History matched through mid-2019 • History matched through mid-2020	• Polymer utilization factor • Oil price (also used in sensitivity of base case) • Polymer facilities (also used in sensitivity of base	• Injected polymer concentration – varied from 300 ppm to 2700 ppm in 300 ppm increments • Throughput rate – total pattern injection and	• NPV • Discounted PI ratio • Development cost

• Full model (also referred to as base model)	• History matched through start of 2022 (subjected to economic sensitivity)	case) • Surveillance and maintenance (also used in sensitivity of base case) • Revenue • OPEX • CAPEX • BTCF	production target rate varied between 1000 and 4000 barrels per day (BPD) • Polymer injection duration – 10 year spacing for switch from polymer to waterflooding • Polymer injection start time – polymer and waterflooding only; switch to polymer flooding after 0.5; 1; 2; 3; 4 and 5 years of waterflooding • Well spacing – 500 ft, 800 ft, 1000 ft, and 1500 ft	

Summary of key results

The oil recovery forecasts out to year 2050 produced by Model A, Model B, the Full Model, and waterflooding resulted in a range of recoveries as follows, 32-34%; 38-42%; 34-36% and 19-21%, respectively (Keith, 2022). Note that this range is a result of the most pessimistic to the best history matched models (see details in **Section 5.3**). Consequently, as expected, the polymer utilization factor for all three models is inversely proportional to the recovery. The economic performance (incremental to waterflood) for the best history-matched, most optimistic, and the most pessimistic Model A, Model B and Full Model, is tabulated in Keith (2022). A bar chart prepared from this table shown in **Figure 5.7.1** serves as a ready reckoner of economic performance, in that Model A produces the most pessimistic results, Model B is the most optimistic, and the Full Model is intermediate Note that a higher NPV (**Equation 5.7.1**) indicates a greater project value while a higher discounted PI ratio (**Equation 5.7.2**) and low development cost (**Equation 5.7.3**) indicate a more efficient investment. The best-matched Full Model simulation, hereafter referred to as the base polymer forecast, predicts that the polymer flood pilot will generate a present value of about $42.9 million during the whole project life. In addition, each dollar invested yields $5.05, and each barrel of oil produced over the project duration costs about $8.35 (additional or incremental by using polymer) to produce.

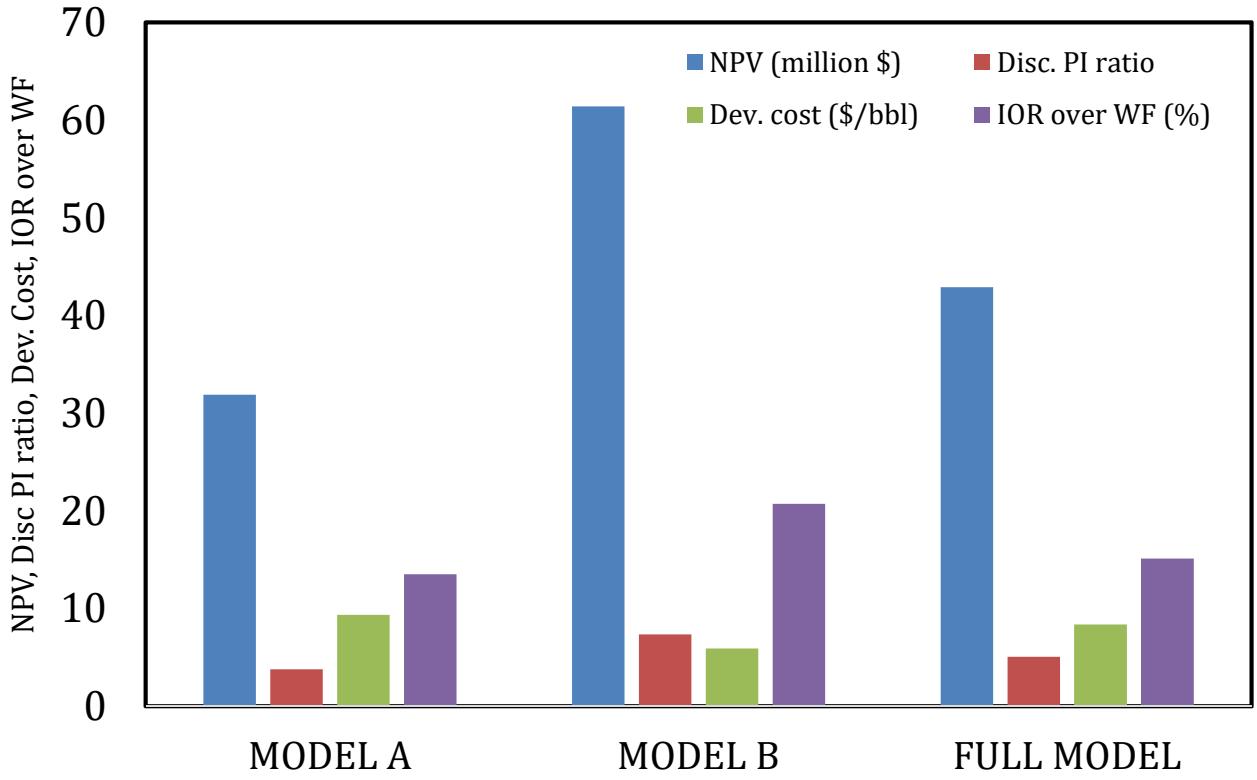

Figure 5.7.1: Comparison of economic performance of polymer flooding incremental to waterflooding for the three history matched models (data shown is for P_{best}; P_{low} and P_{high} are tabulated in Keith et al., 2022).

The NPV, discounted PI ratio and the development cost, respectively are calculated from the following three equations (Keith, 2022),

$$NPV = \sum_{n=0}^{N} BTCF_n * \left(\frac{1}{1+\frac{i}{12}}\right)^n \tag{5.7.1}$$

$$PI\ Ratio = \frac{NPV}{\sum_{n=0}^{N} OPEX_n * \left(\frac{1}{1+\frac{i}{12}}\right)^n + CAPEX_n} \tag{5.7.2}$$

$$Dev.Cost = \frac{\sum_{n=0}^{N} OPEX_n + CAPEX_n}{\sum_{n=0}^{N} V_{o,p,n} - V_{o,w,n}} \tag{5.7.3}$$

where i is the discount rate per annum; N is the maximum number of prediction months, $BTCF$ is before tax cash flow, $OPEX$ and $CAPEX$ are operating and capital expenditures and $V_{o,p,n}$ and $V_{o,w,n}$ is the volume of oil produced under polymer flooding and waterflooding, respectively for month n.

The base-matched Full Model polymer forecast was subjected to an economic parameter sensitivity test that included the oil price; polymer cost and the facilities cost. Three different values were considered for each of the economic parameters, namely a base value; conservative value and optimistic value. In the case of oil price these were $40; $20 and $80 per bbl, $1.50; $2 and $1 per pound for polymer acquisition and transport and for polymer facility acquisition and installation $3 million; $4 million and $2 million, respectively. **Figure 5.7.2** depicts the influence of the aforementioned economic parameters as a percent deviation from the NPV estimated for the base case ($42.9 million, see **Figure 5.7.1**). Clearly, as would be expected, oil price is the most sensitive (and uncertain as well) parameter, whereas the NPV hardly fluctuates with the polymer and facility cost, thus indicating that inaccuracies in our estimates of these costs may not have a significant influence on our comparative economic analysis.

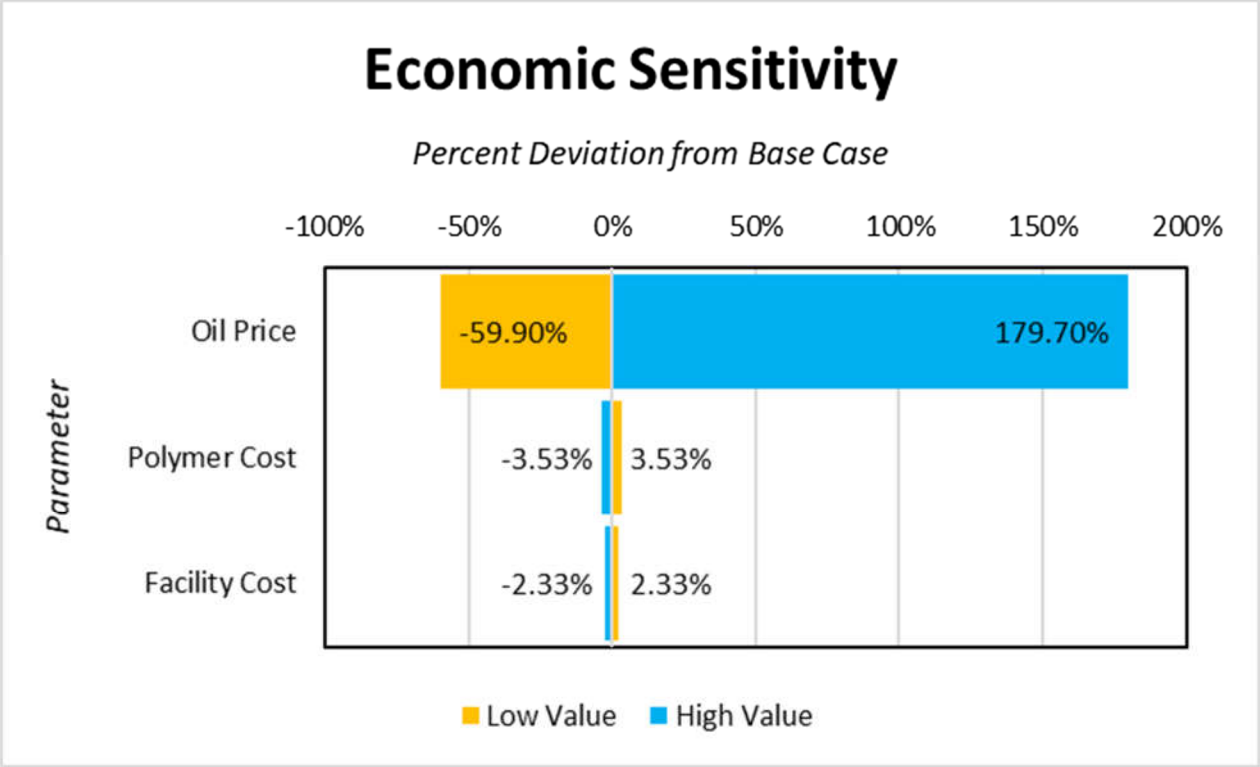

Figure 5.7.2: Tornado chart comparing the influence of economic parameters on the NPV, Keith (2022).

Finally, a sensitivity analysis with regard to five design parameters is conducted to optimize the current polymer flood pilot as well as provide guidance for future polymer flood projects. As stated before, the best-matched Full Model is employed to generate production forecasts for these varying design parameters, and the incremental economic modeling tool is used to determine the economic implication of varying these parameters. As shown in **Table 5.7.1**, the tested design parameters and their ranges include the following (1) injected polymer concentration; (2) throughput rate (3) polymer injection duration; (4) polymer flood start time and (5) well spacing. The results of the design

sensitivity analysis are summarized in **Table 5.7.2** and the NPVs of the different cases is depicted in a collection in **Figure 5.7.3**. Other detailed plots are in Keith (2022).

Table 5.7.2: Summary results of design sensitivity analysis.

Sensitivity parameter	**Outcome**	**Impact on NPV**
Injected polymer concentration	• Polymer superior to waterflood in terms of recoveries. • No benefit beyond threshold polymer concentration of 2100 ppm due to reduced injectivity. • In earlier times, increasing the polymer concentration increases the polymer utilization (up to 1800 ppm). • Reduced injectivity at very high polymer concentrations results in lower polymer utilization.	Incremental NPV directly proportional to injected polymer concentration, peaking at 2100 ppm.
Throughput rate	• Throughput rate is directly proportional to oil recovery. • BHP constraints encountered above 3500 BPD. • Very marginal improvement from 3500 to 4000 BPD.	Incremental NPV directly proportional to throughput rate, peaking at 3500 BPD.
Polymer injection duration	• Switch from polymer flooding to waterflooding dampens the recovery factor substantially. • The minimum point-forward polymer utilization [$PFPU = \frac{M_{p,y+\Delta y} - M_{p,y}}{V_{o,y+\Delta y} - V_{o,y}}$, where M_p and V_o are mass of polymer injected and oil volume produced, respectively; y represents the year to switch back to waterflooding and Δy is the considered duration of additional polymer injection in years] is directly proportional to year for switch to water injection.	N/A

	• For e.g., switch to waterflooding as early as 2025 results in 1.5 lb of polymer to produce an additional bbl of oil vs. 6 lb for a switch as late as 2050.	
Polymer injection start time	• For the first 5 months, waterflooding is capable of achieving higher oil rates than the polymer flood since higher throughput rates are possible with the improved injectivity of water. This is followed by a rapid decline in oil rate due to viscous fingering effects. • Polymer flooding implemented after a waterflood results in oil rate increase and then stabilizes for about 2 – 4 years before declining. • The duration of the stabilized oil rate period increases for earlier polymer flood start-times. • The decline in oil rate during polymer flooding is much more gradual than during waterflooding, even with the fracturing event occurring.	Expected ultimate recovery (EUR) factors converge to ~33% by 2050, for all polymer cases; however, earlier polymer injection start time is beneficial from the NPV standpoint (higher sustained oil rates sooner for longer duration).
Well spacing	• Irrespective of the flooding method (water vs. polymer), EUR is inversely proportional to well spacing. • Polymer flooding is relatively much more sensitive to well spacing since increasing the well spacing decreases the inter-well pressure gradient and dramatically reduces the injectivity. Nevertheless, polymer flooding is superior to waterflooding within the tested bounds. • Polymer utilization shows a "✓" shaped curve for all the tested spacing and the minima (more efficient	• The incremental NPV for polymer flooding over waterflooding vs. well spacing trend is very similar to the incremental EUR. • Overall, for reasonable well spacing, we would generally expect tighter spacing to yield improved economic performance for the polymer flood.

	polymer flood) in polymer utilization occurs much earlier for shorter well spacing. However, at later times, larger well spacing leads to lower polymer utilization values, likely due to additional oil volume contained within the larger spacing provides greater benefit for the extended polymer injection.	

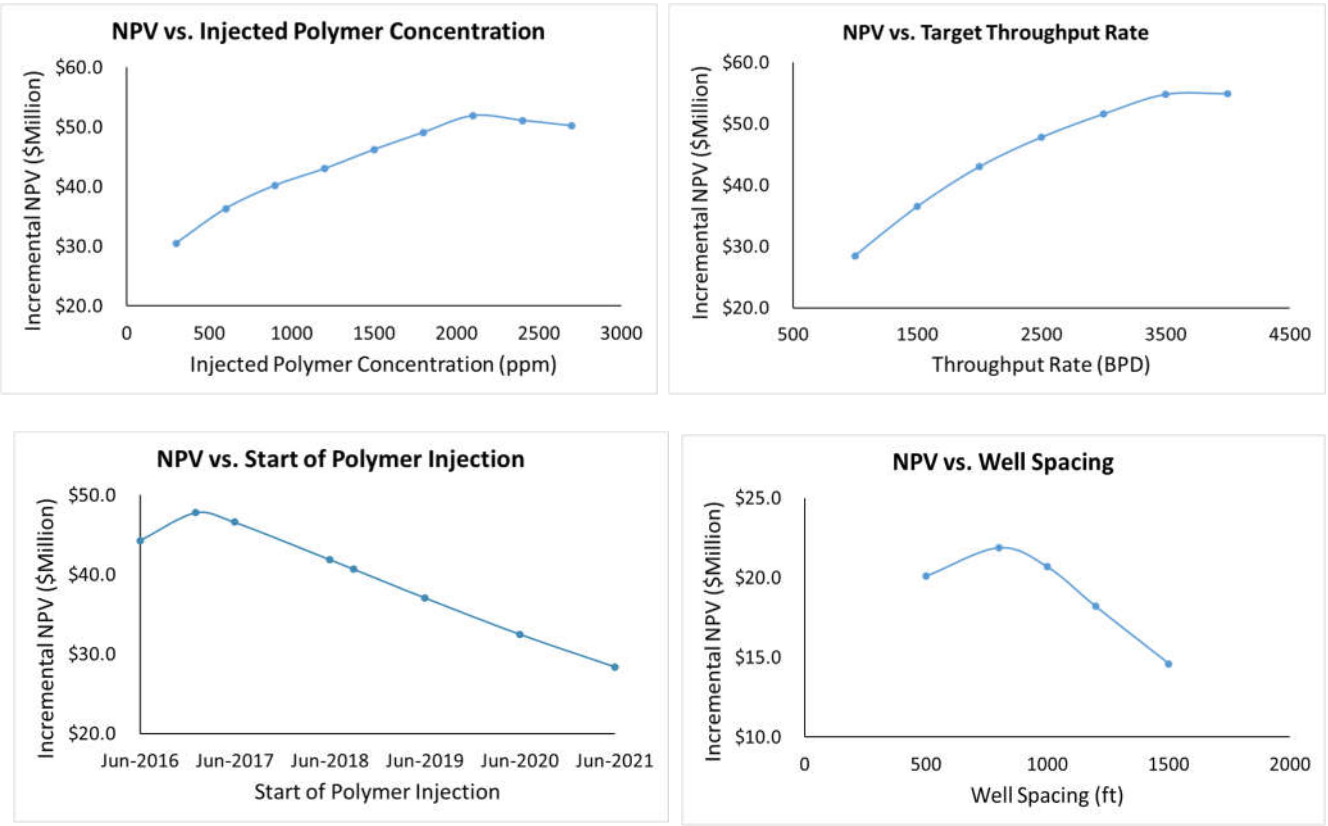

Figure 5.7.3: Incremental NPV comparison of sensitivity cases.

Main findings of practical significance

- The first ever polymer flood field pilot to enhance the recovery of heavy oils is economically beneficial, with all calibrated simulation models remaining robustly profitable in a range of conservative economic scenarios.
- A representatively calibrated simulation model is a pre-requisite for accurately capturing the full benefit of an EOR strategy such as polymer flooding, in the resulting economic evaluation.
- Within limits of injectivity and other operational constraints, increasing the injected polymer concentration and throughput can increase the oil recovery and thus improve project economics.

University of Alaska Fairbanks

- There is little benefit in switching from a polymer flood back to a waterflood for the pattern considered.
- The sustainability of polymer flooding depends on the prevailing economic conditions of the time, but this decision can be informed by efficiency measures such as the proposed point-forward polymer utilization.

Topical publications

1) *Keith, C.D., Wang, X., Zhang, Y., Dandekar, A. and Ning, S.: Economic Evaluation of Polymer Flood Field Test in Heavy Oil Reservoir on Alaska North Slope, SPE-210000-MS, SPE Annual Technical Conference and Exhibition 3-5 October 2022.*

6. Dissemination of Results and Engaging Communities of Interest

Publications have been the hallmark of the success of this team effort with **12** peer reviewed journal articles and **18** conference papers on diverse technical aspects of the polymer pilot. Heavy Oil Polymer EOR in the Challenging Alaskan Arctic - It Works! A paper presented at the 2021 URTeC (paper # 5077) was selected as "The Best of URTeC" for a special session in April 2022 Tulsa IOR meeting. In addition, there have been **7** press releases (media) associated with the project. The project also has produced **7** MS and PhD theses. All these have been cataloged in the OSTI database (www.OSTI.gov). Citations of publications resulting from the project are listed below:

Refereed Journals

1. Wang Dongmei, Shane Namie, Randall Seright, "Pressure Modification or Barrier Issues during Polymer Flooding Enhanced Oil Recovery", Geofluids, vol. 2022, Article ID 6740531, 15 pages, 2022. https://doi.org/10.1155/2022/6740531
2. A. Dhaliwal, Y. Zhang, A.Y. Dandekar, S. Ning, J.A. Barnes, W. Schulpen: Experimental Investigation of Polymer-induced Fouling of Heater Tubes in the First-ever Polymer Flood on Alaska North Slope – Part II. SPE Production & Operations, March 14, 2022. https://doi.org/10.2118/209800-PA
3. Seright, R.S. Wang, D. 2022. Polymer Retention "Tailing" Phenomenon Associated with the Milne Point Polymer Flood. SPE Journal 27. https://10.2118/209354-PA
4. Zhao, Y., Wei, M., Leng, L., Bai, B. Propagation of swellable microgels through superpermeable channels: impact of particle–pore matching size relationship, Energy & Fuels 2021, 35, 22, 18533–18542. https://doi.org/10.1021/acs.energyfuels.1c03030
5. Zhao, Y., Bai, B., Selective penetration behavior of microgels in superpermeable channels and reservoir matrices, JPSE 210 (2022), 109897. https://doi.org/10.1016/j.petrol.2021.109897
6. Zhao, Y, and Bai, B. "Experimental Study of Transport Behavior of Swellable Microgel Particles in Superpermeable Channels for Conformance Control." SPE J. 27 (2022): 790–805. doi: https://doi.org/10.2118/208576-PA
7. H. Chang, Y. Zhang, A.Y. Dandekar, S. Ning, J.A. Barnes, W. Schulpen: Emulsification Characteristics and Electrolyte-optimized Demulsification of Produced Liquid from Polymer Flooding on Alaska North Slope. SPE Production & Operations February 2022. https://doi.org/10.2118/209213-PA

8. Zhao, Y., Leng, J., Lin, B., Wei, M., Bai, B. 2021. Experimental study of microgel conformance control treatment for a polymer flooding reservoir containing super-permeable channels. SPE Journal, April 2021. https://doi.org/10.2118/205486-PA
9. A. Dhaliwal, Y. Zhang, A.Y. Dandekar, S. Ning, J.A. Barnes, R. Edwards, W. Schulpen, Cercone, D. and J. Ciferno: Experimental Investigation of Polymer Induced Fouling of Heater Tubes in The First Ever Polymer Flood Pilot On Alaska North Slope. SPE Production & Operations February 2021. https://doi.org/10.2118/200463-PA
10. Zhao, Y., Yin, S., Seright, R. S., Ning, S., Zhang, Y., Bai, B. 2020. Enhancing Heavy Oil Recovery Efficiency by Combining Low Salinity Water and Polymer Flooding. SPE Journal, November 2020. https://doi.org/10.2118/204220-PA
11. H. Chang, Y. Zhang, A.Y. Dandekar, S. Ning, J.A. Barnes, R. Edwards, W. Schulpen, D. Cercone, J. Ciferno: Experimental Investigation On Separation Behavior of Heavy Oil Emulsion for Polymer Flooding On Alaska North Slope. SPE Production & Operations Journal, June 2020. https://doi.org/10.2118/200369-PA
12. Wang, D., Li, C. and Seright, R.S.: Laboratory Evaluation of Polymer Retention in a Heavy Oil Sand for a Polymer Flooding Application on Alaska's North Slope, SPE Journal, February 2020. https://doi.org/10.2118/200428-PA

Conference Proceedings

1. Abhijit Dandekar, Baojun Bai, John Barnes, Dave Cercone, Jared Ciferno, Reid Edwards, Samson Ning, Randy Seright, Brent Sheets, Dongmei Wang, Yin Zhang, "The Success Story of First Ever Polymer Flood Field Pilot to Enhance the Recovery of Heavy Oils on Alaska's North Slope", SPE Western Regional Meeting, Anchorage, May 22-25, 2023. *(no DOI yet, but should be cataloged on www.onepetro.org when available).*
2. R.S. Seright, New Mexico Inst-Mining & Tech; D. Wang, University of North Dakota, "Impact of Salinity, Hardness, Lithology, And ATBS Content On HPAM Polymer Retention for The Milne Point Polymer Flood", SPE Western Regional Meeting, Anchorage, May 22-25, 2023. *(no DOI yet, but should be cataloged on www.onepetro.org when available).*
3. Keith, C.D., Wang, X., Zhang, Y., Dandekar, A. and Ning, S.: Economic Evaluation of Polymer Flood Field Test in Heavy Oil Reservoir on Alaska North Slope, SPE-210000-MS, SPE Annual Technical Conference and Exhibition 3-5 October 2022. *https://doi.org/10.2118/210000-MS.*
4. Keith, C.D., Wang, X., Zhang, Y., Dandekar, A., Ning, S. and Wang, D.: Polymer Flood Field Test Of Heavy Oil On Alaska North Slope Via Machine Assisted Reservoir Simulation, SPE-209443-MS, SPE IOR Conference, 25–29 April 2022. *https://doi.org/10.2118/209443-MS*
5. R.S. Seright and D. Wang: "Tailing" Phenomenon During Polymer Propagation at The Milne Point Polymer Flood, SPE-209354-MS, SPE Virtual Improved Oil Recovery Conference, 25–29 April 2022. *(cataloged as a journal paper on www.onepetro.org).*
6. D. Wang, S.S. Namie and R.S. Seright: Pressure Barrier Applicability To Polymer Flood Design, SPE- 209462-MS, SPE Virtual Improved Oil Recovery Conference, 25–29 April 2022. *https://doi.org/10.2118/209462-MS*
7. Namie, S., Wang, D., Yin, Z., Radu, G., Samson, N., Dandekar, A., Cercone, D., Ciferno, J., & Xindan, W. (2021). Challenge Solutions for a Significant Water Cut Reduction History Match on

Heavy Oil Polymer EOR. 82nd EAGE Annual Conference & Exhibition, 1–5. https://doi.org/10.3997/2214-4609.202113247.

8. Wang, X., Keith, C.D., Zhang, Y., Dandekar, A., Ning, S., Wang, D., Edwards, R., Barnes, J., Cercone, D.P. and Ciferno, J.P., History Matching and Performance Prediction of a Polymer Flood Pilot in Heavy Oil Reservoir on Alaska North Slope, SPE-206247-MS, SPE Annual Technical Conference and Exhibition, 21 - 23 September 2021 in Dubai, U.A.E. https://doi.org/10.2118/206247-MS
9. Jianqiao Leng, Mingzhen Wei, Baojun Bai, Randall S. Seright, Yin Zhang, David Cercone and Samson Ning. Impact of Rheology Models on Horizontal Well Polymer Flooding in a Heavy Oil Reservoir on Alaska North Slope: A Simulation Study, OTC-31087-MS, Offshore Technology Conference, Houston, TX, USA, 16 - 19 August 2021. https://doi.org/10.4043/31087-MS.
10. A. Dandekar, J. Barnes, D. Cercone, J. Ciferno, R. Edwards, S. Ning, W. Schulpen, R. Seright, B. Sheets, D. Wang, Y. Zhang: Heavy Oil Polymer EOR in the Challenging Alaskan Arctic – It Works! Unconventional Resources Technology Conference, 26-28 July 2021, Houston, TX, USA. https://doi.org/10.15530/urtec-2021-5077. ***Selected as the "Best of URTeC" for a special session at the April 2022, Tulsa IOR meeting.***
11. Abhijit Dandekar, Baojun Bai, John Barnes, Dave Cercone, Jared Ciferno, Reid Edwards, Samson Ning, Walbert Schulpen, Randy Seright, Brent Sheets, Dongmei Wang and Yin Zhang: First Ever Polymer Flood Field Pilot to Enhance the Recovery of Heavy Oils on Alaska's North Slope – Pushing Ahead One Year Later, SPE-200814-MS, SPE Western Regional Meeting, April 27-30, 2020, Bakersfield, California, USA. (actual published date April 2021, due to conference postponement). https://doi.org/10.2118/200814-MS
12. Samson Ning, John Barnes, Reid Edwards, Walbert Schulpen, Abhijit Dandekar, Yin Zhang, Dave Cercone, Jared Ciferno: First Ever Polymer Flood Field Pilot to Enhance the Recovery of Heavy Oils on Alaska North Slope – Producer Responses and Operational Lessons Learned. Virtually presented at the 2020 SPE ATCE, October 28, 2020. https://doi.org/10.2118/201279-MS
13. Samson Ning, John Barnes, Reid Edwards, Kyler Dunford, Abhijit Dandekar, Yin Zhang, Dave Cercone, Jared Ciferno: First Ever Polymer Flood Field Pilot to Enhance the Recovery of Heavy Oils on Alaska North Slope – Polymer Injection Performance, Unconventional Resources Technology Conference Denver, CO July 22-24, 2019. https://doi.org/10.15530/urtec-2019-643
14. Zhao, Y., Yin, S., Seright, S.R., Ning, S., Zhang, Y., Bai, B. 2020. Performance of Low Salinity Polymer Flood in Enhancing Heavy Oil Recovery on the Alaska North Slope. Paper URTeC1082 presented (virtually) at the Unconventional Resources Technology Conference, Austin, TX, USA, 20-22 July 2020. https://doi.org/10.15530/urtec-2020-1082
15. A. Dhaliwal, Y. Zhang, A.Y. Dandekar, S. Ning, J.A. Barnes, R. Edwards, W. Schulpen, C. David P, J. Ciferno: Experimental Investigation of Polymer Induced Fouling of Heater Tubes in The First Ever Polymer Flood Pilot On Alaska North Slope, SPE Improved Oil Recovery Conference, SPE-200463-MS, 18 - 22 April 2020, Tulsa, Oklahoma, USA. https://doi.org/10.2118/200463-MS
16. H. Chang, Y. Zhang, A.Y. Dandekar, S. Ning, J.A. Barnes, R. Edwards, W. Schulpen, C. David P, J. Ciferno: Experimental Investigation On Separation Behavior of Heavy Oil Emulsion for

Polymer Flooding On Alaska North Slope, SPE-200369-MS, SPE Improved Oil Recovery Conference, 18 - 22 April 2020, Tulsa, Oklahoma, USA. *No DOI link, see under refereed journals*.
17. Wang, D., Li, C. and Seright, R.S., Polymer Retention Evaluation in a Heavy Oil Sand for a Polymer Flooding Application on Alaska's North Slope, SPE-200428-MS, SPE Improved Oil Recovery Conference, 18 - 22 April 2020, Tulsa, Oklahoma, USA. *No DOI link, see under refereed journals*.
18. A.Y. Dandekar, B. Bai, J.A. Barnes, D.P. Cercone, J. Ciferno, S.X. Ning, R.S. Seright, B. Sheets, D. Wang and Y. Zhang: First Ever Polymer Flood Field Pilot – A Game Changer to Enhance the Recovery of Heavy Oils on Alaska's North Slope, SPE-195257-MS, SPE Western Regional Meeting San Jose, California, USA, 23-26 April 2019. https://doi.org/10.2118/195257-MS

In addition to the above, **18** extensive RPPRs disseminate the results to communities of interest. In April 2022, Hilcorp PI Dr. Ning presented the 2020 SPE ATCE paper (First Ever Polymer Flood Field Pilot to Enhance the Recovery of Heavy Oils on Alaska North Slope – Producer Responses and Operational Lessons Learned) to the Chevron Heavy Oil Community of Practice Technical Sessions Series. Significant interest in our project was evident from the questions that were received. This also is apparent from the fact that Chevron has major plans for polymer EOR in the Kern County area of California.

7. Impact and Future Directions

Nearly four and a half years since the start of the project, the pilot and other supporting activities have concluded successfully (in particular proving the polymer flooding technology) that has created a renaissance for heavy oil recovery on ANS. Specifically, on MPU polymer flood has expanded to 6 drilling pads and 29 injectors (32 mbd polymer solution) targeting oil viscosity in the range of 40–1,300 cP. Other ANS operators such as ConocoPhillips Alaska is keenly watching the developments, and has been engaged in dialog with Hilcorp on the specifics of the field pilot, and we believe that the short term polymer injectivity test and planned polymer flood pilot test by Eni Petroleum in Nikaitchuq was inspired by this field pilot.

This field laboratory has been an excellent example of "effective" collaboration between the federal government, industry and academia. The project has been an excellent outreach tool since it is actually showcased (relevant parts of it) in the petroleum engineering curriculum, and is a topic of frequent technical discussions, at many places. As part of the April 2022 virtual IOR meeting, New Mexico PI Dr. Seright gave a short course on polymer flooding in which 5 out of the 13 participants were from Chevron, which again is indicative of the impact our project is making as well as Chevron's plans for polymer EOR in the Bakersfield area. Finally, following the results from our project, Dr. Seright also has made certain recommendations that pertain to produced water sampling for improving the ongoing polymer floods at other pads on the Milne Point Unit.

Finally, the (success) of this project is an excellent segue into unlocking the stranded heavy oil in the Ugnu area. On July 1, 2022 the Recipient embarked on phase 1 (laboratory scale) testing of a novel concept called as PAS (polymer alternating solvent) for improving the recovery of 2,000+ cP Ugnu

heavy oil. Successful completion of phase 1 will lead to phase 2 field trial that will be modeled after this project.

8. Acknowledgments

"This material is based upon work supported by the US Department of Energy, Office of Fossil Energy and Carbon Management, administered by the National Energy Technology Laboratory, under Award Number DE-FE0031606."

The authors also would like to thank Hilcorp Alaska, LLC for cosponsoring this project. We especially thank the engineers and operators (Jeremy Alvord, Cody Barber, Aaron Barlow, Brock Birkholz, Kyler Dunford, Kade Foust, David Haakinson, James McKenna, Joel Milette, Doyle Miller, Connor Redwine, Jerry Stinson, Gabriel Toci, Ryan Traxler, and Will West) of Hilcorp's North Slope Team for their tremendous efforts to ensure smooth operations for this field pilot and all our graduate students (Hongli Chang, Anshul Dhaliwal, Cody Keith, Jianqiao Leng, Chunxiao Li, Shane Namie, Xindan Wang, and Yang Zhao) and technicians for their diligent work in running lab experiments and computer models.

9. References

Amott, E. 1959. Observations Relating to the Wettability of Porous Rock. Pet. Trans. AIME 219: 156–162.

Bergaya, F., Theng, B., & Lagaly, G. (2006). Handbook of Clay Science (Volume 1) (Developments in Clay Science, Volume 1) (1st ed., Vols. 28–55). Elsevier Science.

Buckley, J. S., & Liu, Y. (1998). Some mechanisms of crude oil/brine/solid interactions. Journal of Petroleum Science and Engineering, 20(3–4), 155–160. https://doi.org/10.1016/S0920-4105(98)00015-1

Chang, H. (2022). Study on Emulsification/Demulsification Behavior and Mechanism of Produced Liquid from Polymer Flooding on Alaska North Slope [University of Alaska Fairbanks PP - United States -- Alaska]. In ProQuest Dissertations and Theses. http://uaf.idm.oclc.org/login?url=https://www.proquest.com/dissertations-theses/study-on-emulsification-demulsification-behavior/docview/2652881087/se-2?accountid=14470

Chen, Z., Du, C., Kurnia, I., Lou, J., Zhang, G., Yu, J., & Lee, R. L. 2016. A Study of Factors Influencing Polymer Hydrodynamic Retention in Porous Media. Paper SPE 179607. Presented at the SPE Improved Oil Recovery Conference. Tulsa, Oklahoma. 11-13 April. http://dx.doi.org/10.2118/179607-MS.

Dabbous, M.K. 1977. Displacement of Polymers in Waterflooded Porous Media and Its Effects on a Subsequent Micellar Flood. SPE Journal 17(5) 358-368. SPE 6203-PA.

http://dx.doi.org/10.2118/6203-PA.

Dake, L.P. 1977. Fundamentals of Reservoir Engineering. Amsterdam: Elsevier Scientific Publishing Company.

Dawson, R., and Lantz, R.B. 1972. Inaccessible Pore Volume in Polymer Flooding. SPE Journal 12 (5): 448–452. SPE 3522-PA. doi.org/10.2118/3522-PA.

Dominguez, J.G. and Willhite, G.P. 1977. Retention and Flow Characteristics of Polymer Solutions in Porous Media. SPE Journal 17(2) 111-121. SPE 5835-PA. http://dx.doi.org/10.2118/5835-PA.

A. Dandekar, J. Barnes, D. Cercone, J. Ciferno, R. Edwards, S. Ning, W. Schulpen, R. Seright, B. Sheets, D. Wang, Y. Zhang: Heavy Oil Polymer EOR in the Challenging Alaskan Arctic – It Works! Unconventional Resources Technology Conference, 26-28 July 2021, Houston, TX, USA. https://doi.org/10.15530/urtec-2021-5077

Dhaliwal, A. (2021). Experimental investigation of polymer induced fouling of heater tubes in the first-ever polymer flood pilot on Alaska north slope (Order No. 28545177). Available from Dissertations & Theses @ University of Alaska Fairbanks. (2555678694). Retrieved from http://uaf.idm.oclc.org/login?url=https://www.proquest.com/dissertations-theses/experimental-investigation-polymer-induced/docview/2555678694/se-2

A. Dhaliwal, Y. Zhang, A.Y. Dandekar, S. Ning, J.A. Barnes, W. Schulpen: Experimental Investigation of Polymer-induced Fouling of Heater Tubes in the First-ever Polymer Flood on Alaska North Slope – Part II. SPE Production & Operations, March 14, 2022. https://doi.org/10.2118/209800-PA

A. Dhaliwal, Y. Zhang, A.Y. Dandekar, S. Ning, J.A. Barnes, R. Edwards, W. Schulpen, Cercone, D. and J. Ciferno: Experimental Investigation of Polymer Induced Fouling of Heater Tubes in The First Ever Polymer Flood Pilot On Alaska North Slope. SPE Production & Operations, February 2021. https://doi.org/10.2118/200463-PA

Driver, Jonathan W., Britton, Chris, Hernandez, Richard, Glushko, Danylo, Pope, Gary A., and Mojdeh Delshad. "Conditioning Polymer Solutions for Injection into Tight Reservoir Rocks." Paper presented at the SPE Improved Oil Recovery Conference, Tulsa, Oklahoma, USA, April 2018. doi: https://doi.org/10.2118/190217-MS

Ferreira, V.H.S., and Moreno, R.B.Z.L. 2020. Polyacrylamide Adsorption and Readsorption in Sandstone Porous Media. *SPE Journal* **25**(1): 497-514. doi.org/10.2118/199352-PA.

Green, D.W., and Willhite, G.P. 2018. Enhanced Oil Recovery. Textbook Series, SPE, Richardson, Texas 6: 2nd edition.

Guetni, I., Marliere, C., Rousseau, D., Bihannic, I., Pelletier, M., and Villieras, F. 2019. Transport of HPAM Solutions in low Permeability Porous Media: Impacts of Salinity and Clay Content. Paper SPE 195434 presented at the SPE Europec featured at 81st EAGE Conference and Exhibition held in London, England, UK, 3-6 June. doi.org/10.2118/195434-MS.

Hall, H.N., "How to Analyze Waterflood Injection Well Performance," *World Oil*, 1963 (October): p. 128-130

Hunter, T. N., Pugh, R. J., Franks, G. V., & Jameson, G. J. (2008). The role of particles in stabilizing foams and emulsions. Advances in Colloid and Interface Science, 137(2), 57–81. https://doi.org/10.1016/J.CIS.2007.07.007

Jeon, T. Y., & Hong, J. S. (2014). Stabilization of O/W emulsion with hydrophilic/hydrophobic clay particles. Colloid and Polymer Science, 292(11), 2939–2947. https://doi.org/10.1007/s00396-014-3353-2

Jones, C. A. (2010). Engineering properties of resedimented Ugnu clay from the Alaskan North Slope (Doctoral dissertation, Massachusetts Institute of Technology).

Jouenne, S. and Levache, B. 2020. Universal Viscosifying Behavior of Acrylamide-Based Polymers Used in Enhanced Oil Recovery. Journal of Rheology 64(5) 1295-1313. doi.org/10.1122/8.0000063.

Keith, C. D. (2022). Technical and economic evaluation of the first ever polymer flood field pilot to enhance the recovery of heavy oils on Alaska's north slope via machine assisted history matching (Order No. 29065593). Available from Dissertations & Theses @ University of Alaska Fairbanks; ProQuest Dissertations & Theses Global. (2652887252). Retrieved from http://uaf.idm.oclc.org/login?url=https://www.proquest.com/dissertations-theses/technical-economic-evaluation-first-ever-polymer/docview/2652887252/se-2

Keller, W.D., Reynolds, R.C., Inoue, A. 1986. Morphology of Clay Minerals in the Smectite-to-Illite Conversion Series by Scanning Electron Microscope. Clay and Clay Minerals 34(2): 187-197.

Knight, B.L., Jones, S.C., and Parsons, R.W. 1974. Discussion. SPE Journal 14(6) 643-644.

Levitt, D.B. and Pope, G.A. (2008) Selection and Screening of Polymers for Enhanced-Oil Recovery. SPE Symposium on Improved Oil Recovery, Tulsa, 20-23 April 2008, https://doi.org/10.2118/113845-MS.

Long, J., Xu, Z., & Masliyah, J. H. (2006). Role of illite–illite interactions in oil sands processing. Colloids and Surfaces A: Physicochemical and Engineering Aspects, 281(1–3), 202–214. https://doi.org/10.1016/J.COLSURFA.2006.02.059

Lotsch, T., Muller, T., Pusch, G. 1985. The Effect of Inaccessible Pore Volume on Polymer Core

Experiments. Paper SPE 13590 presented at the International Symposium on Oilfield and Geothermal Chemistry. Phoenix, AZ. 9-11 April.

Ma, S., N. R.Morrow, and X.Zhang (1997), Generalized scaling of spontaneous imbibition data for strongly water-wet systems, J. Petrol. Sci. Eng., 18(3–4), 165– 178.

Manichand, R.N., and Seright, R.S. 2014. Field vs Laboratory Polymer Retention Values for a Polymer Flood in the Tambaredjo Field. SPE Res Eval & Eng. 17(3): 314-325. doi.org/10.2118/169027-PA.

Maria V.Mironova and Sergey O.Ilyin, https://doi.org/10.1016/j.fuel.2018.05.164

Masui, A., Haneda, H., Ogata, Y., Aoki, K., 2005. The effect of saturation degree of methane hydrate on the shear strength of synthetic methane hydrate sediments. In: Proceedings of the 5th International Conference on Gas Hydrates (ICGH 2005), Trondheim, Norway, June 12–16.

Mattax and Kyte 1962. Imbibition Oil Recovery from Fractured, Water-Drive Reservoir, DOI: 10.2118/187-PA, Society of Petroleum Engineers

McGuire, P.L., Redman, R.S, Jhaveri, B.S., Yancey, K.E., and Ning, S.X. 2005. Viscosity Reduction WAG: An Effective EOR Process for North Slope Viscous Oils. SPE paper 93914, presented at the SPE Western Regional Meeting held in Irvine, CA, U.S.A., 30 March – 1 April 2005.

Moradi, M., Alvarado, V., and Huzurbazar, S. 2010. Effect of Salinity on Water-in-Crude Oil Emulsion: Evaluation through Drop-Size Distribution Proxy. *Energy Fuels* **25** (1): 260–268. https://doi.org/10.1021/ef101236h

Nakatani, A. I., Mohler, C. E., & Hughes, S. (2021). Chain conformation of polymers adsorbed to clay particles: effects of charge and concentration. Soft Matter, 17(28), 6848–6862. https://doi.org/10.1039/D1SM00674F

Pancharoen, M., Thiele, M.R., and Kovscek, A.R. 2010. Inaccessible Pore Volume of Associative Polymer Floods. Paper SPE 129910 presented at the SPE Improved Oil Recovery Symposium. Tulsa, OK. 24-28 April. http://dx.doi.org/10.2118/129910-MS.

Paskvan, F., Turak, J., Jerauld, G., Gould, T., Skinner, R. and Garg, A. Alaskan viscous oil: EOR opportunity, or waterflood sand control first? SPE 180463, 2016

Quezada, G. R., Jeldres, M., Toro, N., Robles, P., Toledo, P. G., & Jeldres, R. I. (2021). Understanding the flocculation mechanism of quartz and kaolinite with polyacrylamide in seawater: A molecular dynamics approach. Colloids and Surfaces A: Physicochemical and Engineering Aspects, 608, 125576. https://doi.org/10.1016/J.COLSURFA.2020.125576

Rutqvist, Y.S. Wu, C.F. Tsang, et al. A modeling approach for analysis of coupled multiphase fluid

flow, heat transfer, and deformation in fractured porous rock Int J Rock Mech Min Sci, 39 (2002), pp. 429-442

Ryles, R. G. 1988. Chemical Stability Limits of Water-Soluble Polymers Used in Oil Recovery Processes. *SPE Res Eng* **3** (1): 23–34. SPE-13585-PA. https://doi.org/10.2118/13585-PA

Seright, R. Use of polymers to recover viscous oil from unconventional reservoirs. DOE report, Award No: DE-NT0006555, 2011.

Seright, R. Potential for polymer flooding reservoirs with viscous oils. SPE Reservoir Evaluation & Engineering, Vol. 13, No. 4, 2010.

Seright, R.S. 2017. How Much Polymer Should Be Injected during a Polymer Flood? Review of Previous and Current Practices. SPE Journal 22(1): 1-18. doi.org/10.2118/179543-PA.

Seright, R.S. Wang, D. 2022. Polymer Retention "Tailing" Phenomenon Associated with the Milne Point Polymer Flood. SPE Journal 27. doi:10.2118/209354-PA.

Shah, B.N., Willhite, G.P., and Green, D.W. 1978. The Effect of Inaccessible Pore Volume on the Flow of Polymer and Solvent through Porous Media. Paper SPE 7586 presented at the SPE Annual Technical Conference and Exhibition. Houston, TX. 1-3 October. http://dx.doi.org/10.2118/7586-MS.

Sugar, A., Serag, M., Torrealba, V.A., Buttner, U., Habuchi, S., Hoteit, H. 2021. Visualization of Polymer Retention Mechanisms in Porous Media Using Microfluidics. Paper SPE 200557 presented at the SPE Europec 82nd EAGE Conference and Exhibition. Amsterdam, The Netherlands. 14-17 June 2021. doi.org//0.2118/200557-MS.

Targac, G.W, Redman, R.S., Davis, E.R, Rennie, S.B., McKeever, S.O. and Chambers, B.C. Unlocking value in West Sak heavy oil. SPE 97856, 2005

Umar, A. A., Saaid, I. B. M., Sulaimon, A. A., & Pilus, R. B. M. (2018). A review of petroleum emulsions and recent progress on water-in-crude oil emulsions stabilized by natural surfactants and solids. Journal of Petroleum Science and Engineering, 165, 673–690. https://doi.org/10.1016/J.PETROL.2018.03.014

Vela, S., Peaceman, D.W., and Sandvik, E.I. 1976. Evaluation of Polymer Flooding in a Layered Reservoir with Crossflow, Retention, and Degradation. SPE Journal 16 (2): 82–96. SPE-5102-PA. http://dx.doi.org/10.2118/5102-PA.

Wang, D., Li, C., and Seright, R.S. 2020. Laboratory Evaluation of Polymer Retention in a Heavy Oil Sand for a Polymer Flooding Application on Alaska's North Slope. SPE Journal 25(4) 1842-1856. doi.org/10.2118/200428-PA.

Wever, D.A Z., Bartlema, H., ten Berge, A.B.G.M., Al-Mjeni, R., and Glasbergen, G. 2018. The Effect of the Presence of Oil on Polymer Retention in Porous Media from Clastic Reservoirs in the Sultanate of Oman. Paper SPE 190430 presented at the SPE EOR Conference at Oil and Gas West Asia. Muscat, Oman. 26-28 March. doi.org/10.2118/190430-MS.

Zhang, H., Cao, J., Duan, H., Luo, H., & Liu, X. (2022). Molecular dynamics insight into the adsorption and distribution of bitumen subfractions on Na-montmorillonite surface. Fuel, 310, 122380. https://doi.org/10.1016/J.FUEL.2021.122380.

Zhang, G., and Seright, R.S. 2014. Effect of Concentration on HPAM Retention in Porous Media. SPE Journal 19(3): 373-380. Paper 166256. doi.org/10.2118/166256-PA.